Ollscoil na hÉireann

NATIONAL UNIVERSITY OF IRELAND

Nanoscale Electronic Properties of Conjugated Polymers and Nanocrystals

A Thesis Presented to

The National University of Ireland

for the degree of

Doctor of Philosophy

by

Garret O'Brien

Supervised by Dr. Gareth Redmond and Dr. Aidan Quinn

Tyndall National Institute

University College Cork

May 2006

Contents

7. Appendices

Abstract

The objective of this thesis is the exploration and characterisation of the nanoscale electronic properties of conjugated polymers and nanocrystals. In Chapter 2, the first application of conducting-probe atomic force microscopy (CP-AFM)-based displacement-voltage (*z*-*V*) spectroscopy to local measurement of electronic properties of conjugated polymer thin films is reported. Charge injection thresholds along with corresponding single particle gap and exciton binding energies are determined for a poly[2-methoxy-5-(2-ethylhexyloxy)-1,4-phenylenevinylene] thin film. By performing measurements across a grid of locations on the film, a series of exciton binding energy distributions are identified. The variation in measured exciton binding energies is in contrast to the smoothness of the film suggesting that the variation may be attributable to differences in the nano-environment of the polymer molecules within the film at each measurement location. In Chapter 3, the CP-AFM-based *z*-*V* spectroscopy method is extended for the first time to local, room temperature measurements of the Coulomb blockade voltage thresholds arising from sequential single electron charging of 28 kDa Au nanocrystal arrays. The fluid-like properties of the nanocrystal arrays enable reproducible formation of nanoscale probe-array-substrate junctions, allowing the influence of background charge on the electronic properties of the array to be identified. CP-AFM also allows complementary topography and phase data to be acquired before and after spectroscopy measurements, enabling comparison of local array morphology with local measurements of the Coulomb blockade thresholds.

In Chapter 4, melt-assisted template wetting is applied for the first time to massively parallel fabrication of poly-(3-hexylthiophene) nanowires. The structural characteristics of the wires are first presented. Two-terminal electrical measurements of individual nanowires, utilising a CP-AFM tip as the source electrode, are then used to obtain the intrinsic nanowire resistivity and the total nanowire-electrode contact resistance subsequently allowing single nanowire hole mobility and mean nanowire-electrode barrier height values to be estimated. In Chapter 5, solution-assisted template wetting is used for fabrication of fluorene-dithiophene co-polymer nanowires. The structural characteristics of these wires are also presented. Two-terminal electrical measurements of individual nanowires indicate barrier formation at the nanowire-electrode interfaces and measured resistivity values suggest doping of the nanowires, possibly due to air exposure. The first report of single conjugated polymer nanowires as ultra-miniature photodetectors is presented, with single wire devices yielding external quantum efficiencies ~ 0.1 % and responsivities ~ 0.4 mA/W under monochromatic illumination.

Acknowledgements

I want to thank Dr. Gareth Redmond for giving me the opportunity to complete my PhD here in the Tyndall Institute and the wonderful direction and advice he has given me over the course of the work. I would also like to express my gratitude for the superb guidance and mentoring that I received from Dr. Aidan Quinn since I started this PhD. Their support was invaluable. I want to thank all the other members of the nanotechnology group as well, for their technical assistance and friendship. In particular, Dr. Alan O'Riordan for his help with the glovebox, Dr. Hugh Doyle for his early assistance with polymer materials and Mr Liam Floyd for his invaluable assistance with all the measurement systems. Dr. Daniela Iacopino provided great assistance in the fabrication and imaging of the nanowires. Dr. Matteo Biancardo provided excellent support with the nanocrystal work and Dr. Gianluca De Marzi's support with the polymer measurements was much appreciated. The technical assistance of many of the staff in the Institute is greatly appreciated, especially Mr Dan O'Connell and Mr John Kearney for device fabrication and Mr John Rea for helping solve so many problems. Ms Niamh O'Sullivan also helped me navigate through much of the necessary bureaucracy.

I would particularly like to thank all the students in the nanotechnology group, especially those that I started my studies with: Shane Moynihan, Paul Beecher and Sara Harvey. The students who were already in the group prior to our arrival, Mary Manning and Deirdre Murphy, were also of great help and their friendship is valued. I would particularly like to thank Deirdre O'Carroll for her assistance with the nanowire fabrication and measurement; Pierre Lovera for his support with PL measurements, ably guided by Shane Moynihan, and both Claire Barrett and Nicolas Pauget for assisting with the AFM work. Eamon O'Connor's guidance with the glovebox was excellent and his musical taste even better.

I would like to mention some of the students that I started my time here with, Ed O'Carroll and Mark O'Donovan whom I have studied with for over ten years and who are least partially responsible for the situation I find myself in now. More recently, tea with Declan Casey, Ken Reynolds, Andy Connell, Maeve Curtin and Bernadette Ahern has been enlightening (mainly about cars and bikes). Smoking breaks with Gary Grant and Micheal Morris were as enlightening.

The many members of the UCC subaqua club have been great friends over the past number of years especially those who passed through this Institute along the way. Colin Gallagher, Jan Kruger, Aaron Norman, Daniel O'Keeffe and Alan O'Neill's advice, both diving and work related, and camaraderie are greatly appreciated. I also want to thank Daphne, Emilia, Jonathan, Ken, Micheal, Mags and Marie Therese.

I thank all my friends especially Arthur, Eric, John, Paul, Roger and Tanja not least for reminding me that there is indeed a world outside the college gates even if I was their final link to college.

Finally, I would like to thank all my family for their immense support, encouragement and tolerance while I have studied here. I could not have managed without them.

_____

Garret O'Brien

Success is going from failure to failure without loss of enthusiasm.

Winston Churchill (1874-1965)

To my Parents

Chapter 1

Introduction

1.1 Introduction

The ever-increasing complexity and functionality of today's electronics products presents enormous challenges to the semiconductor industry with respect to fabrication processes as well as to maintaining the pace of development. Moore's law, which suggests that the integration level or complexity of integrated circuits will double every 18 months while the cost remains fixed, has guided industry for the last 40 years. For specific applications, an alternate approach to the ever more costly conventional fabrication techniques is the use of novel alternative materials to realise improved functionality whilst reducing cost and concurrently improving device performance. Two broad classes of materials that are proposed to satisfy these criteria are conjugated polymers and nanocrystals.

Since the discovery of the first electrically conducting polymer in 1974 by Heeger, MacDiarmid and Shirakawa the investigation of conducting polymers has expanded considerably with an increasing range of polymers developed with various attributes. The discover of polymer light emitting diodes (PLEDs) by Friend and co-workers at the Cavendish Laboratory at Cambridge University provided fresh impetus for research into these materials, which has resulted in an explosion in research activity in organic materials due to their potential as a lower cost replacement for established technologies in a wide variety of commercial applications ranging from display technologies to telecommunications systems. Currently conjugated polymer solutions have been proposed and commercialised as cheap displays for mobile phones, cameras and monitors. A further potential application is in the development of flexible displays, which are currently unrealisable using current CMOS and LCD solutions. The potential for nanoscale polymer based devices also exists.

Scientific interest in metal nanoparticles dates back to pioneering studies by Faraday in the 1850s. Physical methods of nanoparticle fabrication such as vacuum evaporation have been in existence for decades. However, recently developed methods of chemical synthesis allow far greater precision to be exerted in the fabrication process in terms of particle size, shape and crystallinity. This has led to these newer nanostructures being referred to as nanocrystals, and indeed their crystalline structure, with clearly defined lattice planes, has been characterised. Size control is especially significant, as the electronic properties of nanocrystals are critically dependent on their size. Nanocrystals have thus been dubbed "artificial atoms". Nanocrystals are predicted to play a prominent role in the development of near-term microelectronics applications, for example in the fabrication of flash memory devices. Nanocrystal composite materials are also expected to yield stronger, lighter, wear resistant components for aerospace and automotive applications.

1.2 Conjugated Polymers

1.2.1 Conjugated Polymers

Polymers are macromolecules containing hundreds or thousands of atoms and have been known and utilised for decades for a wide range of applications. While the initial applications of polymers for electronics exploited their insulating properties, recently it has been found that polymers have extensive conductive properties, which span the range from fully insulating to highly conducting, as well as photonic properties. Polymers are organic materials that consist of long chains of repeating base molecules (monomers). In a conjugated polymer structure, repeating monomers form the backbone of the chain and single and double atomic bonds occur alternately throughout the chain. The simplest polymer, polyethylene is composed of multiple ethene monomers; see Figure 1.1(a). Natural polymers include such materials as tar, shellac, tortoise shell and horns, as well as tree saps that produce amber and latex. These polymers can be processed with heat and pressure into useful products. Natural polymers began to be chemically modified during the 1800's to produce many materials. The most prominent of these were vulcanised rubber, gun cotton and celluloid. The first truly synthetic polymer produced was Bakelite in 1909 and was soon followed by the first synthetic fibre, rayon, which was developed in 1911.

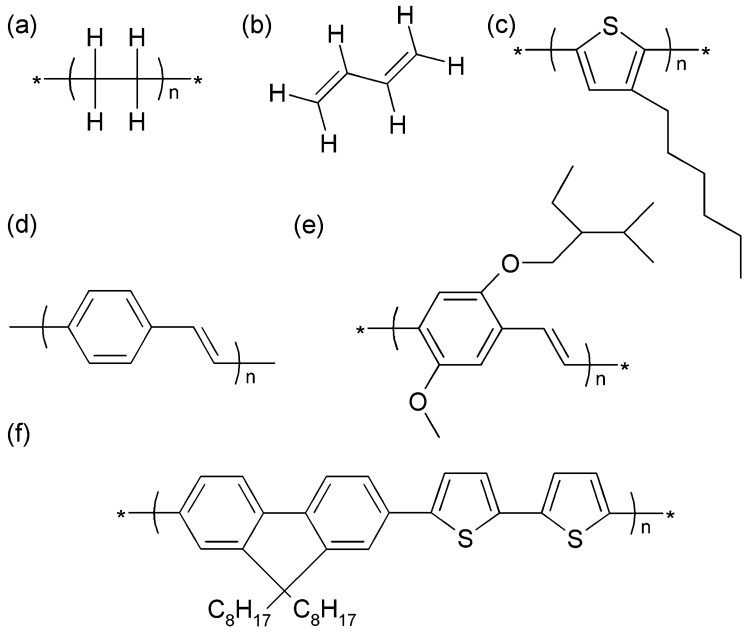

Figure 1.1. Molecular structures of some typical polymers: (a) polyethylene, (b) butadiene, (c) P3HT, (d) PPV, (e) MEH-PPV and (f) F8T2. All except polyethylene are conjugated polymers, featuring alternating single and double bonds along the backbone of the polymer.

The first report of a highly conducting polymer, doped polyacetylene, in 1977,[1] sparked an enormous interest in this new class of materials. A key feature of these materials, which was quickly elucidated, is a backbone consisting of alternating single and double bonds resulting in a π-conjugated network. This results in a relatively small energy gap, enabling the appearance of both semiconducting and metallic properties. The first iterations of conducting polymers were unstable in air and difficult to process. While a large amount of progress has been made with regard to these issues, such as the increased stability of materials and the ability to solvent process them, challenges still remain.

Light emission from conjugated polymer based devices was first reported in the 1980s stimulating interest in this area of research.[2] The repeat unit structure of the first conjugated polymer used for polymer electroluminescent devices, poly(p-phenylene-vinylene) (PPV), is shown in Figure 1.1(d). Commercially viable organic light emitting diode (OLED) based optical solutions have reached the market in, for example, mobile phone displays, camera displays and high brightness white OLEDs for lighting solutions.

A wide range of other devices have been proposed to exploit some of the novel properties of conjugated polymer such as flexible displays, sensors and solar energy panels.[3] Thin film transistors (TFTs) fabricated from conjugated polymers have been developed that have a huge range of applications, e.g., all-polymer optoelectronic integrated circuits such as active-matrix polymer LED displays.[4,5] The use of one-dimensional (1-D) nanostructures fabricated from conducting polymers and small organic molecules has also attracted increasing research interest due to their unique physical, chemical and electronic properties, together with the wide range of potential applications in nanoscience.[6,7] Organic semiconductor nanowires could be exploited as building blocks for nanophotonics, *e.g.*, as emissive devices, photodetectors and (active) waveguides.

1.2.2 Electronic Structure of Conjugated Polymers

Carbon (C) is a Group IV element that has four free electrons in its outer shell, each with an associated wavefunction; see Figure 1.2(a). The electronic configuration of the carbon atom allows it to form a number of hybridised atomic orbitals. Carbon atoms in the elemental substances (e.g., diamond, graphite, and Buckminsterfullerenes) bond to each other covalently, by the sharing of electron pairs. The covalent bonds have directional properties. This in turn gives carbon the ability to adapt into various molecular and crystalline structures. The nature of these bonds underlies the varied chemical properties and physical properties of the carbon allotropes.

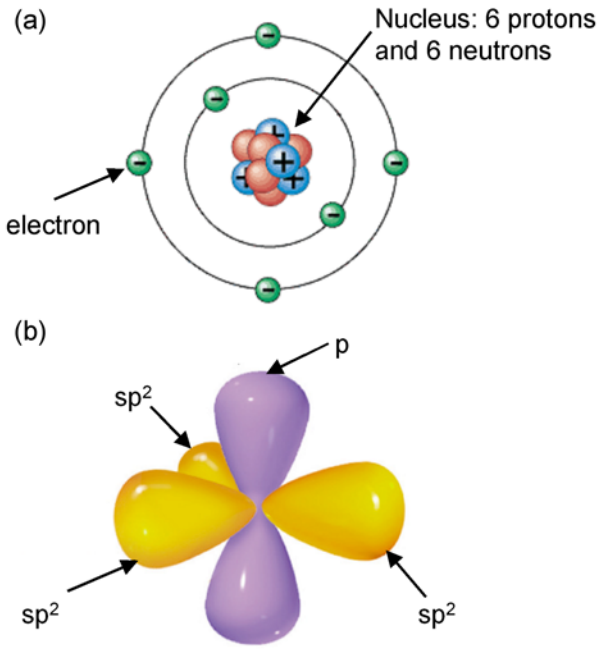

Figure 1.2. (a) Simplified atomic structure of a carbon atom. (b) Orbital configuration of a carbon atom along the backbone of a conjugated polymer system with three sp^2 hybrid orbitals in the same plane forming σ bonds and one remaining p_z orbital overlapping to form π bonds. Images: Prentice-Hall Inc., USA.[8]

Carbon, like many of the second-row elements of the Periodic Table, has atomic orbitals that can hybridise. This is because the s-orbital and p-orbitals of carbon's second electronic shell have very similar energies. As a result, carbon can adapt to form chemical bonds with different geometries. While standard insulating organic polymers have saturated (sp^3 hybridised) carbons along the backbone of the chain, organic conjugated polymers have backbones consisting of sp^2 hybridised carbons. Three orbitals (sp^2 orbitals) exist in one plane with the fourth orbital (p_z orbital) orthogonal to this plane; see Figure 1.2(b). When carbon atoms are brought into proximity with each other the in-plane sp^2 orbitals overlap. This overlap creates a very strong bond called a σ bond between the two carbon atoms. These bonds are strongly localised between the carbon atoms and can form the backbone of, e.g., a polymer chain. The orthogonal p_z orbitals are symmetric between adjacent atoms and the coupling of these orbitals creates delocalised bonds. The p_z orbitals are wave functions with an associated phase and the coupling of these wave functions may result in constructive or destructive interference. In-phase coupling (constructive interference) creates π orbitals or bonding states, which stabilise the polymer chain. These make up the highest occupied molecular orbital (HOMO), which is analogous to a valence state in a semiconductor. Out-of-phase coupling (destructive interference) creates $\pi^{*\square}$ orbitals or anti-bonding states, and results in the formation of less stable high energy bonds due to the reduced coupling between the p_z orbitals. These make up

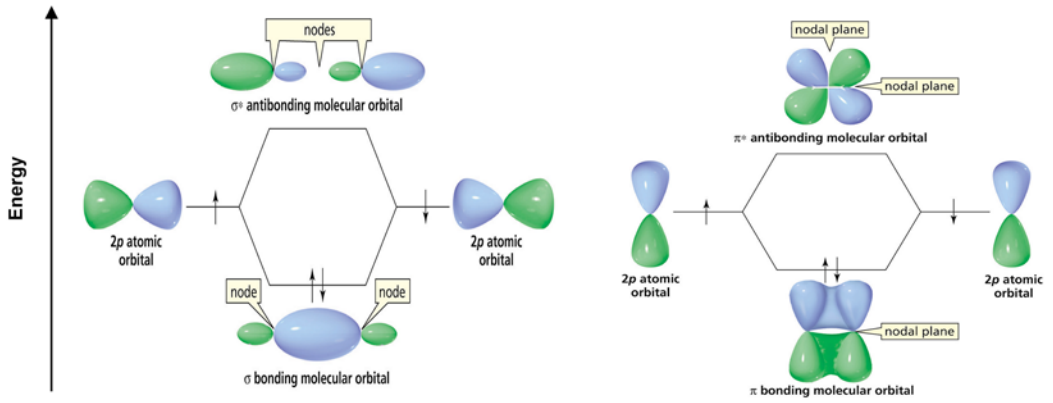

Figure 1.3. Left: End to end overlap of in-phase sp^2 atomic orbitals forms carbon-carbon single σ bonds while lateral overlap (right) of in-phase p_z atomic orbitals forms carbon-carbon π bonds. Nodes represent regions where electron probability density approaches zero. The colours represent the phase of the lobe in the orbitals. Images: Prentice-Hall Inc., USA.[8]

the lowest unoccupied molecular orbital (LUMO), which is analogous to the conduction state in a semiconductor. The formation of such orbitals is graphically presented in Figure 1.3, where the end to end overlap of 2p orbitals leads to σ bonds and the side to side overlap of 2p orbitals leads to π bonds.

Just as the spatial arrangement of carbon atoms determines their electronic states and bonding, occupancy of these electronic states influences the geometric structure of the atoms of

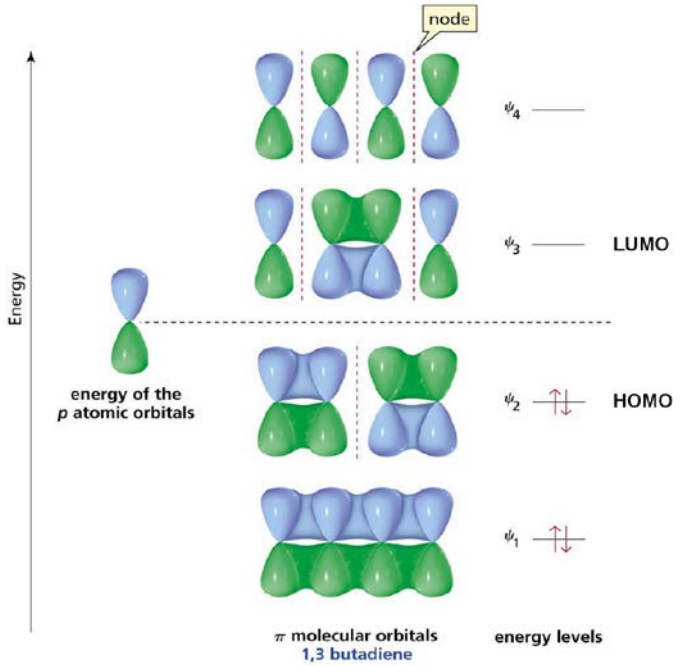

Figure 1.4. 3-D representation of the molecular orbitals (MOs) of butadiene. The energies of the MOs and the positions of the HUMO and LUMO are indicated. Images: Prentice-Hall Inc., USA.[8]

the molecule. The dimer configuration of alternating single and double carbon-carbon bonds in a polymer chain arises from the uneven distribution of π / π* electrons along the chain. This is mirrored in the different bonding-antibonding structures of the HOMO and LUMO states, which highlights the interdependence of electronic and geometric configurations in a conjugated polymer.[9,10] Figure 1.4 illustrates the four π molecular orbitals found in butadiene (C_4H_6), which is the simplest conjugated polymer; see Figure 1.1(b).

1.2.3 Optical Properties of Conjugated Polymers

Spectroscopy is the study of the interactions between matter and electromagnetic radiation. In particular, spectroscopy in the ultraviolet and visible spectrum can provide a wealth of information regarding the properties of conjugated polymers. Only conjugated polymers with π electrons exhibit light absorption in this spectral range. The moieties of a molecule that absorb ultraviolet and visible light are termed chromophores and each chromophore has a characteristic absorbance wavelength. As it is possible to chemically tailor the structures of conjugated polymers, each of which having unique optical properties, it follows that absorbance versus wavelength measurements can be used to identify and characterise individual polymers.

The absorption of photons by an organic molecule can result in the excitation of electrons from an initially occupied, low energy orbital (usually the HOMO) to a higher energy, previously unoccupied orbital (usually the LUMO). The resulting electron-hole pair is called an exciton and upon excitation either singlet or triplet excitons are produced, depending on whether the paired electron and hole spins are anti-parallel or parallel, respectively.[9] A map of the potential energy versus nuclear configuration for a particular electronic state is called a potential energy surface.[9] Figure 1.5 shows a potential energy surface diagram for a molecule where S_0, S_1, and T_1, denote the ground singlet state, excited singlet state and excited triplet state, respectively. The minimum of the curve in the ground state is normally at a lower internuclear distance than that of the excited state. Within the electronic excited and ground states further discrete energy levels exist called vibronic states arising from vibrations of the molecule.[9] Due to fast relaxation between vibronic levels, electrons relax to the lowest vibronic level of the electronic state that they occupy. Absorption results in transitions from the 0 vibronic level of the S_0 ground state to the vibronic levels of S_1. These transitions are vertical due to the fact that an electronic transition occurs much faster than a change in the nuclear configuration of the atoms of the molecule, in agreement with the Franck-Condon principle, which states that the structure of a molecule does not change during certain fast reaction processes and also that for such processes orbital symmetry must be conserved.

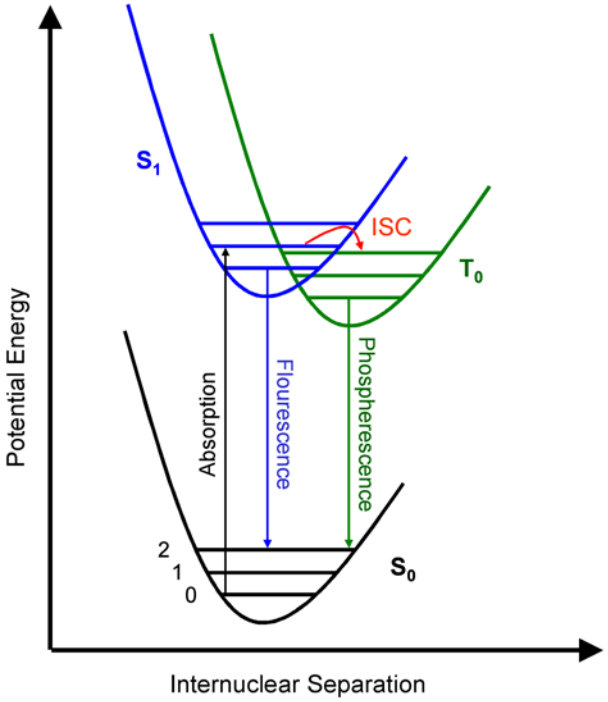

Figure 1.5. Potential energy surface diagram of molecular absorption and photoluminescence processes.

Photoluminescence is emission of light from a material that has absorbed light energy and may be divided into two categories, namely, fluorescence and phosphorescence; see Figure 1.5. In this process, the material's electrons are promoted from the HOMO level to excited states in the LUMO by absorption of photons. The emitted light is the result of those electrons, which relax back to the ground state by emitting photons. The period between absorption and emission is typically extremely short, on the order of 10 nanoseconds. Under certain circumstances, however, this period can be extended into minutes or hours. Both the wavelength of light required to cause photoluminescence and the wavelength of light emitted depend on the energy difference between the ground and excited electron states. That is, the band gap energy is a key parameter in photoluminescence. The relationship between energy and wavelength is given by $E = hc/\lambda$, where h is Planck's constant, c is the speed of light, and λ is the wavelength of light. Fluorescence results from a transition from the 0 vibronic level of the S_1 excited state to the vibronic levels of the S_0 electronic ground state. The slight energy difference of the transitions between vibronic levels of excited and ground states gives rise to a progression of vibronic peaks in the optical spectra (vibronic progression).

If the S_1 and T_1 potential energy curves overlap a conversion from a singlet to a triplet state may occur via intersystem crossing (ISC). Phosphorescence arises from a transition from T_1 to S_0. Since phosphorescence requires a change in the electron spin it is 'spin forbidden' according to the principle of spin conservation, and has a much longer lifetime (~ ms) than

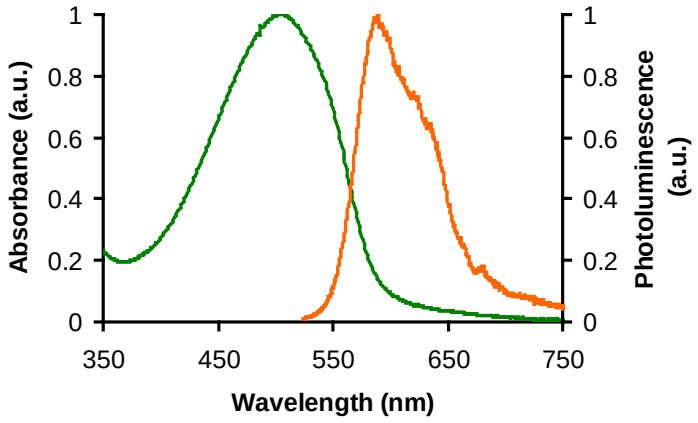

Figure 1.6. Typical absorption (green line) and photoluminescence (orange line) spectra of a MEH-PPV thin film on glass.

fluorescence (~ ns) which is 'spin allowed'.[9] Therefore, in general only fluorescence is observed as light emission in conjugated polymers.

Figure 1.6 shows typical absorption and photoluminescence spectra recorded for a MEH-PPV film on glass. The absorption maximum occurs at ~ 505 nm and the emission is orange-red with a maximum at ~ 590 nm. The broad emission spectrum is characteristic of conjugated polymers and arises from effects associated with inhomogeneous broadening due to a distribution of conjugation lengths and the presence of a vibronic progression.[11] Distinct vibronic peaks are not clearly observed in the spectra.

Not all electrons relax luminescently and contribute to photoluminescence. This fact is important when considering the efficiency of OLEDs. An excited electron will have one of several possible fates that include relaxation to a ground state by releasing only heat. However, the dominant path in polymer photoluminescence involves an electron thermally dissipating some energy to settle into the lowest energy excited state before emitting a photon to relax to the ground state. Other excited electrons may jump to neighbouring molecules or segments of the same molecule and thereby transfer charge. For instance, in what is called a well-barrier structure, there may be a large difference in the HOMO levels between adjacent molecules such that electrons move to the lower energy molecule. Electron spin restrictions allow only 25% of created excited states to be of the singlet type while all others are nonemissive triplet states. Therefore, at a maximum, only 1 in 4 excited electrons will contribute photoluminescence. The photoluminescence quantum efficiency is defined as the percentage of singlet states that do emit light and is proportional to the intensity of fluorescence. This excludes any light generated by the slower triplet processes.

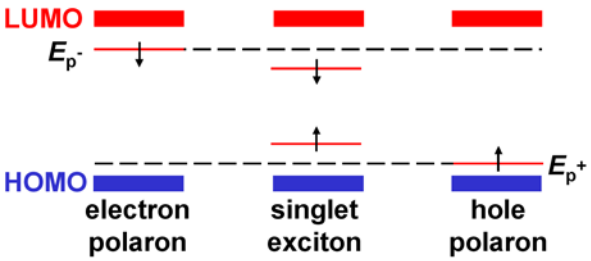

Figure 1.7. Schematic of polaron energy levels. Combination of polarons with opposite charge and spin forms a singlet exciton.

Conjugated polymers can be described as quasi-one-dimensional semiconductors. The HOMO-LUMO gap of the undoped material is such that the absorption edge is in the visible or near infrared. Typically, they are disordered with long chains that can be interrupted by defects caused by bending, dopant atoms, crosslinking, etc. Typical conjugation lengths for PPV are 6 to 8 monomers. Illumination of a conjugated polymer sample by light with energy beyond its absorption edge can result in excitation of a variety of entities including polarons, bipolarons, excimers, excitons and aggregates. Upon absorption of a photon past the absorption edge, an electron is raised to the LUMO and a hole is left behind in the HOMO. There can be several possible outcomes to such an event.

If the electron and hole are sufficiently separated and do not interact enough to form an exciton (see below), each is termed a polaron.[12] Possible causes of such separation include the movement of the hole and electron on creation to different chains; or capture by defects. Hole and electron polarons are typically denoted P^+ and P^-, respectively. Polarons provide two energy levels located symmetrically about the centre of the gap with the position of the polaron level relative to the HOMO and LUMO dependent on the chain length; see Figure 1.7.

Bipolarons consist of two like charges with opposite spin bound together within the same conjugation length. The bipolaron occupies two levels in the gap. The stability of the bipolaron is doubtful in the absence of oppositely charged ions.[13]

An excimer is a complex between an excited state of a molecule and a molecule of the same species that is not excited, i.e., in its ground state.[14] Although only one of the molecules is initially excited, the wave function of the complex must be symmetric or anti-symmetric as the two molecules are identical. The stability of the excimer is due to the overlap of π orbitals of the two molecules. The molecules must be sufficiently close to allow sufficient interaction but not so close that the ground states form a new stable molecule. Separation values range from 0.3 nm to 0.4 nm and are typical of at least one interchain distance in conjugated polymers.

This makes conjugated polymers a good candidate for excimers. The chains should also be parallel for at least a few monomers for good interaction of the π orbitals. An excimer has an emission at a lower frequency than that of a molecule in isolation, due to the lower energy in the excimer state and because in the final state, where both molecules are in their ground state, they repel each other.

A likely fate for an electron-hole pair generated by light is that the electron and hole form an exciton, where both remain on the same chain bound together by electrostatic attraction and to a lesser extent by the chain deformation or relaxation they cause. Such excitons are singlet excitons as the hole and electron have opposite spin.

The role of interchain interactions also has a large effect on the properties of conjugated polymer materials. Aggregate states are a manifestation of interchain interactions, which lead to ground state interactions. Aggregates refer to several polymer chains together with a common ground and excited state due to the delocalization of the ground- and excited state wavefunctions over several polymer chains. It is therefore possible to access aggregates directly via spectroscopy. Aggregation leads to a redshift in both emission and absorption spectra. Near field scanning optical spectroscopy (NSOM) has also been utilised to investigate the presence of aggregates in poly(*p*-pyridyl vinylene) (PPyV) polymer films, for example.[15] The formation of aggregates has been shown to be solvent dependent, with films prepared from solvents in which the polymer dissolves well possessing more aggregation sites.[16] The presence of such aggregates can also be observed in the topography of the polymer films.

1.2.4 Electrical Properties of Conjugated Polymers

As stated earlier the presence of π orbitals in conjugated polymers permits them to conduct charge. Each π orbital can hold two electrons per atom (with spin up and down, respectively), the π orbital is filled while the π^* orbital is empty. As there are no partially filled orbitals, conjugated polymers are typically semiconductors. The σ bonds however are highly localised and do not contribute to electrical conductivity. The alternating bond length of the single- and double carbon carbon bonds create an energy gap at the Fermi level. As the energy gap, E_g, depends on the structure of the monomer, it is possible to control this gap at a molecular level. Charge can be introduced into a conjugated polymer in a wide variety of means such as chemical doping, charge injection from electrodes and exciton splitting. It is possible to reversibly dope conjugated polymers, with associated control of the electrical conductivity over the full range from insulating to metallic.

A wide range of experimental work and simulation has been conducted to characterise charge injection and transport in conjugated polymer devices.[17-19] Much of this experimental work has been conducted on prototypical OLED devices, i.e., two terminal diode structures with a polymer film sandwiched between two metallic electrodes, to determine whether charge injection or charge transport dominates the device performance.[18] The contributions of hole and electron current to the total device current have been investigated using hole and electron only devices and suggest that electrons are severely trapped in typical conjugated polymers such as PPV resulting in differences of several orders of magnitudes in the respective currents.[18]

The mobility, μ, describes how strongly the motion of an electron or hole is influenced by an applied field, E. For a free particle a constant accelerating force exerted by a field leads to a linear increase of momentum with time. For a constantly accelerating particle, which experiences interactions with its surroundings, velocity (v) is usually not continuously increasing but assumes a constant average value. The average velocity gained per unit field, $v/E = (e/m)\tau$, is then the mobility where e is the electronic charge, m is the mass of the charge and τ is the relaxation time.

This simple definition of mobility needs to be modified for conjugated polymer materials. A large range of factors including temperature, electric field and material order influences the mobility of charge carriers.[25] Highly ordered conjugated polymer films exhibit far greater mobility than films with low order especially for current flow parallel to the alignment.[26] The mobility of various polymers has been modelled using a range of means including Monte Carlo simulations and has been experimentally measured using techniques such as time of flight (TOF) spectroscopy as well as from measurements of field effect transistor characteristics.[25]

The mobility of single crystal silicon used in conventional microelectronics is on the order of 10^3 cm^2 V^{-1} s^{-1}. While an extremely wide range of mobility values have been reported for conjugated polymers, the maximum value to date is on the order of 1 cm^2 V^{-1} s^{-1}.[27] High mobility is a critical factor for the proposes of creating high speed circuits but is less critical for low operating frequency devices such as OLEDs and low speed flexible circuits.

The interfacing of a conjugated polymer device to external contact electrodes is a critical factor in device operation and efficiency. For conjugated polymer devices, the contact resistance is dependent not only on the polymer characteristics but also on the contact metal, the barriers between the metals and the polymer, the device geometry. The contact resistance can be a substantial fraction of the total resistance of a device.[28] Matching the workfunctions of

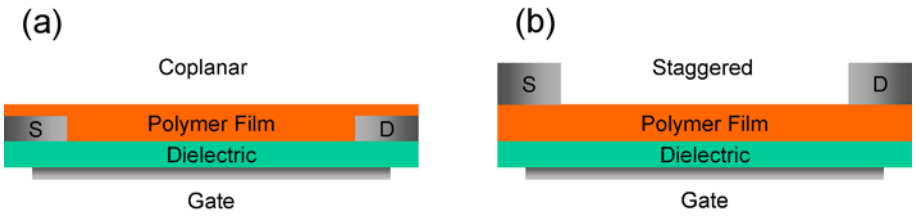

Figure 1.8. Schematic representation of two possible geometries for polymer device fabrication. The coplanar geometry is shown in (a) where the polymer film is spin coated onto the predefined source (S) and drain (D) electrode contacts. The staggered geometry is shown in (b), where the electrodes are deposited after the polymer film has been deposited.

the source and drain electrodes in a two terminal device to the HOMO and LUMO levels respectively allows maximum coupling of charge carriers from the electrodes the device. This reduces the injection barriers; typical materials include gold, ITO, aluminium and calcium.

Polymer devices such as transistors can be fabricated in either the coplanar or staggered geometry; see Figure 1.8.[29] The coplanar geometry allows predefined electrodes to be utilised and the polymer to be spin coated onto predefined electrodes. The staggered geometry is generally less susceptible to high contact resistance than the coplanar geometry because the effective area of the contact is larger.[29] However the process of depositing such top contacts, for example by sputter coating, can, in itself, influence the contact resistance.[29]

Charge transport is generally dominated by one of the injection or bulk limiting mechanisms include tunneling, phonon-assisted tunneling or hopping and space charge limited current, which is applicable for materials with low mobility. For carrier transport in low-mobility semiconductors, diffusion effects must also be considered. Tunneling behaviour has been assigned to Fowler-Nordheim injection of carriers from the electrodes at high fields ($F_t \approx 10^7$ Vm^{-1}), however at lower fields, the model deviates from the experimental characteristics and mechanisms such as thermionic emission have been utilised in the low field regime. Unambigious interpretation of the data has been difficult to obtain. More sophisticated models have been developed to achieve closer agreement with the measured data. These modifications include field dependent carrier mobilities and bipolar carrier-transport models. The large improvements in material quality and uniformity and device preparation have played an important role in aiding this deeper understanding.

Direct tunneling of a charge carrier through a rectangular barrier can be described as follows:

$$J \approx V \exp\left(-\frac{4\pi L}{h}\sqrt{2m\phi_b}\right)$$

where L is the device length, h is Planck's constant, m is the electron mass and ϕ_b is the barrier height. Fowler-Nordheim tunneling can be modelled as follows:

$$J \approx V^2 \exp\left(-\frac{4L\sqrt{2m}}{3qhV}(q\phi_b)^{1.5}\right)$$

here, q is the carrier charge. Direct tunneling and Fowler Nordheim tunneling depend on the applied bias, device length and the barrier height. To a first order, they are independent of temperature. Tunneling mechanisms can be modified to account for variable barrier geometries, multi-step tunneling and trap assisted tunneling.

Hopping conduction refers to the process in which thermally excited charge carriers hop from one isolated state to the next, whose conductance also depends strongly on temperature. A range of hopping mechanisms such as nearest neighbour hopping and variable range hopping have been proposed to characterise charge transport in conjugated polymers. These mechanisms have been analysed through experimental and Monte-Carlo simulations.[21] Hopping conduction mechanisms are characterised by the following *J*-*V* characteristic:

$$J \propto V \exp\left(-\frac{\Delta E}{kT}\right)^2$$

where ΔE is the hopping barrier.

A number of thermionic emission mechanisms have also been proposed. The thermionic emission diffusion theory of Crowell and Sze for current injection into low mobility semiconductors gives:[19]

$$J = qN_c\mu F(0)\exp\left(-\frac{q\phi_b}{kT}\right)$$

where q is the carrier charge, μ is the mobility, N_c is the carrier concentration, $F(0)$ is the electric field at the contact, ϕ_b is the barrier height, k is Boltzmann's constant and T is the Kelvin temperature. The barrier height, ϕ_b, is lowered by the image force according to

$$\phi_b = \phi_{b0} - \Delta\phi = \phi_{b0} - \sqrt{\frac{qF(0)}{4\pi\varepsilon_0\varepsilon_r}}$$

where ϕ_{b0} is the injection barrier at zero field and $\varepsilon_0\varepsilon_r$ is the permittivity of the polymer. For an ohmic contact $F(0) = 0$, and the J-V behaviour is given by:

$$J = \frac{9}{8}\varepsilon_0\varepsilon_r\mu\frac{V^2}{L^3}$$

The quadratic dependence of J on V is characteristic of the so-called space charge limited current (SCLC). For an insulator with traps, at lower biases the current in this case is given by Ohm's law. Ohmic behaviour is expected for devices with contact barriers lower than ~ 0.4 eV. If the work function can be closely aligned to the respective polymer levels then the metal-polymer contact becomes an ohmic contact and the electric field at the contact is zero.[20] Here the current density is controlled by the transport of charge carriers across the device.

$$J = qN_0\mu\frac{V}{L}$$

where N_0 is the equilibrium electron density. The transition from ohmic to SCLC occurs at a threshold voltage value of $V_0 = (8/9)\ qN_0L^2/\varepsilon_0\varepsilon_r$.

A number of factors have been shown to have significant detrimental effects on charge transport in conjugated polymers. These include energy disorder effects arising from charge localisation on polymer strands due to weak inter-chain coupling, the presence of defects, contact resistance and polymer morphology. The ability to spin cast homogenous films of conjugated polymers is one technique to reduce the effects of morphology on charge transport. The preparation of devices in controlled environments can greatly reduce the effects that oxygen and water can have on the polymer. Contact resistance effects are also expected to have a significant role as the width/length ratios scale down from planar/vertical device values (W/L ~ 10^3),[22,23] towards the dimensions of 1-D nanowire devices (W/L << 1).

1.2.5 Opto-electrical Properties of Conjugated Polymers

Electroluminescence is the emission of light due to the radiative recombination of electrons and holes in the material as a result of direct electrical excitation. Electroluminescence from organic semiconductors was first reported in 1963 from anthracene single crystals.[30] These devices required high operating voltages (~ 400 V) due to the thickness of the crystals (10 – 20 μ m). In 1977 the report of a polymer, doped polyacetylene,[1] having a high metallic-like conductivity heightened interest in semiconducting organic materials and their potential for integration into electronic components. A subsequent major breakthrough in the field occurred in 1987 when Tang *et al.* demonstrated electroluminescence from an organic thin film (~ 100 nm) of tris 8-(hydroxyquinoline) aluminium (Alq_3), a small molecule material.[31] The organic layer was deposited by a vacuum evaporation technique, and was sandwiched between two metallic electrodes. The operating voltage of this device was only ~ 10 V, indicating the potential of this organic light emitting diode (OLED) device structure for commercial lighting applications. In 1990, electroluminescence from a conjugated polymer thin film was first demonstrated by employing a similar device structure. The polymer used, poly(p-phenylene-vinylene) (PPV), was deposited from solution using a spin casting technique.[2] This led to an explosion in research interest in emissive organic materials due to their potential as a lower cost replacement for established technologies (inorganic semiconductor optoelectronics) in a wide variety of commercial applications from display technologies to telecommunications systems.

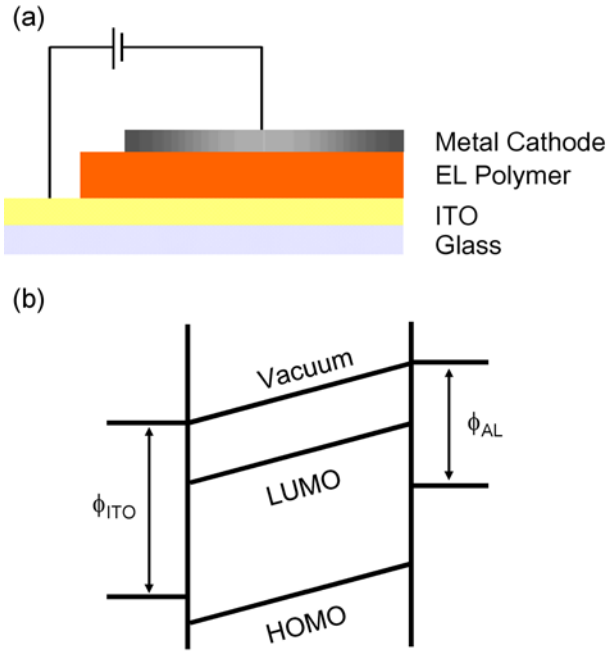

Figure 1.9. (a) Typical single layer OLED device structure (not to scale). (b) Schematic energy level diagram for an ITO/MEH-PPV/Al device.

A typical single layer polymer electroluminescent device consists of a spun cast organic emissive layer sandwiched between two electrodes; see Figure 1.9. The operation of these devices is determined by a range of factors including carrier injection, carrier transport, recombination and light emission processes. Upon the application of a sufficient forward bias, electrons and holes are injected into the polymer layer from the cathode and anode, respectively. Charge carriers must first overcome the offset between the respective workfunction and the polymer energy levels by tunneling through a triangular barrier.[18]

The application of an electric field causes the injected holes and electrons to migrate from polymer chain to polymer chain before recombining on a single conjugated segment to form excitons. Such excitons are identical to those generated by optical excitation. As stated earlier, spin statistics yield a 3:1 ratio between singlet and triple excitons. As the emission of light is solely due to the relaxation of singlet excitons, the maximum achievable efficiency for polymer electroluminescent devices is 25 %. As the hole mobility of organic polymers is orders of magnitude higher than that of electrons, holes are the majority carrier in polymer based devices. For simple single layer devices this results in the recombination of singlet excitons occurring close to the cathode, which can lead to luminescence quenching by the metal, reducing the efficiency of the devices. The choice of electrodes employed in a device is critical in order to achieve balanced carrier injection and high device efficiency. The work functions of the anode and cathode materials are tuned so that they have respectively high and low work functions to match the HOMO and LUMO of the polymer film. This permits the efficient injection of holes and electrons at the anode and cathode, respectively. Generally indium-tin oxide (ITO), an optically transparent material with a high work function, deposited on a glass substrate is used as the anode material. However as deposited ITO is non-stoichiometric, it is a poorly controlled material and properties such as its work function, mobility and roughness can vary significantly. Frequently, a hole conducting polymer, 3,4-polyethylene-dioxythiophene-polystyrenesulfonate (PEDOT), is spun cast onto ITO. This process planarises the anode and provides a consistent but lower work function, enhancing the device efficiency.

The cathode material is chosen so that its workfunction is close to the emissive polymer LUMO level to achieve efficient injection of electrons into the emissive layer. Typical cathode materials include aluminium (ϕ = 4.2 eV) and calcium (ϕ = 2.9 eV). An organic electron transport layer can also be incorporated between the cathode and the emissive polymer layer. This enhances the electron transport in the device and provides a measure of control of the region where recombination of excitons takes place, displacing it from the polymer cathode interface. This reduces luminescence quenching by the metal thus increasing device efficiency.

Photoconductivity (PC) is an optical and electrical phenomenon in which a material becomes more conductive due to the absorption of electromagnetic radiation such as visible light, ultraviolet light, or gamma radiation. To be photoconductive a semiconductor must be in thermal equilibrium. When light is absorbed by the semiconductor, the configuration of electrons and holes changes and raises the electrical conductivity of the semiconductor. To cause excitation the light that strikes the semiconductor must have enough energy to raise electrons across the forbidden bandgap or by exciting impurity states within the bandgap. A classic example of photoconduction is in the polymer polyvinylcarbazole, which is used extensively in photocopying technology. Spun cast thin films of photoconductive conjugated polymers have been used to created photodetectors and photoswitching devices.[32] Polarisation sensitive photodiodes have also been fabricated using aligned polymer layers.[33]

Photovoltaics (PV) are semiconductor devices that convert sunlight into direct current (DC) electricity. The first conventional photovoltaic cells were produced in the late 1950's, and since then have become a popular power source for consumer electronic devices. Significant efforts have been made to develop PV power systems for residential and commercial uses. Conventional fabrication techniques are however expensive and complex. Polymeric photovoltaics present the possibility of producing coatings that function as sunlight-harvesting paints on roofs to produce electricity from sunlight, although the charge transfer mechanisms in conjugated polymers are more complex than those of conventional crystalline PV materials.[34]

In photovoltaic conjugated polymers, such as polythiophenes and PPV derivatives, incident light creates excitons in the polymer. The exciton can be split into its constituent parts at electrodes with holes being collected at the anode and electrons at the cathode. However the exciton splitting process at the polymer-electrode interface is not very efficient and impurities can also act as traps. In order to improve device efficiency, new conducting polymer species that contain electron-donating and electron-accepting species have been developed.[35] Interfaces among conducting polymer molecules of differing electron affinities also enhance the probability of electron transfer between molecules.[36] This process (photoexcited charge transfer) causes the bound charges to separate, and the junction formed at the donor–acceptor interface is analogous to a semiconductor heterojunction. Interpenetrating networks formed from mixtures of two semiconducting polymers likewise allow for the short lifetime of excitons and can provide both the spatially distributed interfaces necessary for efficient charge photo-generation, and the means for separately collecting the electrons and holes.[37] The highest efficiencies achieved to date for conjugated polymer/methanofullerene blend based PV systems are < 3 %,[38] while efficiencies of 6% have been achieved for commercial amorphous silicon-based PV systems and up to 30% for two-junction GalnP/GaAs systems.[39]

1.2.6 Conjugated Polymer Nanowires

Semiconducting nanowires and nanotubes are a new class of one-dimensional (1-D) nanostructures that represent attractive building blocks for nanoscale electronic and photonic devices.[40-43] Inorganic nanowires have been extensively studied and show great promise for nanoelectronics devices both as device components and also as interconnects.[44] Interest in the ability to create polymer based semiconducting nanowires has also increased greatly and a wide variety of potential applications have been envisaged for such nanowires.[45,46]

A number of techniques have been employed for the large-scale fabrication of polymer nanowires, e.g,, electrospinning and template synthesis. In electrospinning,[47] a charged polymer solution or melt is fed through a small opening or nozzle. Due to its charge, the solution is drawn toward a grounded collecting plate, typically 5 – 30 cm away, as a jet. As the jet travels, the solvent gradually evaporates, and a charged polymer fibre is left to accumulate on the grounded target. The charge on the fibres eventually dissipates into the surrounding environment. This results in a non-woven fibre mat composed of fibres with diameters between 50 nm and 10 μm. If the target is allowed to move with respect to the nozzle position, specific fibre orientations (parallel alignment or a random) can be achieved.

Polymer nanostructures can also be fabricated via electrochemical template synthesis.[48] Here, one surface of a template material such as porous aluminium oxide or polycarbonate filter membrane is coated with a metal film, e.g., via sputter coating, and is then used as the anode of an electrochemical cell. The monomer is present in the plating bath solution and a platinum counter electrode is used. This allows polymer nanowires to be synthesised electrochemically within the pores of the membrane. Synthesis by template wetting is a comparatively new method that relies on the wetting of an inorganic template material such as porous aluminium oxide by a polymer solution or melt.[49,50] Due to the high surface energy of the alumina membrane, a thin surface film rapidly covers the pore walls forming nanotubes with well-defined wall thickness. In order to fabricate nanowires, it is necessary to completely fill these pores with the desired material, e.g., conjugated polymer, and then to liberate the nanowires from the membrane in an undamaged state. This process yields arrays of nanowires with good control over structural parameters such as diameter, length and areal density.

From a fundamental viewpoint, the reduced dimensionality of nanowires may enhance the ordering and alignment of conjugated polymer chains within the structures, which might have advantageous effects, e.g., on the electrical performance of nanowire based devices. Applications potentially include highly sensitive sensors, due to the large surface to volume ratio of nanowires, polarised light emitters and nanoscale FETs.[51,52]

1.3 Nanocrystals

1.3.1 Nanocrystals

Nanocrystals are a form of matter which straddle the realm of quantum and classical physics and have been dubbed "artificial atoms".[53] While a host of synthesis methods have been developed to produce these artificial atoms, it is worth bearing in mind that similar structures have been naturally created for aeons. Examples are the formation of opals whose iridescence arises from Bragg diffraction of light by the regular lattice of silica particles and the biological formation of virus crystals. Also, medieval artisans unknowingly became nanotechnologists when they made red stained glass by mixing gold chloride into molten glass. That created tiny gold spheres, which absorbed and reflected sunlight in a way that produces a rich ruby colour. Hence, the rose colour in older cathedral stained glass windows is a result of the strong absorption of gold nanoparticles while silver nanoparticles are responsible for the bright yellow hue. The recent advances in the chemical synthesis of nanoparticles allow far greater precision to be exerted in the fabrication process in terms of particle size, shape and crystallinity. This is signified by the description of such nanostructures as nanocrystals, and indeed their crystalline structure, with clearly defined lattice planes, has been characterised. By contrast, the term nanoparticle indicates either a crystalline or an amorphous entity.[54] Size control is especially significant, as nanocrystals have properties that are critically dependent on their size.

Nanocrystals have demonstrated potential for a great range of applications, from catalysts to novel optoelectronic and electronic devices. Recently the use of nanoparticles for medical applications has been developed, both in diagnostics and therapy. Nanocrystals have been used as ultra-sensitive markers for the investigation of genetic mutations while there are promising cancer therapeutics predicted also.[55,56] Current dyes used for lighting up protein and DNA molecules fade quickly, but semiconductor quantum dots can allow tracking of biological reactions in living cells for days or longer.[57] Also, metal nanocrystals passivated with organic ligand shells show great potential for a range of applications. This has generally lead to a great interest in the electronic properties of isolated nanocrystals and arrays of nanocrystals.[58]

With the development of scanning probe microscopy and the ability to image and measure at the nanoscale, it has become possible to analyse individual nanocrystals as well as arrays of nanocrystals. Assembly of nanoparticles into superlattices is of great interest in the design of nanoelectronic devices based on, e.g., single electron tunneling. Precise control over nanocrystal size, shape, crystal structure and surface chemistry permits the self-assembly of nanocrystals into close-packed solids. Superlattices of nanocrystals may serve as model

systems for the investigation of fundamental physics especially relating to electron transport through the solid.

1.3.2 Metal Nanocrystal Synthesis and Assembly of Nanocrystal Arrays

Metal nanoparticles can be synthesised by both physical and chemical methods. Physical methods include sputtering, which can produce, e.g., gold nanoparticles of various sizes deposited on solid surfaces. Chemical synthesis is more popular as it provides the ability to precisely control the size, shape and dispersity of nanoparticles.[59-62] Production of gold nanoparticles with narrow size distributions is possible, for example, by reduction of a tetrachloroaurate solution in the presence of organic compounds incorporating thiol functionality.[63,64] 5 nm gold nanoparticles have been synthesised in such a manner with a mercaptophenol stabilising ligand.[64] Other methods, which provide for the synthesis of nanoparticles of varying size and stabilising functionality, are also available in the literature.[65,66]

The solution phase chemical synthesis of monodisperse, high quality colloidal nanocrystals typically exploits a temporally discrete nucleation event followed by slower controlled growth on the existing nuclei; see Figure 1.10. Rapid addition to the reaction vessel raises the precursor concentration above the nucleation threshold. A short nucleation burst partially relieves the supersaturation. As long as the consumption of feedstock by the growing colloidal nanocrystals is not exceeded by the rate of precursor addition to the solution, no new nuclei form. As the growth of all nanocrystals is similar, the initial size distribution is largely determined by the time over which the nuclei are formed and begin to grow. A coarse tuning of the average crystal size is possible by controlling the ratio of capping groups to the metal precursor. A second, distinct growth phase known as Ostwald ripening is often observed. In this process the high surface energy of the small nanocrystals promotes their dissolution, whereas material is redeposited on the larger nanocrystals. Thus, the average nanocrystal size increases over time with a complementary decrease in nanocrystal number. The judicious exploitation of the Ostwald ripening process can simplify the preparation of a size series of nanocrystals.

In order to produce a monodisperse (standard deviation, $\sigma < 15$ %) distribution of nanocrystals, further processing is required. This is referred to as size-selective precipitation and involves the titration of a non-solvent into the dispersion to initiate a gradual flocculation. Larger nanocrystals in the size distribution tend to aggregate to the exclusion of smaller nanocrystals as they experience greater attractive van der Waals forces. Partial flocculation of

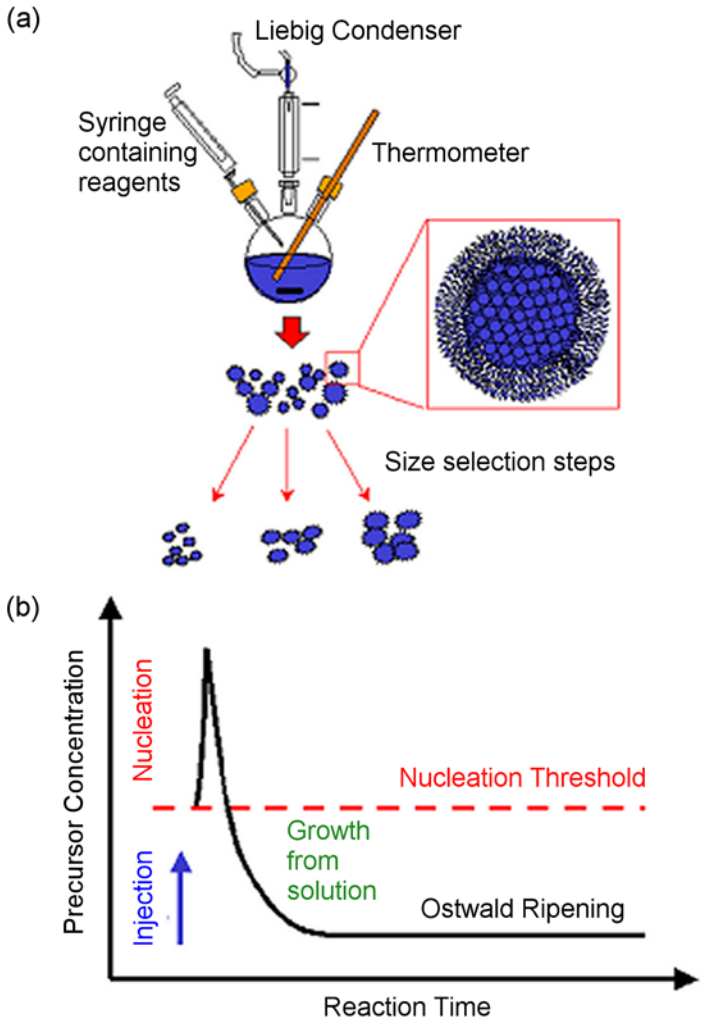

Figure 1.10. (a) Experimental approach for the chemical synthesis of metal nanocrystals. (b) Schematic graph displaying the relationship between the precursor concentration and the reaction time for the solution phase synthesis process.

the dispersion leads to the isolation of a precipitate enriched in the larger nanocrystals after the solution is filtered and centrifuged. The smaller nanocrystals remain dispersed in the supernatant and are retained. The precipitate of larger nanocrystals can be redispersed in a suitable solvent, allowing further iterations of the destabilisation/redispersion procedure to further narrow the size distribution. Similarly, a second size dispersion can be obtained by the addition of more non-solvent to the decanted supernatant to flocculate the remaining nanocrystals. Repeated selection steps result in a range of size fractions. Slower destabilisation leads to more efficient separations of the sizes, yielding size fractions of nanocrystals with standard deviations as small as $\sigma \sim 5$ %, which is well within the accepted threshold of monodispersity.

For a chemical synthesis process to be successful, it must yield readily processible, isolated, purified nanocrystals that can be stored in solution. Due to the heightened surface area to volume ratio of nanocrystals relative to the bulk material, they are far more prone to decomposition. With such a significant amount of the nanocrystal atoms residing on the surface, the melting point is greatly reduced and they are inherently more reactive. Chemisorption of organic ligands onto the surface of the nanocrystals is required in order to counteract the tendency of the bare nanocrystals to aggregate as well as to permit further handling.

The presence of stabilising agents during growth is necessary to prevent aggregation and precipitation of the nanocrystals. When the stabilising molecules are chemically attached to the nanocrystal surface as a monolayer, they are referred to as capping groups. Once an initial capping group has been attached to the nanocrystal surface it is possible to later exchange that capping group. This process is known as ligand exchange. It is also possible to tailor the capping groups such that the new capping layer imbues the nanocrystals with enhanced functionality such as favourable solubility in solvents or binding to a particular target molecule. These modifications of the basic nanocrystal suggest applications for modified nanocrystals in such fields as nanoelectronics, chemical sensing and catalysis. The use of ligand exchange to alter the dimensions of the capping layer surrounding the nanocrystal also allows for variations in the minimum inter-particle spacing in nanocrystal assemblies.

A distinctive feature of nanocrystals is that a discrete set of the number of atoms organises to form an individual nanocrystal, which allows for the size-selective precipitation outlined above. Very small nanocrystals tend to form faceted polyhedral structures as opposed to perfect spheres, such as a cuboctahedron (an octahedron truncated by a cube); see Figure 1.11. This realisation is encapsulated in the term “magic numbers”, which correspond to the number of atoms comprising the nanocrystal. “Magic number” clusters consist of a single central atom, surrounded by successive filled shells. For each new shell n, $10n^2 + 2$ atoms are added to the nanocrystal. The magic numbers for cuboctahedral structures are 1, 13, 55, 147, 309, 561, 923, 1415, 2057, etc.[67,68] Studies by Boyen et al. using X-ray photoelectron spectroscopy reveal that Au_{55} nanocrystals are particularly stable and are also slow to oxidise.[69] A 4 nm diameter nanocrystal contains approximately 2000 atoms and may exhibit regular features. Larger nanocrystals (~ 10 nm) are considered to be roughly spherical.

Ligand stabilised nanoparticles can self-assemble into 2-D and 3-D superlattices. These self-assembled arrays have great potential in future nanocrystal based devices. Nanoparticles are typically dispersed onto a substrate from solvent and the solvent is allowed to evaporate off

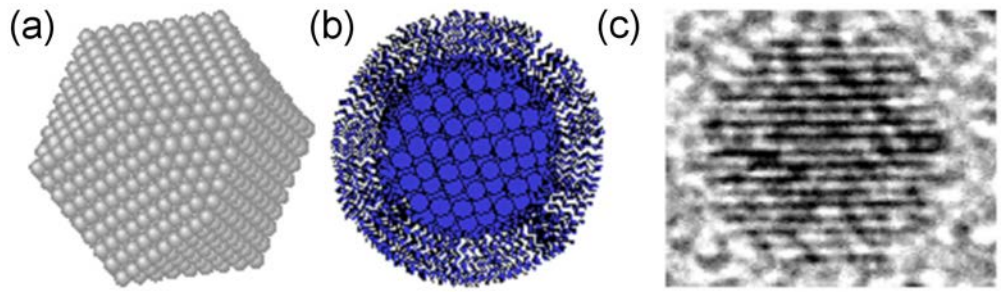

Figure 1.11. (a) Illustration of a cuboctahedral nanocrystal containing the magic number of 2057 atoms. (b) Illustration of a nanocrystal with a protective organic ligand shell. (c) TEM image of a ~ 4 nm $CoPt_3$ nanocrystal, containing roughly the same number of atoms as the illustration in 1.12(a).

in a controlled manner, leaving a self-assembled array of nanoparticles on the substrate. The resulting arrays are typically characterised using TEM, SEM and AFM. Some local disorder and voids in the array are inevitable. Factors that influence the self-assembly of nanocrystals into ordered arrays including the deposition procedure, substrate, stabilising ligand used, finite size dispersion of the nanocrystals and dewetting of the solvents during the self-assembly process. Techniques that have been implemented to minimise these defects include allowing the solvent to evaporate off in a solvent rich environment and using a mixture of solvents and nonsolvents, which slowly destabilises the dispersion as the solvent evaporates. Tailoring the dispersal medium to satisfy the following criteria regarding polarity and boiling point permits the assembly of 3-D arrays of nanocrystals ordered over hundreds of microns: The polarity is such that the interactions between the nanocrystals become mildly attractive as the solvent evaporates and the concentration of the dispersion increases, while the boiling point is selected to permit sufficient time for the nanocrystals to establish equilibrium lattice positions prior to the total evaporation of the solvent. The use of monodisperse nanocrystals is required to produce highly ordered arrays. The chemical synthesis and size selective precipitation procedure outlined above yields highly monodisperse nanocrystals, which are suitable for the creation of such ordered arrays. Under such circumstances, the electronic coupling between nanocrystals and the ensemble properties of the superlattice can be investigated. It is also possible to create binary superlattices for example, binary superlattices of Fe_2O_3 and PbSe nanocrystals in a variety of compositional ratios have been fabricated, which retain the magnetic and semiconducting properties of the individual constituents in the superlattice.[70]

1.3.3 Electronic Properties of Isolated Nanocrystals

Isolated nanocrystals have charging energies that are critically dependent on their size, as indicated by the relation: $E_c = e^2/2C$, where C is dominated by the self-capacitance, $C_0 = 4\pi\varepsilon\ \varepsilon_0\ r$, and where ε_0 is the permittivity of free space, ε is the dielectric constant (typically between 2

and 3 for organic ligands), and r is the radius of the nanocrystal. The charging energy is the energy required to remove an electron from one electrostatically neutral particle. For a metal nanocrystal with a diameter d = 10 nm, $C \approx 1.5$ aF. This gives an activation energy $E_c \approx 50$ meV. Two conditions are necessary for single electron charging to be observed: Firstly, in order to suppress the thermal fluctuations that can wash out single electron charging effects, the charging energy required to add an extra electron to the nanocrystal needs to be significantly higher than k_BT, *i.e.*, $E_c = e^2/2C >> k_BT$ (k_BT = 25 meV at room temperature). Secondly, the tunnel barriers between the nanocrystal and the leads must be opaque enough to ensure that the electron remains localised on the nanocrystal. The condition to be satisfied here is for the tunnel resistance to be greater than the "resistance quantum", given by $R_Q = h/e^2$ (~ 25.8 kΩ).[67,71,72] Tunnel resistances are typically somewhat larger than R_Q.

The current through an artificial atom with very small self-capacitance can vary by many orders of magnitude when its charge is changed by a single electron.[54] If a nanocrystal is charged by only one excess electron, its electric potential will rise to prevent further charging, a process known as "Coulomb blockade".[67,71] To add a charge Q to a neutral metallic "island" requires energy $Q^2/2C$, where C is the total capacitance between the island and the rest of the system, i.e., the leads. In the context of a nanocrystal, the energy of an electron must exceed the Fermi energy by $e^2/2C$, where e is the electronic charge, in order to tunnel on to the nanocrystal. Similarly, for a hole to tunnel, its energy must be $e^2/2C$ below the Fermi energy. The gap in the tunneling spectrum, e^2/C, is the difference between the "electron affinity" required to add an electron and the "ionisation potential" required to remove an electron that arises from electron-electron interactions caused by Coulomb repulsion.[54] This energy barrier to charge transport is called "Coulomb blockade", given by the Coulomb energy e^2/C. By applying $|V_{bias}| > e/2C$ to the single nanocrystal, sufficient energy is provided to lift the Coulomb blockade. The voltage interval $[-e/2C, +e/2C]$ over which conductance is suppressed is referred to as the "Coulomb gap".[54,73]

Scanning probe microscopy (SPM) and scanning tunneling spectroscopy (STS) techniques have been used to obtain topographic and electronic properties of individual nanocrystals on conductive surfaces. The system composed of a tip and a nanocrystal can be modelled as two tunnel junctions in series, with one adjustable junction between the tip and the nanocrystal and a fixed junction between the nanocrystal and the substrate. Amongst the measurements made have been the determination of the Coulomb barriers, the density of states in nanocrystals, discreteness of electron states, the workfunction and separation distances provided by ligand shells.[67] Single electron tunneling to individual nanocrystals has been observed in the *I-V* characteristics of single unpassivated nanocrystals tethered to a dithiol self-assembled

monolayer on a gold substrate probed with an STM.[74] Steps in the tunnel current at voltages greater than the threshold voltage have also been observed and have been ascribed to the "Coulomb staircase" phenomenon, which reflects the addition of further electrons to the isolated nanoparticle. Repeatable, reversible Coulomb staircase behaviour has also been reported for 28 kDa alkanethiolate passivated Au nanocrystals on an Au substrate measured using an STM tip as the nanocontact to the nanocrystal at 83 K.[75] While the requirement for the stepwise charging energy ($E_C = e^2/2C$) to greatly exceed the thermal energy k_BT means that Coulomb staircase behaviour is generally observed at low temperatures where the Coulomb gap is largest, the behaviour may also be observed at room temperature.[74,76]

1.3.4 Electronic Properties of Nanocrystal Assemblies

The electronic properties of nanocrystal assemblies are influenced not only by the properties of each nanocrystal in an array but also by the coupling effects of neighbouring nanocrystals. The mechanisms for conductivity through a nanocrystal superlattice are therefore dependent on many factors including temperature, nanocrystal material and size, ligand type and inter-nanocrystal separation. Typically, nanocrystals within a self-assembled array are weakly coupled, and each member of the lattice is capacitively coupled to its nearest neighbours with possibilities for electron transport, by activated hopping and/or tunneling. Much previous investigation has been conducted on transport through capacitive coupled metal nanocrystals both theoretically and experimentally.[77,78] Measured *I-V* characteristics obtained from weakly coupled assemblies of size-monodisperse nanocrystals have been observed to exhibit non-linearity with a low bias resistance that increases monotonically by several orders of magnitude with decreasing temperature, in contrast to the behaviour expected for a metal. At lower temperatures, non-linearity in the *I-V* curves becomes more acute with the onset of Coulomb blockade. At very low temperatures ($k_BT << E_c$), the density of charge carriers decreases to the extent that the nanocrystals are electrically isolated, and current suppression is observed.[59,79,80] The step-like structure observed in *I-V* measurements of single nanocrystals is washed out in the *I-V* characteristics for nanocrystal assemblies where tunnelling occurs through many nanocrystals in parallel. As with a single nanocrystal, a finite threshold voltage, V_T, is required to generate the charge carriers that will enable current to be passed through the array.[59] Jaeger and co-workers found a correlation between V_T and the length of the nanocrystal array, i.e., a single nanocrystal Coulomb blockade voltage can be estimated based on the length of the array.[79]

1.3.5 Optical Properties of Nanocrystals

Metal nanocrystals possess optical absorption spectra that provide information on their electronic structure.[81-84] They also exhibit characteristic colours depending on their diameters. The theory of (linear) optical absorption of small particles dates back 100 years, when Maxwell's equations were used to solve the interaction of light with nanoparticles.[85] The electronic absorption spectra of nanocrystals with length scales smaller than the wavelength of incident radiation are dominated by the surface plasmon resonance, which for noble metals is strong and lies within the visible region of the spectrum. With respect to nanocrystals, the surface plasmon resonance is a dipolar optical excitation of the entire nanocrystal between the negatively charged free electrons in the nanocrystal and its positively charged core.[58,81,82] For bulk gold, the maximum layer thickness for which this effect is observable is ~ 50 nm. More specifically, the surface plasmon resonance arises from the collective coherent excitation of the free electrons within the conduction band induced by interaction with an electromagnetic field. These excited collective modes of motion of the electron gas are referred to as surface plasmons, and the peak in the absorption spectrum is the resonance frequency for the generation of surface plasmons.

The energy of the surface plasmon resonance is strongly dependent on both the free electron density in the nanocrystal and the dielectric medium (provided by the organic capping ligand and solvent) surrounding the nanocrystal. This dependence on the dielectric medium around the nanocrystals makes it difficult to obtain information about the electronic structure of nanocrystals using plasmon resonance spectroscopy.[58] Alterations to either the surrounding medium dielectric constant and the number of free electrons leads to dramatic changes in the plasmon band. The plasmon resonance is also affected by varying the size of the nanocrystal, shifting to red when the particle diameter is decreased.[58] Whetten and co-workers have also observed that the surface-plasmon band (resonance frequency) in the absorption spectra of gold nanocrystals broadens and decays with decreasing nanocrystal diameter, until the peak disappears for particle diameters < 2 nm.[81] As this point, the density of electronic states is broken up into discrete energy levels as the size of metal nanocrystals is made small. Experiments by Whetten and co-workers also suggest that discrete electronic energy levels in metal nanocrystals can be observed using optical absorption spectroscopy.[81]

1.4 Scanning Probe Microscopy

1.4.1 Scanning Probe Microscopy

Since the invention of the optical microscope, man's ability to image structures at scales beyond those visible to the naked eye has expanded greatly. Some of the major milestones on this path include the development of the scanning electron microscope (SEM), transmission microscope (TEM) and profilometer. These techniques move beyond the resolution limits of conventional optical microscopy by imaging using electron optics or a sharp stylus in the case of the profilometer. While each of these techniques has found widespread application in a wide array of research and technological domains, each suffers from certain limitations. For example, the lateral resolution of the SEM is limited to ~ 5 nm while the TEM can resolve atomic features. Both techniques rely on the interactions of electrons with samples to produce images. However, TEM requires special sample preparation while SEM imaging of insulating samples may cause charging effects that reduce image quality. Neither technique can give reliable vertical measurements. Profilometery is a commonly used technique in microfabrication which can have sub nm vertical resolution but the lateral resolution is typically hundreds of nanometers. Finally, all of these techniques are solely visualisation techniques and do not present many possibilities to conduct local material characterisation at the nanoscale.

Prior to its actual development, the resolution capabilities of the scanning probe microscope were hinted at with the topografiner,[86] which could be considered the first successful SPM and was recognised as such when Binnig and Rohrer's Nobel prize was announced. In this instrument, a field emission current between the tip and sample was employed for feedback control. However, this instrument never achieved the reliable, repeatable atomic resolution that later SPM techniques could deliver for a variety of reasons. Chief among these were the inability to provide adequate vibrational isolation and the lack of computer control, data acquisition and storage systems.

The development of a family of systems ultimately capable of imaging in a range of operational environments with nanometer vertical resolution had to wait for over a decade. However, this new field of microscopy has now found applications in physics (e.g., crystal and surface electronic structure of metals and semiconductors), chemistry (e.g., catalysis, electrochemistry, Langmuir-Blodgett films, polymer morphology), biology (e.g., structure of cells, nucleic acids, proteins and lipids) and many other fields.[87-89]

1.4.2 Scanning Tunneling Microscopy

Following the invention in the early 1980s by Binnig and Roher of the scanning tunneling microscope (STM), the field of scanning probe microscopy has evolved and developed into a huge multiplicity of techniques capable of modifying, probing and characterising materials at the nanoscale.[90-93] All SPM-based imaging techniques are typified by the point-by-point probing of the interaction between an extremely sharp probe and the sample surface. In STM, the electron cloud associated with metal atoms at a surface extends a very small distance above the surface. When a very sharp tip is brought sufficiently close to such a surface, there is a strong interaction between the electron cloud on the surface and that of the tip atom, and an electric tunneling current flows when a small voltage is applied; see Figure 1.12. At a separation of a few atomic diameters, the tunneling current rapidly increases as the distance between the tip and the surface decreases. This rapid change of tunneling current with distance can result in atomic resolution if the tip is raster scanned over the surface to produce an image.

In order to scan the tip over the surface and simultaneously control the probe-sample separation distance a piezoelectric scanner is used. Piezoelectric ceramics are materials that change geometry in a predictable controlled manner on application of a voltage. The voltage applied is proportional to the resulting mechanical movement. Piezoelectric ceramics make it possible to create three-dimensional positioning devices of very high precision. Most SPM systems use tube-shaped piezoelectric ceramics because they combine a simple one-piece construction with high stability and large scan range. Four electrodes cover the outer surface of the tube, while a single electrode covers the inner surface. Application of voltages to one or more of the electrodes causes the tube to bend or to stretch, and hence the sample can be moved in all three dimensions. For example, applying a voltage to one of the four outer quadrants, relative to the centre electrode causes that quadrant to expand and the scanner to tilt away from it (*xy* movement). A corresponding negative voltage applied to the opposite quadrant relative to the centre electrode doubles the *xy* range while preventing vertical motion. Applying a voltage

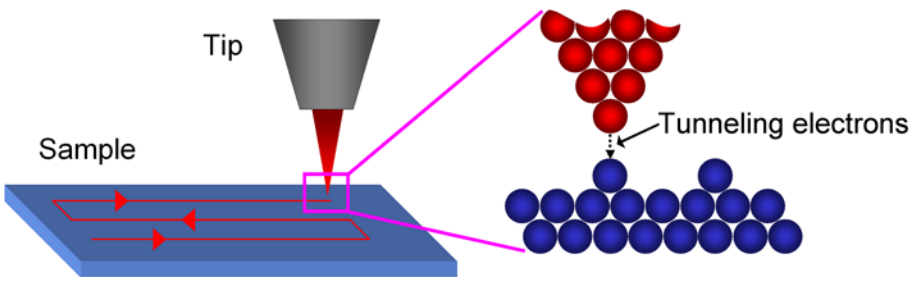

Figure 1.12. Principle of operation of an STM: A sharp metal tip is raster scanned over a sample and the tunneling current between the two is monitored. The magnified view of the region highlighted in pink reveals the tunneling between the atomically sharp tip and the surface atoms of the sample.

to the inner electrode relative to all the outer four electrodes causes the entire tube to expand or contract (*z* movement).

Typically a setpoint tunneling current is defined and as the tip is raster scanned over the sample it encounters changes in sample topography which alter the tip-sample separation leading to changes in tunneling current. Comparing this value to the setpoint yields an error signal, the value of which is utilised as raw data by the associated software. A *z* feedback loop is used to ensure that the tip accurately tracks the surface topography. This continuously compares the detected value to the setpoint and applies a voltage to the scanner in order to adjust the tip position relative to the sample surface in order to reduce the error signal to zero. By plotting the resulting array of *z* feedback data, the topography can be displayed in a meaningful fashion, a false colour image is generated in order to present and analyse the data. As well as allowing extremely high resolution topographic data to be collected, it is also possible to ascertain a great deal of other material characteristics.

1.4.3 Atomic Force Microscopy

One of the critical advances in SPM was the evolution of the atomic force microscope (AFM) from the STM in 1986 by Binnig, Quate and Gerber, which allowed for non conducting samples to be imaged natively.[92] Following on from the development of the AFM, a host of applications beyond simply topographic measurements became apparent as will be discussed later.

AFM utilises a flexible cantilever, with a micromachined probe at its end, with a typical end radius < 20 nm, as a type of spring to measure the force between the tip and the sample; see Figure 1.13. Cantilevers are typically fabricated from silicon nitride or pure silicon using silicon wafers, with photolithography and other microelectronic processing techniques. The ability to batch fabricate the probes results in a large number of near identical probes with similar properties such as spring constant and resonant frequency. The basic principle of an AFM is that the local attractive or repulsive force between the tip and the sample is converted into a bending, or deflection, of the cantilever. The cantilever is attached to a fixed rigid substrate, and depending on whether the interaction at the tip is attractive or repulsive, the cantilever will deflect towards or away from the surface.

The standard detection system for AFM, shown in Figure 1.14, uses a laser beam that is reflected from the back of the cantilever onto a detector in order to monitor the deflections and convert them into an electrical signal. The optical lever principle is used, which means that a small change in the bending angle of the cantilever is converted into a measurably large

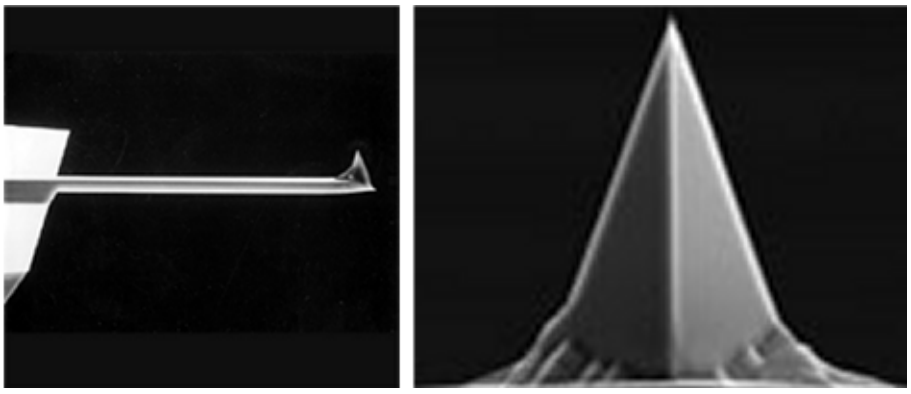

Figure 1.13. Scanning electron microscope image of (a) a flexible cantilever arm of an AFM probe and (b) a high resolution image of the tip of an AFM probe. The probe was fabricated using photolithographic techniques from a standard silicon wafer. Images: Nanosensors, Switzerland.

deflection in the position of the reflected spot. As a result, the system can detect sub-Ångstrom vertical movement at the free end of the cantilever, where the tip is located.

The position of the laser spot is measured by comparing the signals from different sections of the detector. Most AFM systems use a photodiode consisting of four quadrants, so that the laser spot position can be calculated in two directions, by comparing the signals. The vertical deflection (measuring the interaction force) can be calculated by comparing the amount of signal from the top and bottom halves of the detector. The lateral twisting of the cantilever can also be calculated by comparing the left and right halves of the detector.

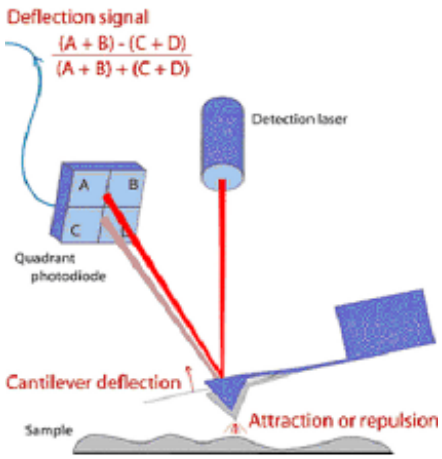

Figure 1.14. Principle of operation of an AFM: A micromachined probe is raster scanned over a sample and the deflections of the probe are monitored using a laser beam that is reflected from the back of the cantilever onto a four quadrant photodetector.

1.4.4 Modes of AFM Operation

As discussed above, the detection system measures the cantilever response as the tip is moved over the surface by the scanning system. In most AFM systems there is also a feedback loop, which adjusts the position of the cantilever above the surface as it is scanned, to take account of the changes in surface height. A value of the cantilever deflection, for example, is selected and then the feedback system adjusts the height of the cantilever base to keep this deflection constant as the tip moves over the surface. This is known as contact mode imaging; see Figure 1.15(a).[92] In contact mode, the tip never leaves the surface, so this mode can be used for very high resolution imaging, such as atomic resolution of inorganic crystals or the images of protein crystals showing the subunits of the proteins. The maximum vertical force is also controlled, so the compression of the sample can be limited. The lateral forces as the tip moves over the surface can be a problem in some situations, but can actually be an advantage in other situations. The lateral deflection can give information about the friction between the tip and the sample, and can show areas that may have the same height, but different chemical properties. In contact mode, the setpoint value is the deflection of the cantilever, so a lower setpoint value gives a lower imaging force.

There are other ways of operating the system, however, using dynamic modes where the cantilever vibrates, and this oscillation of the cantilever is measured rather than the static deflection of the tip. There are also different methods to excite the oscillations - the cantilever substrate can be shaken directly, or a magnetic field can be used to drive the cantilever itself if it is coated with a ferromagnetic layer. In aqueous conditions, the most common technique is to drive the cantilever acoustically through the liquid. In all these cases, however, the measurement of the cantilever oscillation and control systems are the same, and the cantilever is usually driven close to resonance. In these dynamic modes, a setpoint amplitude is chosen, and the height adjusted to match this amplitude through the feedback system. In addition to the height and error signal information from this constant amplitude mode, the phase between the drive signal and the cantilever can also be measured. There are several different dynamic modes, depending on how often the tip makes contact with the surface during the oscillation cycle.

In tapping mode, the tip is not in contact with the surface for most of the oscillation cycle as the cantilever oscillates and the tip makes repulsive contact with the surface of the sample only at the lowest point of the oscillation; see Figure 1.15(b).[94] The lateral forces can therefore be much lower, and this mode can be used for imaging samples such as molecules that are not firmly stuck down on the surface, without moving them around. The cantilever is usually driven close to a resonance frequency of the system, to give a reasonable amplitude for the oscillation

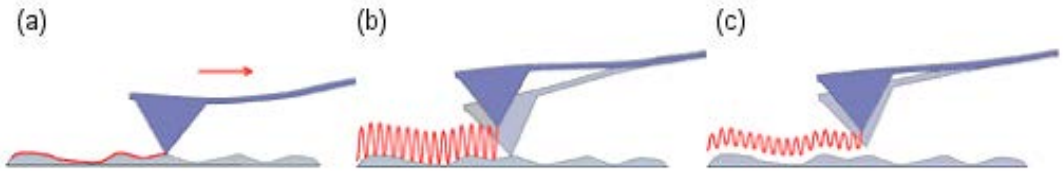

Figure 1.15. The tip sample interactions of the three most commonly used imaging modes in AFM are illustrated above. In contact mode (a), the tip is in permanent contact with the sample, while in tapping mode (b), an oscillating probe tip intermittently makes contact with the sample. (c) In non-contact mode, the cantilever oscillates close to the sample but without making contact with the surface.

and also to provide phase information. The phase of the cantilever oscillation can give information about the sample properties, such as stiffness and mechanical information or adhesion.[94] The resonant frequency of the cantilever depends on its mass and spring constant; stiffer cantilevers have higher resonant frequencies. In tapping mode, the setpoint value is the amplitude of the oscillation, so a higher setpoint value means less damping by the sample and hence lower imaging forces.

In non-contact mode the cantilever oscillates close to the sample surface, but without making contact with the surface; see Figure 1.15(c).[94] The capillary force can make this mode difficult to control in ambient conditions. Very stiff cantilevers are required so that the attraction does not overcome the spring constant of the cantilever, but the lack of contact with the sample means that this mode should cause the least disruption to the sample surface.

As mentioned earlier, the phase between the drive signal and the cantilever can also be measured in AFM mode. Phase imaging is the mapping of the measured phase of the cantilever's periodic oscillations, relative to the phase of the periodic signal that drives the cantilever.[94] Changes in the measured phase correspond to changes in the properties across the sample surface. The technique can be used to map different components in composite materials or to differentiate between regions of high or low surface adhesion. It is important to note that the data acquired from phase imaging is purely qualitative due to inaccurate or unknown spring constants, unknown contact geometry, and contributions from different types of tip-sample interactions. Phase images can be acquired simultaneously with topographic images.

1.4.5 Electrical Characterisation with AFM

Recently, techniques have been developed that can probe the local electrical properties of materials as well as the topography of the material top surface. Specifically, by coating the AFM probe with a thin metal layer, it becomes possible to utilise the probe to explore the electrical properties of samples. Typically, a 25 nm thick double layer of chromium and

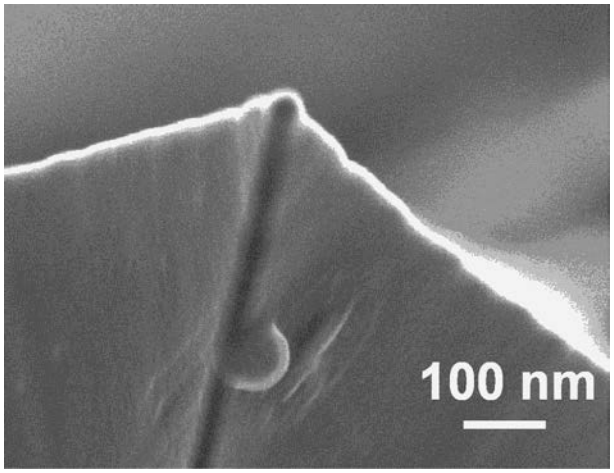

Figure 1.16. High resolution scanning electron microscope image of the apex of a PtIr-coated atomic force microscope (AFM) probe used for both topography and for electrical measurements. The measured probe diameter is ≤ 25 nm; see Chapter 2 for further details.

platinum iridium (PtIr) is deposited on both sides of the cantilever; see Figure 1.16. The tip side coating greatly enhances the conductivity of the tip and allows formation of electrical contacts. The detector side coating enhances the reflectivity of the laser beam by a factor of about 2 and prevents light from interfering within the cantilever. The coating process is optimised for stress compensation and wear resistance with the bending of the cantilever due to stress being less than 3.5% of the cantilever length. The thickness of the coating tapers towards the apex of the tip of the AFM probe and does not greatly alter the imaging resolution of the probe. As the coating the tip apex is quite thin, excessive contact with the sample can cause wear of metal coating. Wear is minimised by imaging in tapping or non-contact mode and avoidance of excessive imaging.

Among the most common of these electrically sensitive techniques based on AFM are scanning capacitance microscopy (SCM), electric force microscopy (EFM), scanning Kelvin probe microscopy (KPM), and conducting-probe AFM (CP-AFM). Scanning capacitance microscopy (SCM) is used to measure capacitance differences between tip and sample while maintaining constant tip sample separation (in non-contact mode) or constant force (in contact mode).[95] The latter is used when a nonconductive layer such as silicon dioxide covers the sample or when tip is intentionally oxidised beforehand.[96,97] Electric force microscopy (EFM) is a secondary imaging mode derived from tapping mode that measures electric field gradient distribution above the sample surface.[98] In a similar manner, scanning Kelvin probe microscopy (KPM) was developed for measuring contact potential difference between the probe and the sample.[99,100]

As metal coated AFM probes are highly conducting, it is possible to directly measure current voltage (*I*-*V*) characteristics of samples locally in the so-called conducting-probe (CP-AFM) configuration. Here the AFM probe is used as a local, nanoscale electrical contact. By ramping the applied voltage between the AFM probe and the sample, the *I*-*V* characteristic can be determined. As it is also possible to acquire topographic information prior to commencing the *I*-*V* measurement, the precise location of the measurement can be ascertained. CP-AFM has been used to investigate charge transport in crystallites of organic semiconductors as well as to investigate the *I*-*V* characteristics of carbon nanotubes and inorganic nanowires.[101-103]

1.5 Scope of This Thesis

The objective of this thesis is the exploration and characterisation of the nanoscale electronic properties of conjugated polymers and nanocrystals.

In Chapter 2, the first application of CP-AFM based *z*-*V* spectroscopy to local measurement of the electronic properties of conjugated polymer thin films is reported. A key advantage of *z*-*V* spectroscopy over conventional current-voltage spectroscopy for measurement of threshold voltages is that the feedback loop remains active during the bias voltage sweep, thus a small increase in the measured current can result in a large relative displacement, allowing precise determination of the charge injection thresholds at both bias polarities. Using this approach, the charge injection thresholds along with corresponding single particle gap energies (E_{gsp}) and exciton binding energies (E_b) are determined for a MEH-PPV thin film. By performing measurements across a grid of locations on the film, a series of exciton binding energy distributions were identified, with peak E_b values ≈ 0.2 eV, 0.4 eV and 0.8 eV, respectively. The variation in measured E_b values is in contrast to the smoothness of the film surface suggesting that the variation may be attributable to differences in the nano-environment of the polymer molecules within the thin film at each measurement location. The method therefore represents a useful tool for local determination of electronic properties of organic materials.

In Chapter 3, it is shown that CP-AFM-based *z*-*V* spectroscopy also permits local, room temperature measurements of the Coulomb blockade voltage thresholds arising from sequential single electron charging of 28 kDa Au nanocrystals in current-carrying paths containing as few as 3 nanocrystals through portions of a nanocrystal array located between the apex of a conducting AFM probe and an underlying Au substrate. It is demonstrated that the fluid-like properties of the nanocrystal arrays enable reproducible formation of nanoscale probe-array-substrate junctions, allowing the influence of background charge on the electronic properties of the array to be identified. Finally, it is shown that the use of CP-AFM allows complementary topography and phase data to be acquired before and after spectroscopy measurements, enabling comparison of local array morphology with local measurements of the Coulomb blockade thresholds. It is suggested that CP-AFM based *z*-*V* spectroscopy could be an extremely valuable technique for characterization and analysis of charge transport through nanocrystal arrays, where specific information regarding the spatial variation of transport thresholds or, e.g., concerning the conductance of ligand molecules, is critically required.

In Chapter 4, it is shown that melt-assisted template wetting is a useful technique for the massively parallel fabrication of conjugated polymer nanowires. The physical and electrical

characteristics of P3HT wires fabricated in this manner are presented. Structural characterisation indicates that the P3HT wires are smooth with a low density of defects. The wires are found to have average lengths of ~ 10 μm and diameters ~ 450 nm while wires with length up to 30 μm are also observed. Extensive radial curvature is observed for the majority of dispersed single wires, indicating appreciable flexibility of these nanostructures. The nanowires are also granular, which suggests partial local dewetting of the molten polymer material from the pore walls during wire formation. Use of CP-AFM for local structural and electronic characterisation of individual nanowires is undertaken. CP-AFM is a useful tool in this regard, as it allows non-invasive characterisation of nanostructures. Two-terminal electrical measurements of individual nanowires, utilising a CP-AFM tip as the source electrode, directly yield values for the intrinsic nanowire resistivity and for the total nanowire-electrode contact resistance. Fits to a thermionic emission-diffusion model also allow the single nanowire hole mobility and the mean nanowire-electrode barrier height to be evaluated. It is proposed that the template wetting method for synthesis of conjugated polymer nanowires may be an important future tool for fabrication of polymer based electronic nanostructures.

In Chapter 5, solution-assisted template wetting is successfully applied to high yield controlled synthesis of F8T2 conjugated polymer nanowires with good control over wire structure and morphology. The physical, electrical and opto-electronic characteristics of wires fabricated in this manner are also presented. Structural characterisation indicates that the discrete F8T2 wires are smooth with a low density of defects. The wires are found to have average lengths of ~ 15 μm and diameters ~ 200 nm. However wires with lengths up to 50 μm are also observed. As expected, structural data point to a low degree of crystallinity within the wires. Individual nanowires are electrically interfaced using top or bottom contact geometries. Current-voltage characteristics acquired for single nanowire devices indicate barrier formation at the nanowire-electrode interfaces and the range of the measured resistivity values, 7×10^3 Ωm < ρ < 4×10^4 Ωm, suggests (unintentional) doping, possibly arising from air exposure. The first report of single F8T2 nanowires as ultra-miniature photodetectors is also presented. Measurements of single nanowires yield external quantum efficiencies ~ 0.1 % under monochromatic illumination, comparable with previously reported data for single inorganic nanowire devices. The single nanowire responsivity ~ 0.4 mA/W is found to be in good agreement with measured responsivity values for large area F8T2 phototransistors and is also competitive with responsivities extracted for inorganic nanowires under similar conditions. These results demonstrate the promise of these one-dimensional polymer nanostructures as sub-wavelength photodetectors with potential for integration into future nanophotonic devices.

The thesis concludes with a summary of the key results achieved in this work.

1.6 References

1. Chiang, C. K.; Fincher, Jr., C. R.; Park, Y. W.; Heeger, A. J.; Shirakawa, H.; Louis, E. J.; Gau, S. C.; MacDiarmid, Alan G. "Electrical Conductivity in Doped Polyacetylene", *Phys. Rev. Lett.* **1977**, *39*, 1098-1101.

2. Burroughes, J. H.; Bradley, D. D. C.; Brown, A. R.; Marks, R. N.; Mackay, K.; Friend, R. H.; Burns, P. L.; Holmes, A. B. "Light-Emitting Diodes Based on Conjugated Polymers", *Nature* **1990**, *347*, 539-541.

3. He, Y.; Kanicki, J. "High-Efficiency Organic Polymer Light-Emitting Heterostructure Devices On Flexible Plastic Substrates", *Appl. Phys. Lett.* **2000**, *76*, 661-663.

4. Sirringhaus, H.; Tessler, N.; Friend, R. H. "Integrated, High-Mobility Polymer Field-Effect Transistors Driving Polymer Light-Emitting Diodes", *Synth. Met.* **1999**, *102*, 857-860.

5. Sirringhaus, H.; Tessler, N.; Friend, R. H. "Integrated Optoelectronic Devices Based on Conjugated Polymers", *Science*, **1998**, *280*, 1741-1744.

6. Merlo, J. A.; Frisbie, C. D. "Field Effect Conductance Of Conducting Polymer Nanofibers", *J. Polym. Sci. Pol. Phys.* **2003**, *41*, 2674-2680.

7. Kim, K.; Jin, J. I. "Preparation of PPV Nanotubes and Nanorods and Carbonized Products Derived Therefrom", *Nano Lett.* **2001**, *1*, 631-636.

8. Bruice, P. Y. *Organic Chemistry*, Prentice-Hall Inc.: New Jersey, **2003**.

9. Turro, N. J. *Modern Molecular Photochemistry*, University Science Books: California, **1991**.

10. Bredas, J. L.; Cornil, J.; Beljonne, D.; dos Santos, D. A.; Shuai, Z. "Excited-State Electronic Structure of Conjugated Oligomers and Polymers: A Quantum-Chemical Approach to Optical Phenomena", *Acc. Chem. Res.* **1999**, *32*, 267-276.

11. Pei, J.; Liu, X.-L.; Yu, W.-L.; Lai, Y.-H.; Niu, Y.-H.; Cao, Y. "Efficient Energy Transfer to Achieve Narrow Bandwidth Red Emission from Eu^{3+}-Grafting Conjugated Polymers", *Macromol.* **2002**, *35*, 7274-7280.

12. Murata, K.; Shimoi, Y.; Abe, S.; Kuroda, S.; Noguchi, T.; Ohnishi, T. "Photogenerated Polarons in Poly(paraphenylene vinylene)", *Chem. Phys.* **1998**, *227*, 191-201.

13. Shimoi, Y.; Abe, S. "Competition Between Polarons and Bipolarons in Nondegenerate Conjugated Polymers", *Phys. Rev. B* **1994**, *50*, 14781-14784.

14. Jenekhe, S. A.; Osaheni, J. A. "Excimers and Exciplexes of Conjugated Polymers", *Science* **1994**, *265*, 765-768.

15. Blatchford, J. W.; Gustafson, T. L.; Epstein, A. J.; VandenBout, D. A.; Kerimo, J.; Higgins, D. A.; Barbara, P. F.; Fu, D. K.; Swager, T. M.; MacDiarmid, A. G. "Spatially and Temporally Resolved Emission from Aggregates in Conjugated Polymers", *Phys. Rev. B* **1996**, *54*, R3683-R3686.

16. Nguyen, T.-Q.; Martini, I.B.; Liu, J.; Schwartz, B. J. "Controlling Interchain Interactions in Conjugated Polymers: The Effects of Chain Morphology on Exciton-Exciton Annihilation and Aggregation in MEH-PPV Films", *J. Phys. Chem. B* **2000**, *104*, 237-255.

17. Braun, D."Electronic Injection and Conduction Processes for Polymer Devices", *J. Polym. Sci, Part B: Polym. Phys.* **2003**, *41*, 2622-2629.

18. Parker, I. D. "Carrier Tunneling and Device Characteristics in Polymer Light-Emitting-Diodes", *J. Appl. Phys.* **1994**, *75*, 1656-1666.

19. Blom, P. W. M.; Vleggaar, M. C. J. M. "Charge Transport in Poly(p-phenylene vinylene) Light-Emitting Diodes", *Mater. Sci. Eng.* **2000**, *27*, 53-94.

20. Shen, Y.; Hosseini, A. R.; Wong, M. H.; Malliaras, G. G. "How to Make Ohmic Contacts to Organic Semiconductors", *ChemPhysChem* **2004**, *5*, 16-25.

21. Wolf, U.; Arkhipov, V. I.; Bassler, H. "Current Injection from a Metal to a Disordered Hopping System. I. Monte Carlo Simulation", *Phys. Rev. B* **1999**, *59*, 7507-7513.

22. Bockrath, M.; Markovic, N.; Shepard, A.; Tinkham, M.; Gurevich, L.; Kouwenhoven, L. P.; Wu, M. S. W.; Sohn, L. L. "Scanned Conductance Microscopy of Carbon Nanotubes and Lambda-DNA", *Nano Lett.* **2002**, *2*, 187-190.

23. Stutzmann, N.; Friend, R. H.; Sirringhaus, H. "Self-Aligned, Vertical-Channel, Polymer Field-Effect Transistors", *Science*, **2003**, *299*, 1881-1884.

24. Becker, H.; Burns, S. E.; Friend. R. H. "Effect of Metal Films on the Photoluminescence and Electroluminescence of Conjugated Polymers", *Phys. Rev. B*, **1997**, *56*, 1893-1905.

25. Martin, S. J.; Kambili, A.; Walker, A. B. "Temperature and Field Dependence of the Mobility of Highly Ordered Conjugated Polymer Films", *Phys. Rev. B* **2003**, *67*, art. no. 165214.

26. Sirringhaus, H.; Wilson, R. J.; Friend, R. H.; Inbasekaran, M.; Wu, W.; Woo, E. P.; Grell, M.; Bradley, D. D. C. "Mobility Enhancement in Conjugated Polymer Field-Effect Transistors Through Chain Alignment in a Liquid-Crystalline Phase", *Appl. Phys. Lett.* **2000**, *77*, 406-408.

27. Sirringhaus, H. "Device Physics of Solution-Processed Organic Field-Effect Transistors", *Adv. Mater.* **2005**, *20*, 2411-2425.

28. Hamadani, B. H.; Natelson, D. "Temperature-Dependent Contact Resistances in High-Quality Polymer Field-Effect Transistors", *Appl. Phys. Lett.* **2004**, *84*, 443-445.

29. Street, R. A.; Salleo, A. "Contact Effects in Polymer Transistors" *Appl. Phys. Lett.* **2002**, *81*, 2887-2889.

30. Pope, M.; Kallmann, H. P.; Magnante, P. "Electroluminescence in Organic Crystals", *J. Chem. Phys.* **1963**, *38*, 2042-2043.

31. Tang, C. W.; VanSlyke, S. A. "Organic Electroluminescent Diodes", *Appl. Phys. Rev.* **1987**, *51*, 913-915.

32. Hamilton, M. C.; Martin, S.; Kanicki, J. "Thin-Film Organic Polymer Phototransistors", *IEEE Trans. Electron. Dev.* **2004**, *51*, 877-885.

33. Zen, A.; Neher, D.; Bauer, C.; Asawapirom, U.; Scherf, U.; Hagen, R.; Kostromine, S.; Mahrt, R. F. "Polarization-Sensitive Photoconductivity in Aligned Polyfluorene Layers", *Appl. Phys. Lett.* **2002**, *80*, 4699-4701.

34. Brabec, C. J.; Sariciftci, N. S.; Hummelen, J. C. "Plastic Solar Cells", *Adv. Func. Mater.* **2000**, *11*, 15-26.

35. Wallace, G. G.; Dastoor, P. C.; Officer, D. L.; Too C. O. "Conjugated Polymers: New Materials for Photovoltaics", *Chemical Innovations* **2000**, *30*, 14-23.

36. Granstrom, M.; Petritsch, K.; Arias, A. C.; Lux, A.; Andersson, M. R.; Friend, R. H. "Laminated Fabrication of Polymeric Photovoltaic Diodes", *Nature* **1998**, *395*, 257-260.

37. Halls, J. J. M.; Walsh, C. A.; Greenham, N.; Marseglia, E. A.; Friend, R.; Moratti, S. C.; Holmes, A. "Efficient Photodiodes from Interpenetrating Polymer Networks", *Nature*, **1995**, *376*, 498-500.

38. Shaheen, S. E.; Brabec, C. J.; Sariciftci, N. S.; Padinger, F.; Fromherz, T.; Hummelen, J. C. "2.5% Efficient Organic Plastic Solar Cells", *Appl. Phys. Lett.* **2001**, *78*, 841-843.

39. Bertness, K. A.; Friedman, D. J.; Kurtz, S. R.; Kibbler, A. E.; Kramer, C.; Olson, J. M. "High-Efficiency GaInP/GaAs Tandem Solar Cells", *IEEE AES Systems* **1994**, *9*, 12-17.

40. Duan, X.; Huang, Y.; Cui, Y.; Lieber. C. M. In *Molecular Nanoelectronics*; Reed, M. A.; Lee, T., Ed.; American Scientific Publishers, California, **2003,** 199–227.

41. Huang, Y.; Lieber, C. M. "Integrated Nanoscale Electronics and Optoelectronics: Exploring Nanoscale Science and Technology Through Semiconductor Nanowires", *Pure Appl. Chem.* **2004**, *76*, 2051-2068.

42. Law, M.; Goldberger, J.; Yang, P. "Semiconductor Nanowires and Nanotubes", *Annu. Rev. Mater. Sci.* **2004**, *34*, 83-122.

43. Yao, Z.; Dekker, C.; Avouris, P. "Electrical Transport Through Single-Wall Carbon Nanotubes", *Top. Appl. Phys.* **2001**, *80*, 147-171.

44. Barrelet, C. J.; Greytak, A. B.; Lieber, C. M. "Nanowire Photonic Circuit Elements", *Nano Lett.* **2004**, *4*, 1981-1985.

45. Merlo, J. A.; Frisbie, C. D. "Field Effect Transport and Trapping in Regioregular Polythiophene Nanofibers", *J. Phys. Chem. B* **2004**, *108*, 19169-19179.

46. Liu, H.; Reccius, C. H.; Craighead, H. G. "Single Electrospun Regioregular Poly(3-hexylthiophene) Nanofiber Field-Effect Transistor", *Appl. Phys. Lett.* **2005**, *87*, art. no. 253106.

47. MacDiarmid, A. G.; Jones Jr., W. E.; Norris, I. D.; Gao, J.; Johnson Jr., A. T.; Pinto, N. J.; Hone, J.; Han, B.; Ko, F. K.; Okuzaki, H.; Llaguno, M. "Electrostatically-Generated Nanofibers of Electronic Polymers", *Synth. Met.* **2001**, *119*, 27-30.

48. Martin, C. R. "Nanomaterials a Membrane-Based Synthetic Approach", *Science*, **1994**, *266*, 1961-1966.

49. Steinhart, M.; Wendorff, J. H.; Greiner, A.; Wehrspohn, R. B.; Nielsch, K.; Schilling, J.; Choi, J.; Gösele, U. "Polymer Nanotubes by Wetting of Ordered Porous Templates", *Science* **2002**, *296*, 1997.

50. Hulteen, J. C.; Martin, C. R. "A General Template-Based Method for the Preparation of Nanomaterials", *J. Mater. Chem.* **1997**, *7*, 1075-1087.

51. Joo, J.; Kim, B. H.; Park, D. H.; Kim, H. S.; Seo, D. S.; Shim, J. H.; Lee, S. J.; Ryu, K. S.; Kim, K.; Jin, J. I.; Lee, T. J.; Lee, C. J. "Fabrication and Applications of Conducting Polymer Nanotube, Nanowire, Nanohole, and Double Wall Nanotube", *Synth. Met.* **2005**, *153*, 313-316.

52. Huang, J.; Virji, S.; Weiller, B. H.; Kaner, R. B. "Polyaniline Nanofibers: Facile Synthesis and Chemical Sensors", *J. Am. Chem. Soc.* **2003**, *125*, 314-315.

53. Kastner, M.A. "Artificial Atoms", *Phys. Today* **1993**, *46*, 24-31.

54. Halperin, W. P. "Quantum Size Effects in Metal Particles", *Rev. Mod. Phys.* **1986**, *58*, 533-606.

55. Murphy, D.; Redmond, G. "Optical Detection and Discrimination of Cystic Fibrosis-Related Genetic Mutations Using Oligonucleotide-Nanoparticle Conjugates", *Anal. Bioanal. Chem.* **2005**, *381*, 1122-1129.

56. Loo, C.; Lin, A.; Hirsch, L.; Lee, M. H.; Barton, J.; Halas, N.; West, J.; Drezek, R. "Nanoshell-Enabled Photonics-Based Imaging and Therapy of Cancer", *Technol. Cancer. Res. T.* **2004**, *3*, 33-40.

57. Chan, W. C. W.; Nie, S. "Quantum Dot Bioconjugates for Ultrasensitive Nonisotopic Detection", *Science* **1998**, *281*, 2016-2018.

58. Murray, C. B.; Kagan, C. R.; Bawendi, M. G. "Synthesis and Characterisation of Monodisperse Nanocrystals and Close-Packed Nanocrystal Assemblies", *Annu. Rev. Mater. Sci.* **2000**, *30*, 545-610.

59. Abeles, B.; Sheng, P.; Coutts, M. D.; Arie, Y. "Structural and Electrical Properties of Granular Metal Films", *Adv. Phys.* **1975**, *24*, 407-461.

60. Alivisatos, A. P. "Semiconductor Clusters, Nanocrystals, and Quantum Dots", *Science* **1996**, *271*, 933-937.

61. Turkevich, J.; Stevenson, P. C.; Hillier, J. "A Study of Nucleation and Growth Processes in the Synthesis of Colloidal Gold", *Dicuss. Faraday Soc.* **1951**, *11*, 55-75.

62. Frens, G. "Controlled Nucleation for the Regulation of the Particle Size in Monodisperse Gold Suspensions", *Nature Phys. Sci.* **1973**, *241*, 20-22.

63. Brust, M.; Walker, M.; Bethell, D.; Schiffrin, D. J.; Whyman, R. "Synthesis of Thiol Derivatised Gold Nanoparticles in a Two Phase Liquid-Liquid System", *J. Chem. Soc., Chem. Commun.* **1994**, *15*, 801-802.

64. Brust, M.; Fink, J.; Bethell, D.; Schiffrin, D. J.; Kiely, C. "Synthesis and Reactions of Functionalised Gold Nanoparticles", *J. Chem. Soc., Chem. Commun.* **1995**, *16*, 1655-1656.

65. Brown, K.; Natan, M. J. "Hydroxylamine Seeding of Colloidal Au Nanoparticles in Solution and on Surfaces", *Langmuir* **1998,** *14*, 726-728.

66. Green, M.; O'Brien, P. "A Simple One Phase Preparation of Organically Capped Gold Nanocrystals", *J. Chem. Soc., Chem. Commun.* **2000**, *21*, 183-184.

67. Schön, G.; Simon, U. "A Fascinating New Field in Colloid Science: Small Ligand-Stabilised Metal Clusters and their Possible Application in Microelectronics", *Colloid Polym. Sci.* **1995**, *273*, 101-117, 202-218.

68. Thomas, P. J.; Kulkarni, G. U. "From Colloids to Nanotechnology: Investigations on Magic Nuclearity Palladium Nanocrystals", *Curr. Sci. India* **2003**, *85*, 1760-1766.

69. Boyen, H. G.; Kastle, G.; Weigl, F.; Koslowski, B.; Dietrich, C.; Ziemann, P.; Spatz, J. P.; Riethmuller, S.; Hartmann, C.; Moller, M.; Schmid, G.; Garnier, M. G.; Oelhafen, P. "Oxidation-Resistant Gold-55 Clusters", *Science* **2002**, *297*, 1533-1536.

70. Redl, F. X.; Cho, K.-S.; Murray, C. B.; O'Brien, S. " Three-Dimensional Binary Superlattices of Magnetic Nanocrystals and Semiconductor Quantum Dots", *Nature* **2003**, *423*, 968-971.

71. Simon, U. "Charge Transport in Nanoparticle Arrangements", *Adv. Mater.* **1998**, *10*, 1487-1492.

72. Matagne, P.; Leburton J. P. In *Quantum Dots and Nanowires*; Bandyopadhyay, S.; Nalwa, H. S., Ed.; American Scientific Publishers, **2003**, 1-66.

73. Parak, W. J.; Manna, L.; Simmel, F. C.; Gerion, D.; Alivisatos, A. P. In *Nanoparticles – From Theory to Applications*; Schmid, G., Ed.; Wiley-VCH, Weinheim, **2004**, 4-49.

74. Andres, R. P.; Bein, T.; Dorogi, M.; Feng, S.; Henderson, J. I.; Kubiak, C. P.; Mahoney, W. J.; Osifchin, R. G.; Reifenberger, R. ""Coulomb Staircase" at Room Temperature in a Self-Assembled Molecular Nanostructure", *Science* **1996**, *272*, 1323-1325.

75. Ingram, R. S.; Hostetler, M. J.; Murray, R. W.; Schaaf, T. G.; Khoury, J. T.; Whetten, R. L.; Bignioni, T. P.; Guthrie, D. K.; First, P. N. "28 kDa Alkanethiolate-Protected Au Clusters Give Analogous Solution Electrochemistry and STM Coulomb Staircases", *J. Am. Chem. Soc.* **1997**, *119*, 9279-9280.

76. Bigioni, T. P.; Harrell, L. E.; Cullen, W. G.; Guthrie, D. K.; Whetten, R. L.; First, P. N. "Imaging and Tunneling Spectroscopy of Gold Nanocrystals and Nanocrystal Arrays", *Eur. Phys. J. D* **1999**, *6*, 355-364.

77. Middleton, A. A.; Wingreen, N. S. "Collective Transport in Arrays of Small Metallic Dots", *Phys. Rev. Lett.* **1993**, *71*, 3198-3201.

78. Rimberg, A. J.; Ho, T. R.; Clarke, J. "Scaling Behavior in the Current-Voltage Characteristic of One- and Two-Dimensional Arrays of Small Metallic Islands", *Phys. Rev. Lett.* **1995**, *74*, 4714-4717.

79. Parthasarathy, R.; Lin, X. M.; Jaeger, H. M. "Electronic Transport in Metal Nanocrystal Arrays: The Effect of Structural Disorder on Scaling Behaviour", *Phys. Rev. Lett.* **2001**, *87*, art. no. 186807.

80. Black, C. T.; Murray, C. B.; Sandstrom, R. L.; Sun, S. "Spin-Dependent Tunneling in Self-Assembled Cobalt-Nanocrystal Superlattices", *Science* **2000**, *290*, 1131-1134.

81. Alvarez, M. M.; Khoury, J. T.; Schaaff, T. G.; Shafigullin, M. N.; Vezmar, I.; Whetten, R. L. "Optical Absorption Spectra of Nanocrystal Gold Molecules", *J. Phys. Chem. B* **1997**, *101*, 3706-3712.

82. Link, S.; El-Sayed, M. A. "Optical Properties and Ultrafast Dynamics of Metallic Nanocrystals", *Annu. Rev. Phys. Chem.* **2003**, *54*, 331-366.

83. Templeton, A. C.; Pietron, J. J.; Murray, R. W.; Mulvaney, P. "Solvent Refractive Index and Core Charge Influences on the Surface Plasmon Absorbance of Alkanethiolate Monolayer-Protected Gold Clusters", *J. Phys. Chem. B* **2000**, *104*, 564-570.

84. Schaaff, G.; Shafigullin, M. N.; Khoury, J. T.; Vezmar, I.; Whetten, R. L.; Cullen, W. G.; First, P. N.; Gutierrez-Wing, C.; Ascensio, J.; Jose-Yacaman, M. J. "Isolation of Smaller Nanocrystal Au Molecules: Robust Quantum Effects in Optical Spectra", *J. Phys. Chem. B* **1997**, *101*, 7885-7891.

85. Mie, G. "Beiträge zur Optik trüber Medien, Speziell Kolloidaler Metallösungen", *Ann. Phys.* **1908**, *25*, 377-445.

86. Young, R.; Ward, J.; Scire, F. "The Topografiner: An Instrument for Measuring Surface Microtopography", *Rev. Sci. Instrum.* **1972**, *43*, 999-1011.

87. Wildoer, J. W. G.; Venema, L. C.; Rinzler, A. G.; Smalley, R. E.; Dekker, C. "Electronic Structure of Atomically Resolved Carbon Nanotubes", *Nature* **1998**, *391*, 59-62.

88. Frommer, J. "Scanning Tunneling Microscopy and Atomic Force Microscopy in Organic-Chemistry", *Angew. Chem. Int. Edit.* **1992**, *31*, 1298-1328.

89. Li, M. Q. “Scanning Probe Microscopy (STM/AFM) and Applications in Biology”, *Appl. Phys. A Mater.* **1999**, *68*, 255-258.

90. Binnig, G.; Rohrer, H. “Scanning Tunneling Microscopy”, *Helv. Phys. Acta* **1982**, *55*, 726-735.

91. Binnig, G.; Rohrer, H. “Scanning Tunneling Microscopy”, *IBM J. Res. Develop.* **1986**, *44*, 279-293.

92. Binnig, G.; Quate, C. F.; Gerber, C. “Atomic Force Microscope”, *Phys. Rev. Lett.* **1986**, *56*, 930-933.

93. Wiesendanger, R. Scanning Probe Microscopy and Spectroscopy: Methods and Applications, University Press, Cambridge, **1994**.

94. Garcia, R.; Perez, R. “Dynamic Atomic Force Microscopy Methods”, *Surf. Sci. Rep.* **2002**, *47*, 197-301.

95. Williams, C. C.; Hough, W. P.; Rishton, S. A. “Scanning Capacitance Microscopy on a 25 nm Scale”, *Appl. Phys. Lett.* **1989**, *55*, 203-205.

96. Tarun, A. B.; Laniog, J. N.; Tan, J. M.; Cana, P. N. “Junction Leakage Analysis Using Scanning Capacitance Microscopy”, *IEEE Trans. Dev. Mat. Rel*, **2004**, *4*, 46-49.

97. Nakakura, C. Y.; Hetherington, D. L.; Shaneyfelt, M. R.; Shea, P. J.; Erickson, A. N. “Observation of Metal-Oxide-Semiconductor Transistor Operation Using Scanning Capacitance Microscopy”, *Appl. Phys. Lett.* **1999**, *75*, 2319-2321.

98. Girard, P. “Electrostatic Force Microscopy: Principles and Some Applications to Semiconductors”, *Nanotechnology* **2001**, *12*, 485-490.

99. Nonnenmacher, M.; O'Boyle, M. P.; Wickramasinghe, H. K. “Kelvin Probe Force Microscopy”, *Appl. Phys. Lett.* **1991**, *58*, 2921-2923.

100. Martin, Y.; Abraham, D. W.; Wickramasinghe, H. K. “High-Resolution Capacitance Measurement and Potentiometry by Force Microscopy”, *Appl. Phys. Lett.* **1988**, *52*, 1103-1105.

101. Kelley, T. W.; Granstrom, E. L.; Frisbie, C. D. “Conducting Probe Atomic Force Microscopy: A Characterization Tool for Molecular Electronics”, *Adv. Mater.* **1999**, *11*, 261-264.

102. Dai, H. J.; Wong, E. W.; Lieber, C. M. “Probing Electrical Transport in Nanomaterials: Conductivity of Individual Carbon Nanotubes”, *Science*, **1996**, *272*, 523-526.

103. Park, W. I.; Yi, G. C.; Kim, J. W.; Park, S. M. “Schottky Nanocontacts on ZnO Nanorod Arrays”, *Appl. Phys. Lett.* **2003**, *82*, 4358-4360.

Chapter 2

Local Mapping of Electronic Properties in MEH-PPV Thin Films Using Conducting-Probe Atomic Force Microscopy

2.1 Introduction

Conjugated polymers are attractive materials for (opto-) electronics due to their chemically tunable optical and electronic properties, as well as their facility for solution processing.[1-4] The conjugated backbone in these polymers results in formation of delocalised bonding (π) and anti-bonding (π^*) orbitals, analagous to valence and conduction states in inorganic semiconductors. Solution processing methods such as spin coating present both opportunities and challenges for device fabrication. Opportunities include the potential for low-cost fabrication (relative to inorganic semiconductors) as well as for large area deposition of polymer thin films onto both rigid and flexible substrates. Challenges arise from the dependence of the (opto-) electrical properties of polymer thin film devices on polymer processing conditions,[5-9] e.g., polymer concentration, choice of solvent, deposition conditions, environmental effects and the influence of the polymer-substrate interface. In this regard, some of the fundamental mechanisms which govern the interplay between the electronic properties of a polymer thin film and its local morphology remain controversial or poorly understood. Development of a detailed understanding of the local electronic structure of conjugated polymer films is essential in order to make progress towards the ultimate goal of high-performance organic devices.

For semiconducting polymers, the macromolecular analogue of the band gap in inorganic semiconductors is the energy gap between the highest occupied molecular state (HOMO) and the lowest unoccupied molecular state (LUMO). Addition of an electron or hole to a vacant molecular state results in polaron formation due to a local deformation of the polymer around the additional charge. This effectively moves the polaron energy level into the HOMO-LUMO gap. The energy difference between the electron polaron level (E_{p-}) and the hole polaron level (E_{p+}) is known as the single particle energy gap, $E_{gsp} = E_{p-} - E_{p+}$.[10] Combination of a hole polaron with an electron polaron results in formation of an exciton. The exciton binding energy (E_b) can be thought of as the energy which must be supplied to an exciton in order to create a pair of oppositely charged polarons, i.e., $E_b = E_{gsp} - E_a$, where E_a is the excitonic band gap.[11] The value of E_a, which corresponds to the optical absorption edge, can be determined by UV-Vis absorption spectroscopy. Determination of the magnitude and variability of the exciton binding energy in a given conjugated polymer system is of key importance for device applications since, e.g., the magnitude of the singlet exciton binding energy influences the recombination efficiency in emissive devices and also influences the charge separation efficiency in photovoltaic devices.[2]

The singlet exciton binding energy has been investigated using a range of techniques for a number of polymer families, including the widely studied poly(1,4-phenylenevinylene) (PPV). Early work in this area on PPV and its derivatives employed electro-optical spectroscopic techniques such as electroabsorption,[12,13] electroabsorption combined with internal photoemission,[14] and photoconductivity excitation profile spectroscopy.[15,16] A wide range of values have been reported for the exciton binding energy in the PPV family, 55 meV < E_b < 1.1 eV.[12-16] More recently, scanning tunneling microscopy (STM)-based displacement-voltage (*z*-*V*) spectroscopy has been applied to probe the local electronic properties of films of conjugated polymers with layer thicknesses in the range 2-100 nm.[10,17-20] For sharp tips, where geometry-induced field emission dominates charge injection, the alignment of the electron and hole polaron energy levels (relative to the Fermi level of the unbiased electrode) and the single particle energy gap E_{gsp} can be determined.[10,17,18,20] One disadvantage of STM is that it precludes stable imaging of the polymer film topography. In this chapter,[♦] the local determination of the charge injection thresholds for electron (E_{p-}) and hole (E_{p+}) polaron levels and the associated single particle energy gap (E_{gsp}) in poly[2-methoxy-5-(2-ethylhexyloxy)-1,4-phenylenevinylene] (MEH-PPV) using conducting-probe atomic force microscopy (CP-AFM) combined with *z*-*V* spectroscopy is reported. This technique enables direct comparison of measured electronic properties with nanoscale film morphology.

[♦] This work will be published as "Local Mapping of Electronic Properties in MEH-PPV Thin Films Using Conducting-Probe Atomic Force Microscopy", *Nanotechnology* submitted.

2.2 Brief Description of Proposed Approach

Figure 2.1 shows the proposed model for local *z*-*V* spectroscopy on a conjugated polymer thin film. Initially, topographic and phase images are acquired in tapping mode AFM to identify smooth regions of the film. Following selection of a location, the probe is retracted and the microscope is switched into scanning tunneling microscopy (STM) mode for the *z*-*V* spectroscopy measurements. A small bias voltage is applied between the substrate and the metallised probe, and a current setpoint is fixed. The geometry of the probe apex is critical to the performance of the *z*-*V* spectroscopy measurement; it has been shown for extremely sharp probes with apex radii much less than 50 nm that the highest electric field occurs at the probe apex so that this is expected to be the predominant site for charge-carrier injection into the organic thin film.[20] The nominal apex radii of the commercial probes utilised in this work are less than 25 nm and thus satisfy this condition, for example; see Figure 1.16 in Chapter 1.

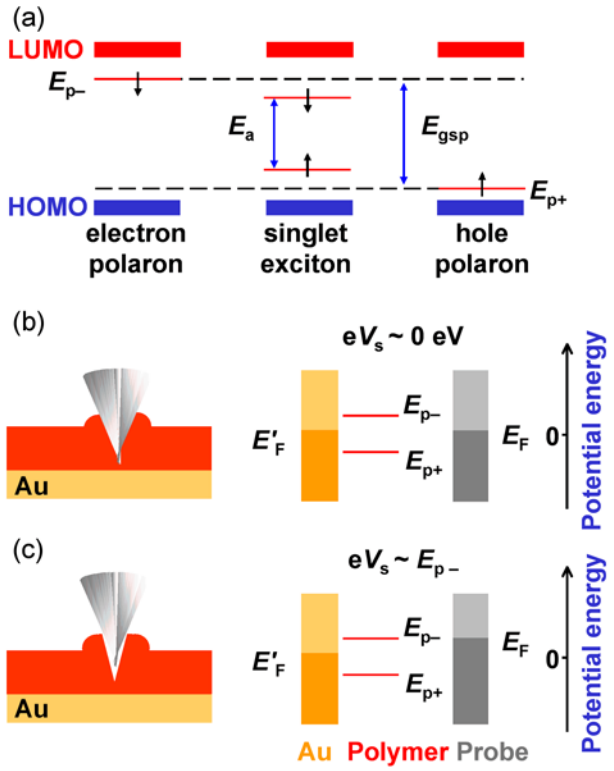

Figure 2.1. (a) Schematic of electron polaron (E_{p-}) and hole polaron (E_{p+}) energy levels. Combination of polarons with opposite charge and spin forms a singlet exciton. (b), (c) Schematic of the probe-polymer-substrate geometry and energy level alignment. At low sample bias, (b), current flow can only occur via non-resonant tunneling through the polymer, hence the tip penetrates into polymer layer. When the substrate bias (V_s) has been made sufficiently large, (c), resonant tunneling through a polaron level results in a sharp increase in local conductance, thus causing the probe to retract in order to maintain the preset tunneling current.

The left hand panel of Figure 2.1(b) shows the situation after the feedback loop has been engaged at a small positive substrate bias. The probe has penetrated into the polymer film until the measured current (I) has reached the setpoint. The right hand panel in Figure 2.1(b) shows the corresponding energy level diagram. In this case, current flow between the probe apex and the substrate occurs via non-resonant tunneling through the polymer, and carrier injection is dominated by field-enhanced injection from the probe apex.[10] Thus, the probe does not penetrate the polymer film completely, but leaves a layer that is several nanometers thick between the probe apex and the substrate. As the substrate bias voltage (V_s) is increased, the relative probe height (z) remains effectively constant due to the quasi-logarithmic dependence of the probe-sample separation on the bias voltage (at constant current).[21]

Figure 2.1(c) shows the situation when the applied bias has been made just large enough to enable resonant tunneling from the probe apex through the electron polaron level in the polymer, i.e., $eV_s = E_{p-}$, where e is the magnitude of the electronic charge. This enhanced tunneling probability results in a dramatic increase in the local conductance.[10] Consequently, the feedback loop causes the probe to retract in order to maintain the current at its setpoint value and the injection threshold appears as a step-like increase in the z-V curve. Similarly, for voltage sweeps at negative bias, the threshold energy for resonant tunneling through the hole polaron level occurs at $|eV_s| = |E_{p+}|$. A key advantage of z-V spectroscopy over conventional I-V spectroscopy for measurement of local charge injection thresholds is that the feedback loop remains active during the bias voltage sweep, thus a small increase in the measured current can result in a large relative displacement, allowing precise determination of carrier injection thresholds at both bias polarities. On the basis of this model, therefore, z-V spectroscopy is expected to enable precise measurements of the positions of the polaron energy levels and the corresponding single particle gap energies in conjugated polymers. Combining these data with values of the excitonic band gap measured by optical absorption spectroscopy thereby permits determination of conjugated polymer exciton binding energies.

2.3 Experimental

Poly[2-methoxy-5-(2-ethylhexyloxy)-1,4-phenylenevinylene] (MEH-PPV) with mean molecular weight M_w > 1,000,000 was purchased from ADS. Inc., Canada, and stored before use in a controlled athmosphere nitrogen glovebox (< 0.1 ppm O_2, H_2O; MBraun, Germany). All other reagents and solvents were purchased from Sigma, and were used without purification. For optical spectroscopy measurements, thin films of MEH-PPV dissolved in tetrahydrofuran (THF, 4 mg/mL) were spun cast onto glass coverslips. UV-Vis absorption spectra were acquired in air using a spectrophotometer (8453E, Agilent Technologies). For *z*-*V* measurements, gold substrates were prepared by vacuum evaporation of metal (Cr 10 nm, Au 100 nm) onto oxidised silicon wafer substrates (*n* type, 2-4 Ωcm, 100 nm thermal oxide), followed by solvent cleaning (trichloroethylene, acetone, isopropyl alcohol) and flame annealing using a butane torch. For each set of *z*-*V* measurements, a fresh 4 mg/mL solution of MEH-PPV in THF was prepared and then spun cast onto the substrates at 6000 rpm for 60 seconds in the nitrogen glovebox, followed by mild annealing (50 °C) under vacuum for 12 hours. The samples were then transferred to a controlled atmosphere scanning probe microscopy system (JSPM 4200, JEOL U.K. Ltd.). The maximum exposure to the laboratory atmosphere was 20 minutes.

Tapping mode atomic force microscopy (AFM) measurements were made under high vacuum (10^{-6} mbar) using commercial tapping mode PtIr metallised probes (NCHPt, Nanosensors, Germany, having typical radius of curvature ~ 10 nm and front/rear cone angles of 22.5 º / 27.5 º, respectively). The AFM probes were cleaned by exposure to a UV source (UV-Tipcleaner, Bioforce Nanoscience Inc., USA) for 15 minutes prior to use. Following topography and phase measurements, a suitable region (i.e., RMS < 1.5 nm / 2 μm^2 area with low phase contrast) of each thin film was selected and *z*-*V* spectroscopy measurements were then performed at a regular orthogonal grid of locations within the region, at pitches of ~ 500 nm. At each location, an initial bias voltage (V_s) of −0.1 V was applied to the substrate (with the probe acting as a virtual ground) and the feedback loop was engaged, causing the probe to approach the substrate until the measured current reached the setpoint (50 pA). The relative probe height (*z*) was then measured as a function of the applied bias (V_s: −0.1 V → −3 V, step 5 mV). At the end of the negative sweep, the probe was withdrawn, the bias voltage setpoint was adjusted to +0.1 V, the feedback loop was re-engaged and the positive polarity sweep (V_s: +0.1 V → +3 V, step 5 mV) was measured. On completion of *z*-*V* spectroscopy measurements, simultaneous topography and phase images of the region were again acquired. For comparison purposes, control *z*-*V* measurements were also performed on bare flame-annealed Au substrates.

2.4 Results and Discussion

2.4.1 Physical Characterisation of Polymer Thin Films

For each set of measurements, fresh solutions of MEH-PPV in tetrahydrofuran were prepared and thin films were spun cast onto glass slides and flame-annealed Au substrates, respectively. Figure 2.2(a) shows a UV-Visible absorption spectrum for a typical film spun cast onto a glass slide. The energy required to create a molecular exciton is the threshold energy for optical absorption, E_a.[10] Taking linear fits to the absorption data at energies below and above the absorption onset, respectively, the absorption threshold is given by the intersection of the two fits, $E_a = 2.08 \pm 0.06$ eV. Figures 2.4(b) and (c) show topography and phase images of a MEH-PPV thin film spun cast onto a flame-annealed Au substrate, acquired prior to *z*-*V* spectroscopy measurements. The data indicated formation of a smooth film with a low density of defects and average RMS roughness of 1.35 ± 0.2 nm for 2×2 μm^2 areas. By comparison, AFM topography measurements of bare flame annealed Au substrates revealed the

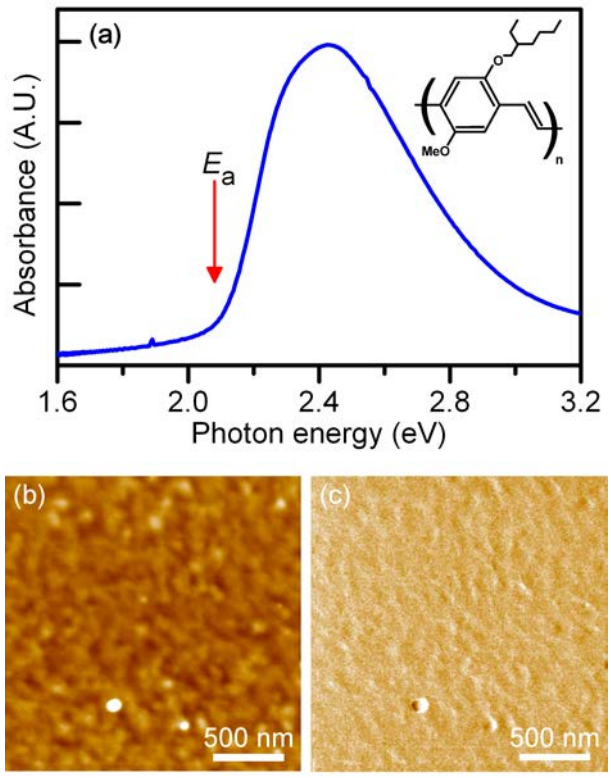

Figure 2.2. (a) Optical absorption spectrum of a thin film of MEH-PPV on glass. The threshold for optical absorption, (E_a) is indicated by the red arrow. The inset shows the chemical structure of MEHPPV. (b) Tapping mode AFM topography image of a 60 nm thick MEH-PPV film spun cast on a flame annealed Au substrate, false colour height scale (*z*): 10 nm, RMS roughness: 1.35 nm. (c) Phase image of the same region indicates a homogenous film, false colour phase scale: 5º, RMS roughness: 1º.

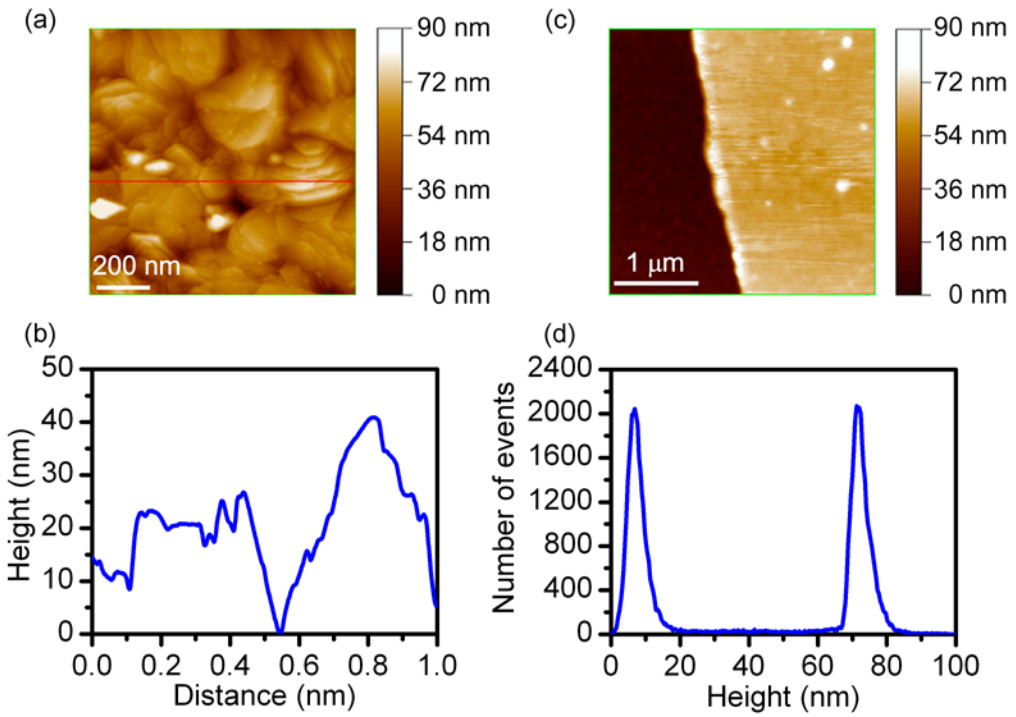

Figure 2.3. (a) Tapping mode atomic force microscope (AFM) images of a flame annealed Au substrate (1 μm × 1 μm) with RMS roughness of 9.8 nm, (b) a line profile reveals plateaus on the surface. (c) Tapping mode AFM image of a gently scratched MEH-PPV thin film on an Au substrate. (d) The height histogram reveals that the polymer film thickness was 60 ± 6 nm.

existence of regions with ~ 100 nm sized flat plateaus. AFM topography measurements on regions of an MEH-PPV film which had been gently scratched to reveal the substrate yielded a mean film thickness of 60 ± 6 nm; see Figure 2.3 (c) and (d).

2.4.2 *z-V* Spectroscopy of Polymer Thin Films

Figure 2.4 shows a typical pair of negative and positive *z-V* curves measured at one location on the MEH-PPV film for which AFM data is shown in Figure 2.2. For the negative bias sweep (eV_s: –0.1 → –3.0 eV), the relative probe height (z) initially increases slowly as a function of the applied bias, by ~ 5 nm over the range –0.1 V < V_s < 0.95 eV. A step-like increase, Δz ~ 8 nm, is observed over a voltage range < 0.2 V, with a measured threshold of E_{p+} = –0.95 ± 0.03 eV. Following this sharp displacement, the probe height continues to increase as a function of increasingly negative bias voltage with increased fluctuations in height relative to the sub-threshold data.[10] For the positive bias sweep, a slight increase in z at low bias is also observed, with a sharp displacement threshold at E_{p-} = 1.3 ± 0.03 eV. The probe height does not saturate within the measured voltage range for either bias polarity sweep, in agreement with observations by Kemerink and co-workers for STM-based *z-V* measurements on thin films of

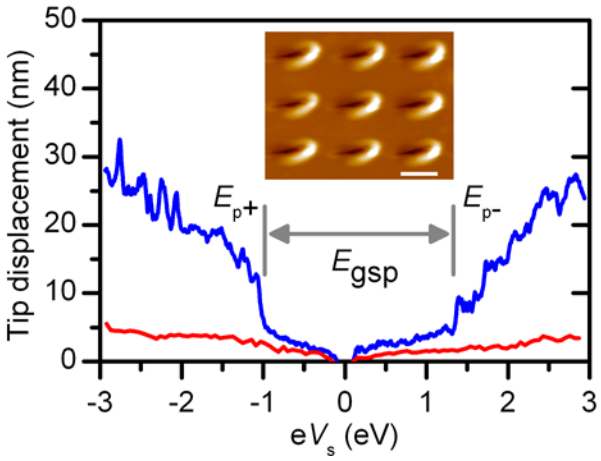

Figure 2.4. Negative- and positive-bias *z*-*V* data (blue) obtained at the same location on a 60 nm thick MEH-PPV film spun cast on a Au substrate. Clear voltage thresholds are observed at both polarities of the substrate bias voltage (V_s), corresponding to the threshold energies for charge-carrier injection into hole (E_{p+}) and electron (E_{p-}) polaron states. The single particle energy gap, $E_{gsp} = E_{p-} - E_{p+}$, is also indicated. No thresholds are observed in *z*-*V* curves acquired on bare Au substrates (red). The inset shows the topography of the MEH-PPV film measured by tapping mode AFM following acquisition of *z*-*V* data at a regular grid of locations, false colour height scale (*z*): 250 nm. Scale bar: 500 nm.

PPV derivatives (~ 100 nm thick) prepared by spin casting.[19] For the *z*-*V* data shown in Figure 2.4, the corresponding single particle energy gap, $E_{gsp} = E_{p-} - E_{p+} = 2.25 \pm 0.06$ eV. Taking $E_a = 2.08 \pm 0.06$ eV from the data shown in Figure 2.2(a) yielded an exciton binding energy $E_b = E_{gsp} - E_a \approx 0.17 \pm 0.12$ eV for this location on the film.

By contrast, *z*-*V* measurements acquired on bare flame-annealed Au substrates show smoothly varying curves with no evidence for voltage thresholds at either bias polarity; see Figure 2.4. The inset to Figure 2.4 shows a tapping mode AFM topography image of a region of the MEH-PPV film acquired following *z*-*V* spectroscopy measurements. A regular array of pits in the film is observed, corresponding to the orthogonal grid of *z*-*V* measurement locations, with a grid pitch ~ 500 nm. The topography data indicate that the material displaced by the AFM probe as it penetrates the film during the *z*-*V* measurement does not completely reflow following retraction of the probe. The lip observed at the right of each pit is due to the tilt angle between the plane of the AFM cantilever and the substrate (~ 15 º), which likely causes "raking" of the polymer as the probe apex penetrates and leaves the film during each *z*-*V* measurement. Analysis of the pits indicates the presence of a narrow furrow at the bottom of each pit, ~ 50 nm long by 30 nm wide. While the overall dimensions of the pits are governed by the probe dimensions, the cantilever tilt angle, and the film thickness, the probe apex clearly forms an electrical nanocontact to the polymer film; see Figure 2.5.

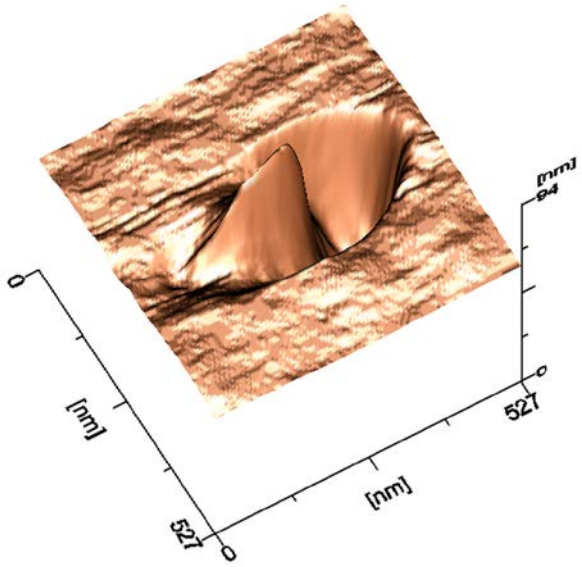

Figure 2.5. (a) Inverted tapping mode AFM image of the pit resulting from a *z*-*V* spectroscopy measurement on a 60 nm thick MEH-PPV film spun cast on a Au substrate. A narrow furrow at the bottom of the pit is clearly visible, indicating the formation of an electrical nanocontact to the polymer film by the probe apex. False colour height scale (*z*): 94 nm.

Distinct voltage thresholds were observed at both bias polarities in measured *z*-*V* data for more than 80 % of the locations sampled, confirming the efficacy of this method for local determination of the charge injection thresholds in macromolecular semiconductors. Figure 2.6 shows a map of the measured values for the single particle energy gap (E_{gsp}) across a 5 × 4 orthogonal grid of locations (~ 500 nm) on the same film for which data is presented in Figures 2.4 and 2.6. A range of values for E_{gsp} is observed, 1.55 eV < E_{gsp} < 2.7 eV. Figure 2.7 shows a histogram of the 43 E_{gsp} values extracted from *z*-*V* data measured for this film, with measured

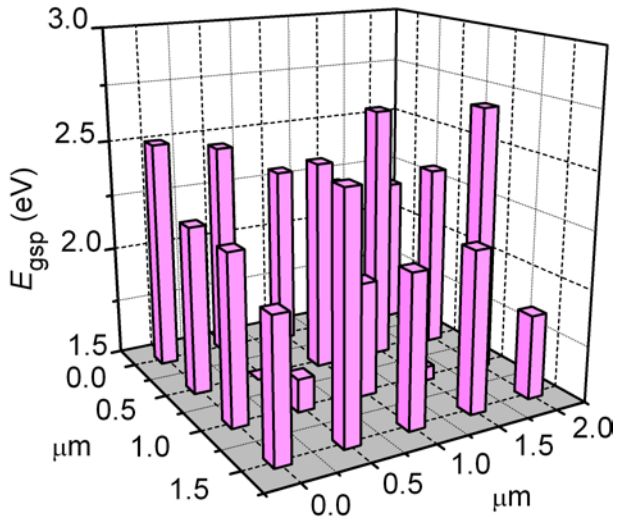

Figure 2.6. Spatial map of E_{gsp} values extracted from *z*-*V* data acquired at a regular grid of 20 locations on the MEH-PPV film for which data is shown in Figure 2.2 and 2.6.

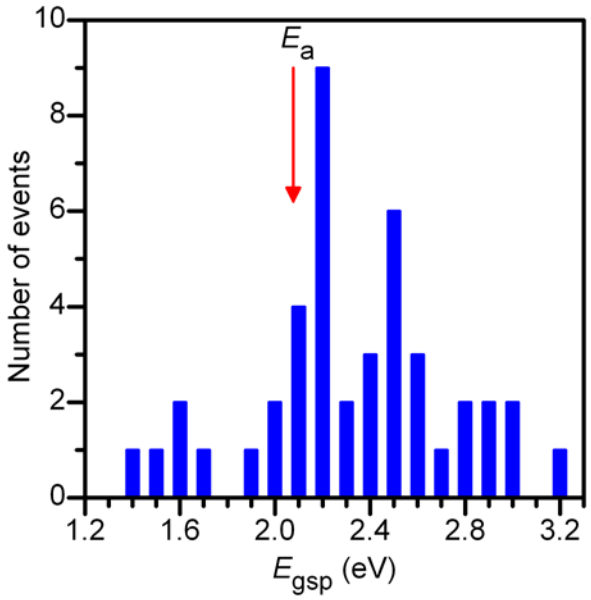

Figure 2.7. Histogram of the single particle gap energies, E_{gsp}, (0.1 V bins) calculated from *z*-*V* data acquired at a regular grid of 43 locations on the MEH-PPV film shown in Figure 2.4. The optical absorption edge (E_a) is indicated by the red arrow.

values in the range 1.4 eV < E_{gsp} < 3.2 eV. While the majority of measured E_{gsp} values lie above the optical absorption edge, E_a = 2.08 ± 0.06 eV, a small number of locations are also observed for which $E_{gsp} < E_a$. These arise from the presence of mid-gap states, likely due to exposure of the MEH-PPV film to the atmosphere during sample transfer from the nitrogen glovebox to the CP-AFM system prior to *z*-*V* measurement. In this regard, *z*-*V* data acquired

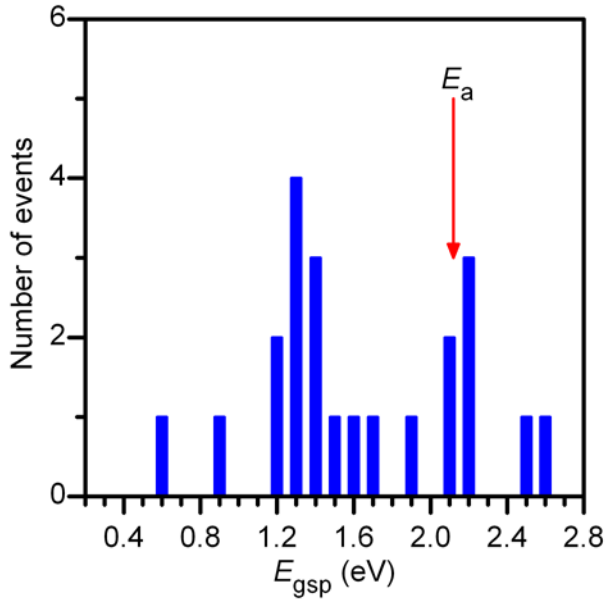

Figure 2.8. Histogram of the single particle band gap energies, E_{gsp}, (0.1 V bins) calculated from *z*-*V* data acquired at a regular grid of 22 locations on a MEH-PPV film prepared under ambient conditions. The optical absorption edge, E_a, is indicated by the red arrow.

for MEH-PPV films prepared under ambient conditions showed that states with $E_{gsp} < E_a$ accounted for ~ 70% of the total measured; see Figure 2.8. In Figure 2.7, three dominant peaks are observed above E_a in the E_{gsp} distribution. Gaussian fits to these data yield E_{gsp} peaks at 2.28 ± 0.07 eV, 2.50 ± 0.08 and a smaller peak at 2.90 ± 0.14 eV. By combining these data with E_a = 2.08 ± 0.06 eV, a series of exciton binding energies can be determined, with peak E_b values ≈ 0.2 eV, 0.4 eV and 0.8 eV, respectively.

Determination of the value(s) of the exciton binding energy in conjugated polymers and identification of the factors influencing these values are of key importance in order to develop an understanding of the mechanisms underlying charge injection, transport and recombination in these novel macromolecular semiconductors. For PPV and its derivatives, a wide range of measured values for the exciton binding energy (E_b) has been reported, 0.05 eV < E_b < 1.1 eV.[10,12-16] Several factors may influence the exciton binding energy, many of which are dependent on polymer synthesis and/or processing conditions. These include the average electron delocalization length (conjugation length) in the polymer; interchain coupling, which may screen the Coulomb interaction and hence reduce E_b; dimensionality effects, e.g., the presence of highly oriented 1-D polymer chains; random disorder; and, finally, interface effects between the polymer and the substrate, which may also result in increased screening.[12-16,20-25] Based on electronic structure calculations, several groups have proposed a dependence of the exciton binding energy in conjugated polymers on both inter-chain screening and chain conjugation length.[22-25] Concerning screening, large values of E_b were found for isolated chains, while inclusion of interchain interactions or increased chain packing density, which are responsible for long range screening in bulk polymers, yielded a dramatic reduction in the calculated value of E_b.[22,23] A quasi-exponential decrease in E_b with increasing conjugation length has also been proposed.[24,25]

Given that such fundamental aspects of the electronic properties of polymers are so strongly influenced by local morphology, it follows that the spatial variations in the E_{gsp} and, consequently, the E_b values observed for the MEH-PPV thin film described above reflect the nature of the nano-environment experienced by the polymer material addressed at each location. Importantly, the local variation in these values contrasts with the measured topographic smoothness of the film supporting the assertion that such variation is due to differences in the environment of the polymer material within the thin film or at the interface between the film and the underlying Au substrate. However, the observation of a distribution of E_{gsp} values does not necessarily imply the existence of different specific types of excitons because the excitonic band gap corresponding to the E_{gsp} value measured at each location is not known. In general, local variations of the measured electronic properties of spun-cast films of

conjugated polymers have previously been observed by a number of groups using scanning probes methods such as near-field scanning optical microscopy.[26-28] For example, micron-scale aggregates with distinct photoluminescence signatures have been observed in films of MEH-PPV spun cast from different solvents.[27] Also, variations in measured fluorescence intensity with polarization have been reported for annealed films of polyfluorene derviatives, corresponding to formation of organised domains with lateral dimensions ~ 100 nm, where the polarization anisotropy reflected differences in molecular orientation within each domain.[28] Finally, variations of E_{gsp} with location have recently been reported for thin films of methyl-substituted ladder-type poly(para-phenylene) using STM-based *z*-*V* spectroscopy.[18] Interestingly, a distribution of E_{gsp} values was also observed in that study, with a low energy peak (i.e., close to E_a) attributed to aggregate formation and two higher energy peaks attributed to local variations in the orientation of the polymer backbones at the buried interface between the polymer film and the metal substrate.

2.5 Conclusion

In this chapter, an initial demonstration of the application of CP-AFM-based *z*-*V* spectroscopy to local measurement of the electronic properties of conjugated polymer thin films has been reported. Using this approach, the charge injection thresholds along with corresponding single particle gap energies (E_{gsp}) and exciton binding energies (E_b) were determined for a MEH-PPV thin film. By performing measurements across a grid of locations on the film, a series of exciton binding energy distributions were identified, with peak E_b values $\approx$ 0.2 eV, 0.4 eV and 0.8 eV, respectively. The variation in measured E_b values was in contrast to the smoothness of the film surface suggesting that the variation may be attributable to differences in the nano-environment of the polymer material within the thin film at each measurement location. The influence of film preparation conditions was also investigated and found to be of critical importance to the development of conjugated polymer based devices. The method therefore represents a useful tool for local determination of electronic properties of organic materials.

2.6 References

1. Forrest, S. R. "The Path to Ubiquitous and Low-Cost Organic Electronic Appliances on Plastic", *Nature* **2004**, *428*, 911-918.

2. Malliaras, G.; Friend, R. H. "An Organic Electronics Primer", Phys. Today, **2005**, May, 53-58.

3. Shirota, Y. "Organic Materials for Electronic and Optoelectronic Devices", *J. Mater. Chem.* **2000**, *10*, 1-25.

4. Blythe, T.; Bloor, D. *Electrical Properties of Polymers*, Cambridge University Press: Cambridge, **2005**.

5. Shi, Y.; Liu, J.; Yang, Y. "Device Performance and Polymer Morphology in Polymer Light Emitting Diodes: The Control of Thin Film Morphology and Device Quantum Efficiency", *J. Appl. Phys.* **2000**, *87*, 4254-4263.

6. Liu, J.; Shi, Y.; Ma, L.; Yang, Y. "Device Performance and Polymer Morphology in Polymer Light Emitting Diodes: The Control of Device Electrical Properties and Metal/Polymer Contact", *J. Appl. Phys.* **2000**, *88*, 605-609.

7. Liu, J.; Guo, T.-F.; Shi, Y.; Yang, Y. "Solvation Induced Morphological Effects on the Polymer/Metal Contacts", *J. Appl. Phys.* **2001**, *89*, 3668-3673.

8. Pron, A.; Rannou, P. "Processible Conjugated Polymers: From Organic Semiconductors to Organic Metals and Superconductors", *Prog. Polym. Sci.* **2002**, *27*, 135-190.

9. Schwartz, B. J. "Conjugated Polymers as Molecular Materials: How Chain Conformation and Film Morphology Influence Energy Transfer and Interchain Interactions", *Annu. Rev. Phys. Chem.* **2003**, *54*, 141-172.

10. Alvarado, S. F.; Seidler, P. F.; Lidzey, D. G.; Bradley, D. D. C. "Direct Determination of the Exciton Binding Energy of Conjugated Polymers Using a Scanning Tunneling Microscope", *Phys. Rev. Lett.* **1998,** *81*, 1082-1085.

11. Conwell, E. M. "Definition of Exciton Binding Energy for Conducting Polymers", *Synth. Met.* **1996**, *83*, 101-102.

12. Leng, J. M.; Jeglinski, S.; Wei, X.; Benner, R. E.; Vardeny, Z. V.; Guo, F.; Mazumdar, S. "Optical Probes of Excited States in Poly(p-phenylenevinylene)", *Phys. Rev. Lett.* **1994**, *72*, 156-159.

13. Hagler, T. W.; Pakbaz, K.; Heeger, A. J. "Polarized Electroabsorption Spectroscopy of Highly Ordered Poly(2-methoxy,5-(2'-ethyl-hexoxy)-p-phenylene vinylene)", *Phys. Rev. B* **1995**, *51*, 14199-14206.

14. Campbell, I. H.; Hagler, T. W.; Smith, D. L.; Ferraris, J. P. "Direct Measurement of Conjugated Polymer Electronic Excitation Energies Using Metal/Polymer/Metal Structures", *Phys. Rev. Lett.* **1996**, *76*, 1900-1903.

15. Barth, S.; Bassler, H. "Intrinsic Photoconduction in PPV-Type Conjugated Polymers", *Phys. Rev. Lett.* **1997**, *79*, 4445-4448.

16. Moses, D.; Wang, J.; Heeger, A. J.; Kirova, N.; Brazoviski, S. "Electric Field Induced Ionization of The Exciton on Poly(phenylene vinylene)", *Synth. Met.* **2001**, *119*, 503-506.

17. Rossi, L.; Alvarado, S. F.; Rieß, W.; Schrader, S.; Lidzey, D. G.; Bradley, D. D. C. "Influence of Alkoxy Substituents on the Exciton Binding Energy of Conjugated Polymers", *Synth. Met.* **2000,** *111*, 527-530.

18. Alvarado, S. F.; Barth, S.; Bussler, H.; Scherf, U.; van der Horst, J.-W.; Bobbert, P. A.; Michels, M. A. J. "Spatially Resolved STM Spectroscopy of Charge Injection at the Ladder-Type poly(paraphenylene)/Au(111) Interface", *Adv. Funct. Mater.* **2002**, *12*, 117-122.

19. Kemerink, M.; Offermans, P.; van Duren, J. K. L.; Koenraad, P. M.; Janssen, R. A. J.; Salemink, H. W. M.; Wolter, J. H. "Real-Space Measurement of the Potential Distribution Inside Electronic Semiconductors", *Phys. Rev. Lett.* **2002**, *88*, art. no. 096803.

20. Kemerink, M.; Alvarado, S. F.; Muller, P.; Koenraad, P. M.; Salemink, H. W. M.; Wolter, J. H.; Janssen, R. A. J. "Scanning Tunneling Spectroscopy on Organic Semiconductors: Experiment and Model", *Phys. Rev. B* **2004**, *70*, art. no. 045202.

21. Wiesendanger, R. *Scanning Probe Microscopy and Spectroscopy*, Cambridge University Press: Cambridge, **1994**.

22. van der Horst, J.-W.; Bobbert, P. A.; Michels, M. A. J.; Brocks, G.; Kelly, P. J. "Ab Inito Calculation of The Electronic and Optical Excitations in Polythiophene: Effects of Intra- and Interchain Screening.", *Phys. Rev. Lett.* **1999**, *83*, 4413-4416.

23. Ruini, A.; Cadlas, M. J.; Bussi, G.; Molinari, E. "Solid State Effects on Exciton States and Optical Properties of PPV", *Phys. Rev. Lett.* **2002**, *88*, art. no. 206403.

24. Pedersen, T. G.; Johansen, P. M.; Pedersen, H. C. "Particle-in-a-Box Model of One-Dimensional Excitons in Conjugated Polymers", *Phys. Rev.B* **2000**, *61*, 10504-10510.

25. Knupfer, M. “Exciton Binding Energies in Organic Semiconductors”, *Appl. Phys. A* **2003**, *77*, 623-626.

26. Blatchford, J. W.; Gustafson, T. L.; Epstein, A. J.; Vanden Bout, D. A.; Kerimo, J.; Higgins, D. A.; Barbara, P. F.; Fu, D. K.; Swager, T. M.; MacDiarmid, A. G. “Spatially and Temporally Resolved Emission from Aggregates in Conjugated Polymers”, *Phys. Rev. B* **1996**, *54*, R3683-R3686.

27. Nguyen, T.-Q.; Schwartz, B. J.; Schaller, R. D.; Johnson, J. C.; Lee, L. F.; Haber, L. H.; Saykally, R. J. “Near-Field Scanning Optical Microscopy (NSOM) Studies of the Relationship between Interchain Interactions, Morphology, Photodamage, and Energy Transport in Conjugated Polymer Films”, *J. Phys. Chem. B* **2001**, *105*, 5153-5160.

28. Teetsov, J.; Vanden Bout, D. A. “Near-Field Scanning Optical Microscopy Studies of Nanoscale Order in Thermally Annealed Films of Poly(9,9-diakylfluorene)”, *Langmuir* **2002**, *18*, 897-903.

29. O'Brien, G. A.; Quinn, A. J.; Biancardo, M.; Preece, J. A.; Bignozzi, C. A.; Redmond, G. “Making Electrical Nanocontacts to Nanocrystal Assemblies: Mapping of Room-Temperature Coulomb-Blockade Thresholds in Arrays of 28-kDa Gold Nanocrystals”, *Small*, **2006**, *2*, 261-266.

Chapter 3

Making Electrical Nanocontacts to Nanocrystal Assemblies: Mapping of Room Temperature Coulomb Blockade Thresholds in Arrays of 28kDa Nanocrystal Gold Molecules

3.1 Introduction

There is a growing research interest in metal and semiconductor nanocrystals, often termed "artificial atoms" due to their size-dependent optical and electronic properties, e.g., quantum confinement and single charge tunneling.[0-5] Developing a detailed understanding of the charge injection, retention and transport properties of individual nanocrystals and nanocrystal arrays is an essential prerequisite if these 0-dimensional (0-D) nanostructures are to fulfill their promise as functional elements in future electronic or photonic devices. For example, nanocrystals have been proposed as charge storage elements in floating gate flash memories,[6,7] and as quantum dots in photonic devices.[8-10] While conventional current-voltage measurements on nanocrystal arrays are valuable, providing insight into the mechanisms underlying charge transport and the dimensionality of the current-carrying network, typically they only probe the global properties of the entire array.[11-13] Little information is revealed about the local charging environment of the nanocrystals. In this regard, scanning probe methods, e.g., scanning tunneling spectroscopy (STS), electrostatic force microscopy (EFM) and conducting-probe atomic force microscopy (CP-AFM) have recently emerged as effective techniques for combined imaging and local electrical characterization with high spatial resolution.[14,15] These methods have been applied to investigate charging, discharging and transport mechanisms in individual metal and semiconductor nanocrystals at the single charge level,[16-22] and have also been employed to probe the collective electronic properties of nanocrystal arrays.[19,20,23-28]

Since the electronic properties of individual nanocrystals are critically dependent on the nanocrystal core diameter, chemically synthesised nanocrystals attract considerable research interest due to the recent emergence of efficient methods for synthesis of ligand-passivated metal and semiconductor nanocrystals with narrow core size distributions.[0-5] Of these, 28 kDa nanocrystal gold molecules, containing ~ 140 gold atoms, have received particular attention.[4,5] Extensive structural, optical and electrochemical characterization of these nanocrystal molecules has been undertaken by the Murray and Whetten groups.[4,5,18,19,29-35] Due to the small effective diameter of the nanocrystals cores (d ~ 1.65 nm) and the insulating nature of the protecting ligand monolayer, which acts as a tunnel barrier, single electron charging effects (Coulomb blockade) have been observed at room temperature in isolated nanocrystals using scanning tunneling spectroscopy,[19] and ensemble Coulomb staircases have also been observed at room temperature using electrochemical techniques.[18]

In this chapter,[*] local mapping of the electronic properties of arrays of 28 kDa gold nanocrystals via combined conducting-probe atomic force microscopy (CP-AFM) and displacement-voltage (*z*-*V*) spectroscopy is described. As mentioned in Chapter 2, Alvarado and co-workers have previously used an ultra-high vacuum scanning tunneling microscope (STM) to perform *z*-*V* spectroscopy on a conjugated polymer layer sandwiched between a metal tip and a planar gold substrate.[36-38] Applying a small bias voltage with the STM feedback loop engaged (to maintain a constant setpoint current) caused the tip to penetrate the polymer film and approach within tunneling distance of the substrate, since the polymer layer behaved as an insulator at low bias. As the bias voltage was increased, the relative tip height above the substrate remained effectively constant until a sharp vertical displacement was observed at a particular voltage (V_T) corresponding to the threshold energy for charge injection at that bias polarity. In this manner, the electron- and hole-polaron energies could be measured independently. One drawback in the experiment was that the use of an STM precluded stable imaging of the polymer topography.

This chapter reports on the first application of CP-AFM-enabled *z*-*V* spectroscopy under ambient conditions for mapping the topography and local electronic properties of arrays of 28 kDa Au nanocrystals. CP-AFM-based *z*-*V* spectroscopy is shown to permit local, room temperature measurements of the Coulomb blockade voltage thresholds arising from sequential single electron charging of 28 kDa Au nanocrystals in short current-carrying paths through the portion of a nanocrystal array located between the apex of a conducting AFM probe and an underlying Au substrate. It is also shown that the fluid properties of these nanocrystal arrays enable reproducible formation of nanoscale probe-array-substrate junctions, allowing the influence of background charge on the electronic properties of the array to be identified. Finally, it is demonstrated that the use of CP-AFM allows complementary topography and phase data to be acquired before and after spectroscopy measurements, enabling comparison of local array morphology with local electronic properties.

[*] This work is published as "Making Electrical Nanocontacts to Nanocrystal Assemblies: Mapping of Room-Temperature Coulomb-Blockade Thresholds in Arrays of 28 kDa Gold Nanocrystals", *Small* **2006**, *2*, 261-266.

3.2 Brief Description of the Proposed Approach

Figure 3.1 shows the proposed model for a local CP-AFM-based *z*-*V* measurement on an array of ligand-protected 28 kDa Au nanocrystals. Initially, topographic and phase images of the nanocrystal film are acquired in AFM tapping mode to identify smooth, homogeneous regions of the nanocrystal film. Following selection of an appropriate location, the probe is retracted and the microscope is switched into scanning tunneling microscopy mode for the *z*-*V* spectroscopy measurements. A small bias voltage is applied between the substrate and the metallised probe, and a current setpoint is fixed. The right-hand panel in Figure 3.1(a) shows the situation after the feedback loop has been engaged.

The probe has penetrated into the nanocrystal film until the measured current has reached the setpoint. At low bias, current flow through the nanocrystal array between the probe apex and the substrate is almost completely suppressed due to sequential Coulomb blockade. However, a small (but non-zero) current can flow through the nanocrystal array at low bias arising from the

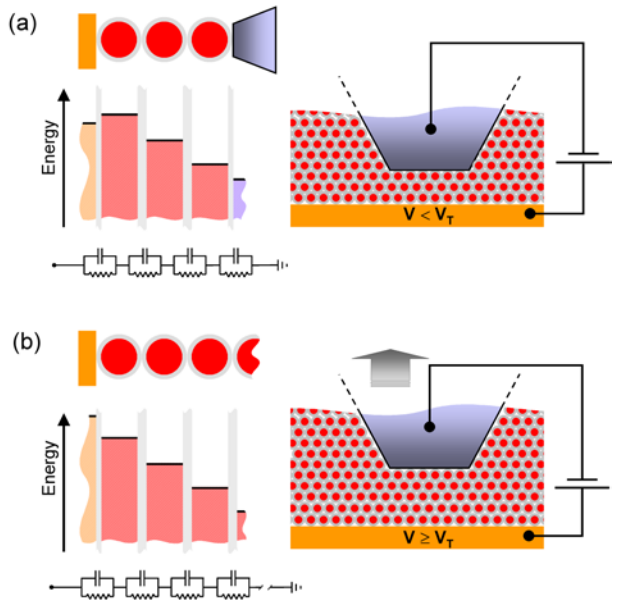

Figure 3.1. Schematic representation of a local *z*-*V* measurement on a small array of ligand-protected 28 kDa Au nanocrystals located between a metallised AFM probe and a planar gold substrate. (a) Left: 1-D representation of a single conducting path; a simplified energy diagram for this path at a substrate bias voltage (V) below the array Coulomb blockade voltage threshold ($V < V_T$). Coulomb blockade has been lifted across all but one of the nanocrystals; the equivalent circuit for this path. Right: Cross-sectional schematic of the probe-array-substrate electrical nanocontact. (b) Situation for $V \geq V_T$, where the lifting of the local Coulomb blockade across each of the nanocrystals in the path results in a sharp increase in conductance, causing the probe to retract in order to maintain the preset current.

non-zero ratio of the thermal energy ($k_B T_{300K}$ ~ 26 meV) to the nanocrystal charging energy (E_c), where k_B is Boltzmann's constant and T is the temperature. Thus, the probe does not penetrate the nanocrystal film completely, but leaves a layer that is several nanocrystals thick between the probe apex and the substrate. As the bias voltage (V) is increased, the probe height (z) remains effectively constant, since each conducting path between the probe apex and the substrate contains at least one nanocrystal under Coulomb blockade. The left-hand panel in Figure 3.1(a) shows a simplified energy diagram for a conducting path through the array between the probe apex and the substrate containing three nanocrystals. The Fermi levels for the individual nanocrystals are offset by the nanocrystal charging energy (E_c), the energy required to add or remove an electron from the nanocrystal core. In the diagram, the applied bias voltage is large enough to lift the Coulomb blockade across all but one of the nanocrystals, shown here as the nanocrystal closest to the substrate, i.e., the Fermi level of the substrate is below the Fermi level of the leftmost nanocrystal, and current flow is therefore minimal. The left-hand panel of Figure 3.1(a) also shows an equivalent circuit for this conducting path. The circuit contains four tunnel junctions, where each junction represented as a parallel resistor-capacitor (RC) element, arising from the resistance of the insulating ligand tunnel barriers (R_B) and the total capacitance at each site (C_Σ), due to the self-capacitance of the nanocrystal core and capacitive contributions from the local environment, e.g., neighbouring nanocrystals or contact electrodes.

Figure 3.1(b) shows the situation just after the applied voltage has been made large enough to lift the Coulomb blockade across every nanocrystal in the conducting path, i.e., $V \geq V_T$, where V_T is the threshold voltage for sequential Coulomb blockade. The energy diagram shows that the Fermi level of the substrate electrode is now higher than the Fermi levels of each of the nanocrystals in the chain, thus charge can tunnel efficiently to and from the nanocrystals in this path. Furthermore, additional parallel paths can now also open through the portion of array between the probe apex and the substrate. Consequently, the local conductance increases dramatically and the feedback loop causes the probe to retract in order to maintain the setpoint current. Therefore, a key advantage of z-V spectroscopy over conventional current-voltage spectroscopy for measurement of threshold voltages is that the feedback loop remains active during the bias voltage sweep, thus a small increase in the measured current can result in a large relative displacement, allowing precise determination of the Coulomb blockade threshold voltages at both bias polarities. On the basis of this model, z-V spectroscopy is expected to enable precise measurements of Coulomb blockade thresholds in arrays of 28 kDa Au nanocrystals.

3.3 Experimental

3.3.1 Synthesis of 28 kDa (*d* = 1.65 nm) Gold Nanocrystals[40†]

Reagents and solvents were purchased from Aldrich, and used without purification unless otherwise stated. All solvents were degassed with Ar prior to use and maintained under an Ar atmosphere. De-ionised water (Millipore; Q, > 18 MΩcm) was used for all aqueous solutions. Gold nanocrystals passivated with octanethiol were synthesised using a modified Brust-Schiffrin method.[4,5,39]

Briefly, an aqueous solution of $HAuCl_4$ (0.9 mM) was added to a solution of the phase-transfer catalyst, tetraoctylammoniumbromide (TOAB, 3.9 mM), in degassed anhydrous toluene, while stirring at room temperature. The organic phase turned red, while the aqueous phase remained colourless. The two-phase mixture was vigorously stirred at room temperature for 20 minutes. Following removal of the aqueous phase, octanethiol (2.7 mM) was added. The reaction was stirred for a further 20 minutes at room temperature. A freshly-made aqueous suspension of $NaBH_4$ (24 mM) was added to the solution under vigorous stirring at room temperature, which was continued overnight. The solution turned brown. The aqueous phase was separated, and the organic phase reduced in vacuum. The resulting nanocrystal solid was redissolved in toluene. Excess organic stabilisers were removed by repeated purification cycles entailing the addition of non-solvent (ethanol) to the nanocrystal solution, centrifugation of the precipitate, and redispersion of the resultant nanocrystal material in toluene. Finally, the solid crystal fractions were combined, dissolved in $CHCl_3$, solvent removed in vacuum and dried overnight under high vacuum.

The nanocrystals were characterised by measuring ^1H Nuclear Magnetic Resonance (NMR) spectra, recorded on a Bruker AC300 (300.13 MHz) spectrometer, and Matrix Assisted Laser Desorption/Ionisation Time of Flight Mass Spectrometry (MALDI-TOF/MS) spectra (1-100 kDa), acquired for neat (matrix-free) films of the nanocrystal solid using a Bruker Biflex IV spectrometer with a 337 nm nitrogen laser.

3.3.2 Synthesis of *d* = 6 nm Gold Nanocrystals[45]

Gold nanocrystals passivated with 11-mercaptoundecanoic acid (Au:MUA) were also synthesised using the Brust-Schiffrin method.[4,5,39] All solvents were degassed with Ar prior to use and maintained under an Ar atmosphere. De-ionised water (Millipore; Q, > 18 MΩ cm)

† Nanocrystal processing steps were under taken by Prof. Jon Preece's group within the School of Chemistry at the University of Birmingham.

was used for all aqueous solutions. An aqueous solution of $NaBH_4$ (5 mM) was added to a vigorously stirred toluene solution of $HAuCl_4$ (5 mM) in the presence of tetraoctylammonium bromide (TOAB, 1mM). A rapid colour change from orange to red-brown was observed. The solution was stirred for a further two hours. Following removal of the toluene in vacuo and resuspension of the nanocrystals in CH_2Cl_2, subsequent addition of MUA in CH_2Cl_2 resulted in immediate precipitation of the nanocrystals. The nanocrystal dispersion was purified by repeated cycles of resuspension in H_2O, precipitation with 50:50 CH_3OH:CH_2Cl_2, then centrifugation to collect the precipitant.

The nanocrystals were characterised by measuring ^1H Nuclear Magnetic Resonance (NMR) spectra, recorded on a Bruker AC300 (300.13 MHz) spectrometer, and Matrix Assisted Laser Desorption/Ionisation Time of Flight Mass Spectrometry (MALDI-TOF/MS) spectra (1-100 kDa), acquired for neat (matrix-free) films of the nanocrystal solid using a Bruker Biflex IV spectrometer with a 337 nm nitrogen laser.

Transmission electron microscopy (TEM) images of the gold nanocrystals were collected on a Philips CM20 transmission electron microscope operating at 200 kV. Samples were prepared by slow evaporation of one drop of a dilute solution of the nanocrystals on a carbon coated copper mesh grid.

3.3.3 Electrochemical Measurements of 28 kDa (*d* = 1.65 nm) Au Nanocrystals[§]

Electrochemical characterization of the 28 kDa nanocrystals was performed in a three electrode open cell containing a polycrystalline Au disk working electrode (2 mm diameter), an $Ag/AgNO_3$ reference electrode and a Pt wire counter electrode.[42] Briefly, the gold disk electrode was polished with 1, 0.3, 0.05 μm Al_2O_3 slurries and cleaned by potential cycling between 1.2 and –0.4 V versus SCE in 0.1 M H_2SO_4 for approximately 5 minutes. The working electrode was than immersed in a 0.1 M nonanedithiol/toluene solution overnight, followed by thorough rinsing with toluene and immersion in a solution of the 28 kDa nanocrystals in toluene for 24 hours. Subsequent layers were deposited by repeated alternate immersions in the nanocrystal and dithiol solutions respectively; see Figure 3.2(a). After the first monolayer of nanocrystals had been deposited on the functionalised electrode surface, immersion times at least of three hours in the nanocrystal and dithiol solutions were employed in order to obtain saturated layers. Cyclic voltammetry (CV) and differential pulse voltammetry (DPV) measurements were then performed in 0.1 M Bu_4NPF_6/CH_2Cl_2 electrolyte solution.

[§] Electrochemical measurements were undertaken by Dr. Matteo Biancardo within the Nanotechnology Group at the Tyndall National Institute.

In CV, the current in the cell is measured as a function of the potential. Electron transfer to and from the nanocrystal multilayer occurs at the Au working electrode while the counter electrode maintains the desired current from the signal source to the solution and the reference potential electrode is maintained at a constant potential value. The potential difference between the reference electrode and the working electrode is linearly cycled. In DPV, the potential wave form consists of small pulses (of constant amplitude) superimposed upon a staircase wave form. The current is sampled twice in each pulse period (once before the pulse, and at the end of the pulse), and the difference between these two current values is recorded and displayed. For a multilayer of 28 kDa Au nanocrystals tethered to a polished polycrystalline Au electrode a number of current peaks, which are regularly spaced, are observed. These electrochemical current peaks, termed quantised double layer peaks, appear because the effective capacitances of the dithiol passivated nanocrystals are so small (< 1 aF) that single electron changes in their core charges occur at large voltage intervals relative to $k_B T$ even at room temperature. Multiple peaks were observed in both the CV and DPV for 28 kDa Au nanocrystal multilayers tethered to polished polycrystalline Au electrodes; the DPV experiment is clearly the superior method for resolving small current features.

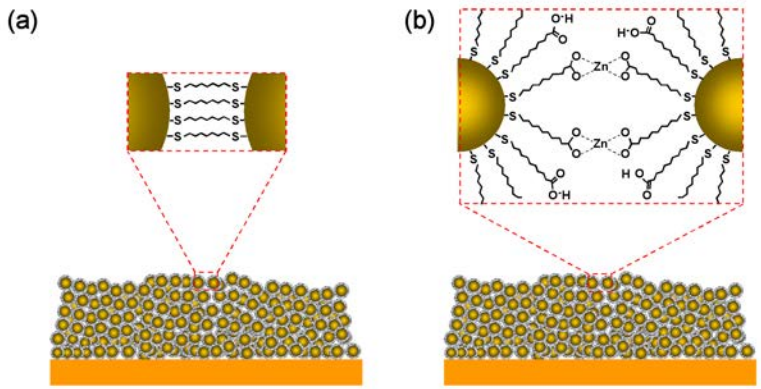

Figure 3.2. Schematic representation of (a) a 28 kDa Au nanocrystal multilayer tethered to a nonanedithiol functionalised Au electrode; the magnified view of the region highlighted in red reveals the nonanedithiol linkages between adjacent 28 kDa Au nanocrystals. (b) d = 6 nm Au:MUA nanocrystal multilayer tethered to a MUA-functionalised Au electrode; the magnified view of the region in red outlines the MUA-metal ion-MUA binding used to link adjacent d = 6 nm Au nanocrystals.

3.3.4 Electrochemical Measurements of d = 6 nm Au Nanocrystals

Electrochemical characterization of d = 6 nm Au:MUA nanocrystals was performed in a three-electrode single compartment cell as described above. Following cleaning of the polished polycrystalline Au disk working electrodes, the electrodes were immersed in a 5mM solution of MUA in ethanol for 48 hours. Au:MUA nanocrystals were tethered to the MUA-functionalised

working electrode by successive cycles of electrode immersion in solutions of 1 mM KOH (in ethanol) for 20 minutes, 0.2 M $Zn(NO_3)_2$ in ethanol for 20 minutes and finally in a nanocrystal solution (comprising 750 μL of 20 μM Au:MUA nanocrystals with 5μL 0.04 M KOH/EtOH added) for 30 minutes; see Figure 3.2(b). CV and DPV measurements were then performed in 0.1 M Bu_4NPF_6/CH_2Cl_2 electrolyte solution.

3.3.5 AFM Imaging and *z-V* Measurements of Nanocrystal Arrays

Gold substrates were prepared for *z-V* measurements by vacuum evaporation of metal (Cr 10 nm, Au 100 nm) onto silicon wafers, followed by solvent cleaning and flame-annealing. Nanocrystal arrays were prepared by drop deposition of a purified nanocrystal solution in toluene onto each substrate; the excess solvent was then allowed to evaporate over 1 hour. AFM topography measurements (JSPM 4200, JEOL U.K. Ltd.) were acquired in tapping mode under ambient conditions, using commercial PtIr metallised probes (NCH-Pt, Nanosensors, Germany) with apex diameters ~ 25 nm.

For each set of room temperature *z-V* spectroscopy measurements on freshly deposited nanocrystal arrays, simultaneous topography and phase images were first acquired to identify smooth, homogeneous regions (uniform phase) with low concentrations of aggregates suitable for spectroscopy measurements. Phase contrast images were acquired simultaneously with the topography data.

Following topography and phase measurements, a suitable region of each nanocrystal array was selected and *z-V* spectroscopy measurements were then performed at a regular orthogonal grid of locations within the region, at pitches of ~ 750 nm. At each location, an initial bias voltage of –0.1 V was applied to the substrate (with the probe acting as a virtual ground) and the feedback loop was engaged, causing the probe to approach the substrate until the measured current reached the setpoint (50 pA). The relative probe height (*z*) was then measured as a function of the applied bias (*V*: –0.1 V $\rightarrow$ –3 V). At the end of the negative sweep, the probe was withdrawn, the bias voltage setpoint was adjusted to +0.1 V, the feedback loop was re-engaged and the positive polarity sweep (*V*: +0.1 V $\rightarrow$ +3 V) was measured. On completion of *z-V* spectroscopy measurements, simultaneous topography and phase images of the region were again acquired.

3.4 Results and Discussion

3.4.1 Physical Characterisation of 28 kDa Nanocrystals

Figure 3.3 shows a mass spectrum of a typical sample of purified octanethiolate-protected nanocrystal gold molecules (matrix-free). The spectrum shows a single dominant main peak at 27.6 kDa (full-width-at-half-maximum: 2.7 kDa) with weaker peaks corresponding to other stable cluster configurations. A 27.6 kDa cluster peak was identified by Whetten and co-workers in mass spectra acquired from polydisperse clusters and was ascribed to a truncated octahedral Au_{140} core based on X-ray data and atomistic simulations.[30] Subsequent experiments and further atomistic simulations for monodisperse 28 kDa clusters were consistent with a quasi-crystalline truncated decahedral Au_{146} core of diameter 1.64 nm.[31] The effective core diameter (d) for the Au_{140} clusters can be estimated using the density of bulk fcc Au (59 atoms/nm^3), via the relation $N_{Au} = 140 = (59\ nm^{-3})(\pi/6)d^3$. Thus the 27.6 kDa peak corresponds to an effective core diameter d = 1.65 nm. The inset to Figure 3.3 shows a typical optical absorption spectrum for a purified solution of 28 kDa octanethiolate-protected nanocrystal gold molecules in toluene. The plasmon absorption centred near 500 nm is weak and broad, characteristic of nanocrystal gold molecules with diameters less than 2.5 nm and the onset of absorbance near 700 nm is assigned to the first interband transition from the top of the 5d^{10} band to the lowest unoccupied levels of the broad 6sp conduction band.[32] ^{1}H NMR data (not shown) acquired for the gold nanocrystals revealed a broadened methylene proton peak indicating formation of covalent thiol bonds between the gold cores and ligands. No evidence of free ligands was observed.

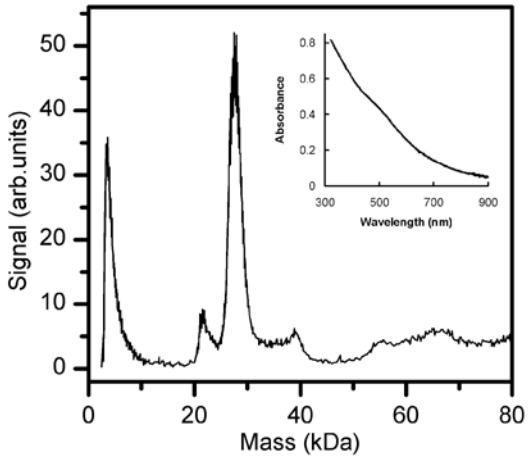

Figure 3.3. Mass spectrum of a matrix-free gold nanocrystal film. The main peak at 27.6 kDa corresponds to a mean nanocrystal core diameter d ~ 1.65 nm. Inset: Optical absorption spectrum of 28 kDa gold nanocrystals in toluene. The strongly diminished and broadened plasmon absorption centred at 500 nm is characteristic of nanocrystals with diameters below 2.5 nm.

The classical electrostatic energy required to add a single electron to a nanocrystal in an array is given by $E_c = e^2/2C_\Sigma$,[43] where e is the magnitude of the electronic charge and C_Σ is the total capacitance at each nanocrystal site. In contrast, for an isolated nanocrystal, this capacitance is the self-capacitance (C_0), which can be estimated from simple electrostatics by treating the nanocrystal as a conducting sphere of diameter d embedded in a dielectric of relative permittivity ε_r, thus $E_0 \approx e^2/4\pi\varepsilon_0\varepsilon_r d$, where ε_0 is the vacuum permittivity. Taking the effective core diameter d = 1.65 nm, and ε_r = 2.7 from literature data,[44] yields C_0 = 0.25 aF and a single nanocrystal charging energy $E_0 = e^2/2C_0 \approx$ 320 meV. For comparison, room temperature CV and DPV measurements of 28 kDa Au nanocrystal multilayers tethered to polished polycrystalline Au electrodes were performed in 0.1 M Bu_4NPF_6/CH_2Cl_2 electrolyte solution; see Figure 3.4.

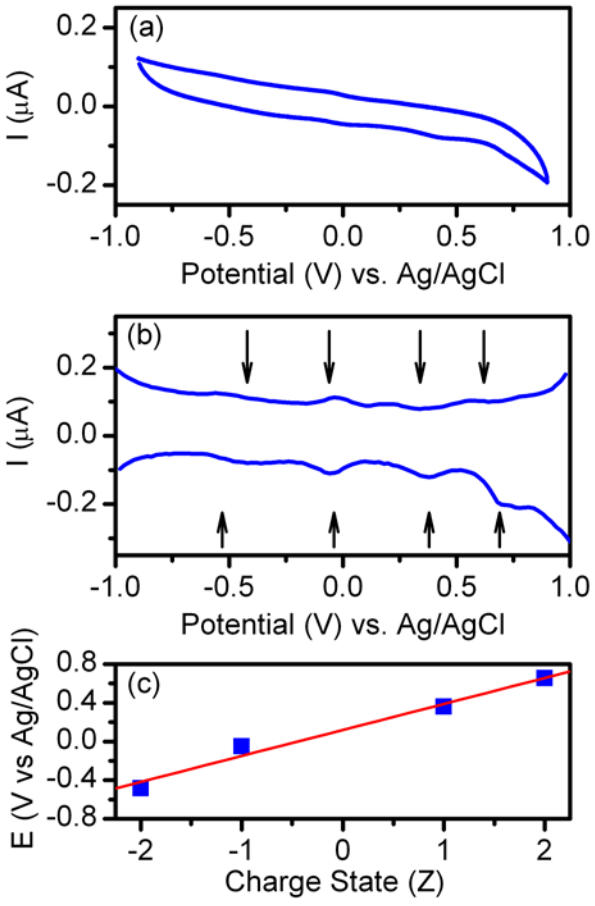

Figure 3.4. Typical (a) cyclic voltammetry (CV) and (b) differential pulse voltammetry (DPV) data acquired for a multilayer of 28 kDa Au nanocrystals tethered to a polished polycrystalline Au electrode in 0.1 M Bu_4NPF_6/CH_2Cl_2 electrolyte solution. The arrows in (b) indicate ensemble single electron charging events. CV sweep rate 20 mV/s. DPV measurement conditions: Amplitude 50 mV, pulse width 200 ms, sample width 20 ms, pulse period 200 ms. (c) Formal potentials (E_p) of charging events versus nanocrystal charge state (Z). A linear fit to the data yields a single electron charging energy E_c = 270 ± 30 meV for a 28 kDa Au nanocrystal in a multilayer array.

The regular peaks observed in the DPV of Figure 3.4(b) indicated quantised double-layer charging of the nanocrystal cores and provided further evidence of the low polydispersity of the 28 kDa nanocrystals.[35] Figure 3.4(c) shows a plot of the measured formal potentials (E_p) of charging events from Figure 3.4(b) versus nanocrystal charge state (Z). The data can be modeled using the expression $E_p = E_{PZC} + (Z - 1/2)E_c$,[35] where E_{PZC} is the potential at zero charge and E_c is the single electron charging energy for a 28 kDa nanocrystal in a multilayer array. E_c can be determined from a linear fit to the data. From fitting the formal potentials of charging events versus cluster charge state,[35] the single electron charging energy for a nanocrystal in an array was calculated to be $E_c = 270 \pm 30$ meV; see Figure 3.4(c). This value is in fair agreement with data from Murray's group obtained using a similar method for octanethiolate-passivated 28 kDa nanocrystals ($E_c = 310$ meV).[35] The lower value for the measured charging energy of a nanocrystal in an array ($E_c = 270$ meV) in our data versus the calculated value for an isolated nanocrystal ($E_0 \approx 320$ meV) is likely due to the fact that the total capacitance at each nanocrystal site in the array (C_Σ) exceeds the self-capacitance of an isolated nanocrystal (C_0) as a result of classical electrostatic coupling from neighbouring nanocrystals in the array.[43]

3.4.2 Physical Characterisation of d = 6 nm Nanocrystals

Following purification of newly synthesised nanocrystals, histogram analysis of TEM images containing several hundred nanocrystals was carried out. This process yielded a mean nanocrystal diameter $d = 6$ nm. ^{1}H NMR data acquired for the purified Au:MUA nanocrystals showed a broadened methylene proton peak indicating formation of covalent thiol bonds between the gold cores and MUA ligands. No evidence of free ligands was observed.

CV and DPV measurements of $d = 6$ nm Au:MUA nanocrystal multilayers tethered to polished polycrystalline Au electrodes were performed in 0.1 M Bu_4NPF_6/CH_2Cl_2 electrolyte solution; see Figure 3.5. No evidence for quantised double layer charging at room temperature was observed in the data measured for these $d = 6$ nm nanocrystal arrays indicating that the nanocrystal charging energy is not substantially larger than the thermal energy. This is in accord with previous variable-temperature charge transport characteristics acquired for multilayer arrays of these nanocrystals drop deposited between gold electrodes (inter-electrode gaps ~ 50 nm),[45] which yielded measured charging energies in the range 30 meV < E_c < 32 meV. Voltage thresholds corresponding to sequential Coulomb blockade were only observed for temperatures at or below 38 K.[45]

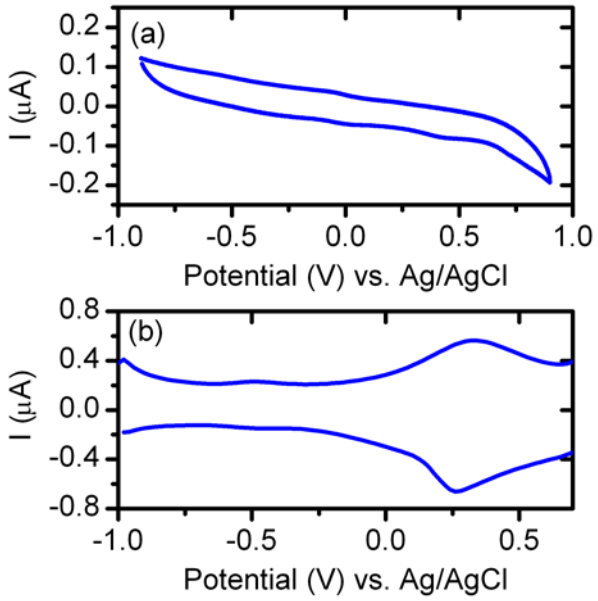

Figure 3.5. Typical (a) CV, and (b) DPV data acquired for a d = 6 nm Au nanocrystal multilayer tethered to a polished polycrystalline Au electrode in 0.1 M Bu_4NPF_6/CH_2Cl_2 electrolyte solution. CV sweep rate 25 mV/s. DPV measurement conditions: amplitude 50 mV, pulse width 200 ms, sample width 20 ms, pulse period 200 ms. No evidence for ensemble single electron charging was observed.

3.4.3 *z-V* Spectroscopy of Nanocrystal Films

Simultaneous topographic and phase images of freshly deposited nanocrystal films were acquired in AFM tapping mode to identify smooth, homogeneous regions (uniform phase) with low concentrations of aggregates suitable for *z-V* spectroscopy measurements; see Figure 3.6. This mode allows nanocrystal array topography to be imaged with minimal probe-sample interaction. Figure 3.6(a) shows the measured topography for one such region of a 28 kDa NC layer deposited from toluene solution after allowing the excess solvent to evaporate over 1 hour. The region appears smooth, with measured root-mean-square (RMS) roughness for the 3 × 3 μm^2 region from which this image was taken of 1.4 nm, comparable to values measured for bare gold substrates following flame-annealing (1-2 nm RMS). The region contains a low concentration of islands with diameters in the range 50-200 nm (< 1 μm^{-2}). Phase contrast images were acquired simultaneously with the topography data; see Figure 3.6(b). These measurements confirmed the homogeneity of the film.

AFM topography data acquired over larger scan areas (100 × 100 μm^2) on freshly deposited nanocrystal films demonstrated that it was not possible to produce trenches by scratching a film, suggesting that the nanocrystals reflowed following structural perturbation of the array. This

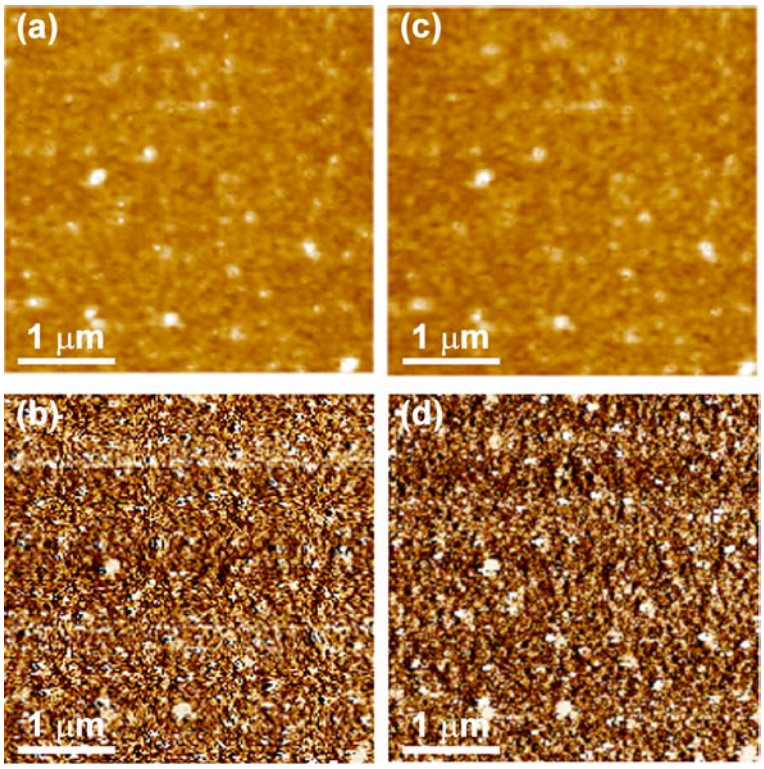

Figure 3.6. (a) Tapping mode AFM topography image of a layer of 28 kDa (d = 1.65 nm) Au nanocrystals drop-cast on a Au substrate measured before acquisition of a regular grid of tip displacement versus bias voltage (z-V) data (grid pitch ~ 750 nm). False colour height scale (z): 12 nm, RMS roughness: 1.4 nm. (b) Simultaneously acquired phase image. False colour phase scale: 68º. (c) Topography data for the same region as shown in (a) imaged following acquisition of z-V data at a regular grid of points. False colour height scale (z): 12 nm, RMS roughness: 1.5 nm. The slight offset between the pre- and post-measurement topography images is the result of thermal drift. (d) Simultaneously acquired phase image. False colour phase scale: 64º. Acquisition of z-V data does not appear to affect the nanocrystal layer topography.

behaviour is in agreement with simulations of the behaviour of monolayers of ligand-protected Au_{140} nanocrystals on graphite substrates[46] where the protecting monolayer was predicted to lubricate the nanocrystal-substrate interface, resulting in high surface mobility of the nanocrystals, which occurred through an activated collective slip-diffusion mechanism.

Following selection of the suitably smooth region of the 28 kDa nanocrystal layer shown in Figure 3.6(a), z-V data was then acquired using the approach described in section 3.3.5. A typical pair of negative and positive z-V curves measured at the same location on the nanocrystal array are shown in Figure 3.7. For the negative sweep, a sharp threshold is observed at $V_{T-} \approx -0.6$ V, resulting in a large probe displacement at increasingly negative bias polarity. For the positive sweep, a sharp threshold is also observed, this time at $V_{T+} \approx +0.8$ V,

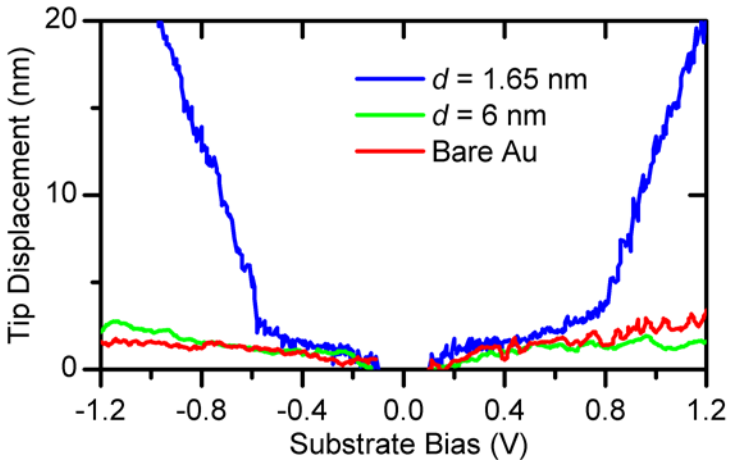

Figure 3.7. Negative and positive bias *z*-*V* curves acquired at the same location on a layer of 28 kDa (*d* = 1.65 nm) Au nanocrystals drop-cast on a Au substrate (Figure 3.6(a)) showing clear voltage thresholds. No thresholds are observed in *z*-*V* data acquired on bare Au substrates or in data measured for drop cast layers of larger *d* = 6 nm Au nanocrystals.

indicating an asymmetry in the displacement threshold voltages. In contrast to the distinct thresholds observed in data measured for arrays of 28 kDa nanocrystals, data acquired on bare gold substrates and arrays of larger *d* = 6 nm nanocrystals show only smoothly varying *z*-*V* curves with no evidence for a voltage threshold at either bias polarity; see Figure 3.7. Thus, the *z*-*V* thresholds measured for the 28 kDa nanocrystals do indeed appear to represent lifting of sequential Coulomb blockade for short conducting paths containing multiple nanocrystals through the portion of the nanocrystal array between the apex of the conducting probe and the underlying substrate. The lateral dimensions of this portion of the array can be estimated as follows: Taking the distance between neighbouring nanocrystals as $D \approx d + 2s$, where $d = 1.65$ nm is the nanocrystal core diameter,[29,31] and s is the extended chain length of the octanethiol ligands ($s \approx 1$ nm),[35] results in $D \approx 2.85$ nm, corresponding to an array with lateral dimensions of $\sim 9 \times 9$ nanocrystals located beneath a probe whose apex area is $\sim 25 \times 25$ nm^2. The conducting AFM probe thus acts as an electrical nanocontact to the nanocrystal array.

Figure 3.6(c) and Figure 3.6(d) show the topography and phase data for the same region shown in Figure 3.6(a) following acquisition of an 8×5 array of *z*-*V* measurements at a pitch of 750 nm. The slight displacement between the images is due to thermal drift. No significant changes in the topography or phase images are evident and the measured root-mean-square roughness value (1.5 nm) is similar to the value measured for data acquired before the spectroscopy measurements (1.4 nm). The similarity in the measured topography data provides evidence for the assertion that the nanocrystals reflow in a fluid-like manner as the probe retracts during *z*-*V* measurements at each location.[46]

The sharp thresholds observed at both bias polarities for the 28 kDa nanocrystal array *z*-*V* measurement data shown in Figure 3.7 are well described by the model presented in Figure 3.1. Considering the positive sweep, at bias voltages below the measured voltage threshold ($V < V_{T+}$), each conducting path through the nanocrystal array contains at least one junction under Coulomb blockade so the probe displacement is minimal and similar to the observed behaviour for measurements on bare gold substrates; see Figure 3.7. When the substrate bias is sufficiently large ($V = V_{T+}$), the Coulomb blockade is lifted, the conductance increases sharply and the probe retracts to maintain the constant preset current. Above the threshold ($V \geq V_{T+}$), many additional conduction paths can open and the probe retracts further in order to maintain the setpoint current. A similar situation holds for the negative sweep, where the probe displacement is minimal for $|V| < |V_{T-}|$ and the Coulomb blockade is lifted at $V = V_{T-}$. For each pair of *z*-*V* measurements at a given location, the difference in energy between the positive and negative Coulomb blockade threshold voltages is defined to be $E_{diff} = e(V_{T+} - V_{T-}) = 1.4$ eV for the data shown in Figure 3.7. For sequential Coulomb blockade, $E_{diff} = 2N E_c$, where N is the integer number of nanocrystals in the shortest conducting path(s) through the portion of the array between the probe apex and the substrate and E_c is the single electron charging energy for a 28 kDa nanocrystal in an array ($E_c \sim 270$ meV; see Figure 3.4). The measured value of E_{diff} for the data shown in Figure 3.7 therefore suggests $N \approx 3$ nanocrystals in the shortest path(s) through the portion of the nanocrystal array between the apex of the conducting probe and the substrate.

Considering the asymmetry between the measured Coulomb blockade threshold voltages, the energy asymmetry E_{asym}, which is defined as $e(V_{T+} + V_{T-})$, is 0.2 eV for the data shown in Figure 3.7. Within the framework of orthodox single electron tunneling theory for double barrier tunnel junction devices (single nanocrystal devices), asymmetry in current-voltage characteristics is represented as an excess charge on the central node $Q = ne - Q_0$, where n is an integer and $|Q_0| \leq e/2$.[47,48] This fractional excess charge (Q_0) can arise from contact potential differences between probe and substrate, geometric capacitance differences, or local charge disorder.[47,49] Such asymmetry is characteristic of conducting paths containing only a few tunnel junctions.[48-50] For example, no asymmetry has been observed in Coulomb blockade threshold voltages measured at low temperature for laterally-contacted arrays of ligand-protected metal nanocrystals, where the shortest conducting paths contained 10-100 nanocrystals, whereas values of Q_0 obtained from *I*-*V* measurements on individual Au clusters have been in the range -0.20 ± 0.17 eV.[11-13,17] Thus, both the magnitude of the difference energy (E_{diff}) and the small (but non-zero) value of the energy asymmetry (E_{asym}) confirm charge transport through conducting paths containing only a few nanocrystals.

3.4.4 Mapping of Coulomb Blockade Thresholds to Local Array Morphology

To gain further insight into the Coulomb blockade process, *z*-*V* spectroscopy measurements were acquired at regular grids of locations on previously imaged smooth regions of a freshly deposited 28 kDa nanocrystal film on Au. At each grid point, negative and positive *z*-*V* sweeps were acquired as described above, allowing the (local) negative and positive Coulomb blockade thresholds to be accurately measured. Figure 3.8 shows the measured Coulomb blockade thresholds for a 5 × 2 grid (with a pitch of ~ 750 nm) together with the measured topography for the region from which the data were acquired. The data demonstrate that Coulomb blockade thresholds can be spatially mapped across the nanocrystal array, providing quantitative local measurements of the array electronic properties. Further, the spread in measured values for the thresholds appears to be narrow, suggesting reproducible probe-array-substrate nanocontact formation, consistent with the smooth film topography (uniform phase) and fluid-like properties of the nanocrystal array.

Figure 3.9(a) shows a histogram of the measured Coulomb blockade thresholds for a grid containing 27 locations (with grid spacing ~ 750 nm) acquired from the region shown in Figure 3.8 and neighbouring regions. Narrow distributions are observed at both bias polarities, with a clear gap in the low bias region. Gaussian fits to the distributions at negative and positive polarities yield values for mean thresholds of V_{T+}= 0.75 ± 0.1 V and V_{T-} = –0.55 ± 0.1 V. Figure 3.9(b) shows a histogram of the corresponding E_{diff} values for the Coulomb blockade threshold data presented in Figure 3.9(a). The narrow range of measured E_{diff} values (0.8 eV <

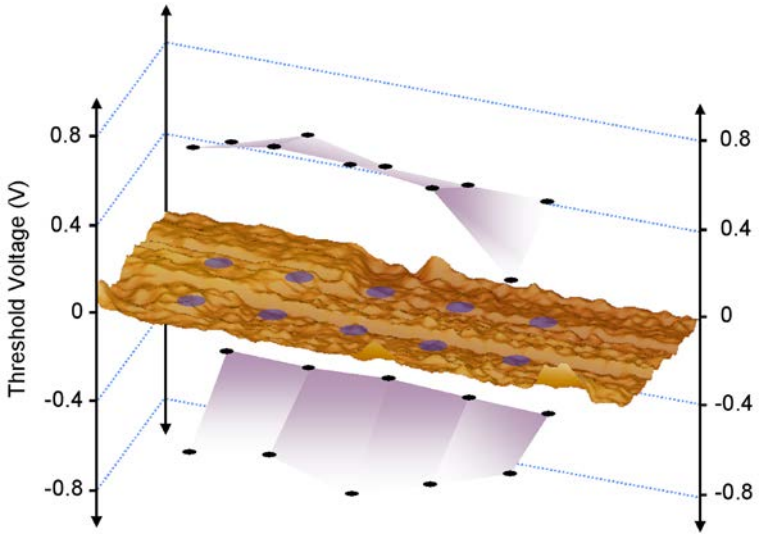

Figure 3.8. Mapping of measured *z*-*V* negative and positive Coulomb blockade thresholds for a 5 x 2 grid of measurement locations across a layer of 28 kDa Au nanocrystals drop-cast on a Au substrate. The ovals indicate the *z*-*V* measurement locations on the 3D rendering of the measured film topography (*z*-scale: 15 nm).

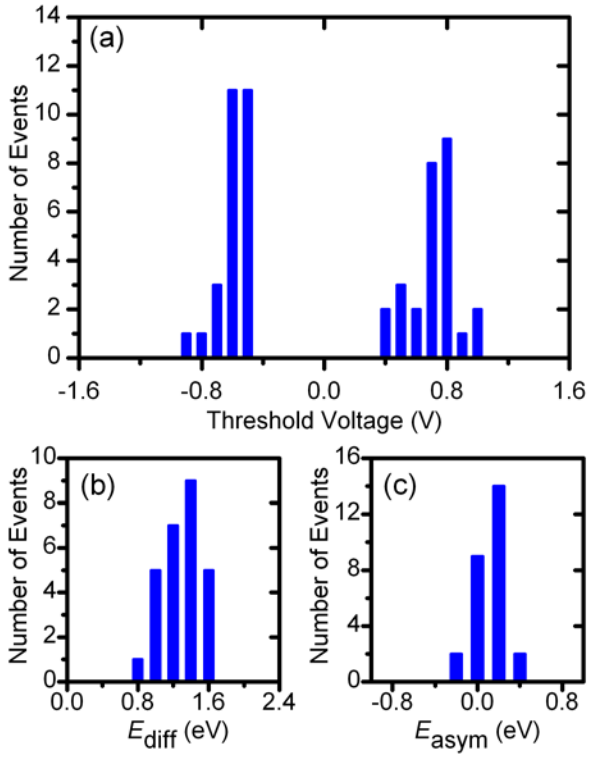

Figure 3.9. (a) Histogram of measured Coulomb blockade threshold voltages (0.1 V bins) from *z*-*V* data acquired at a regular grid of 27 locations on a 28 kDa nanocrystal film. Corresponding difference energy, (b), and energy asymmetry, (c), distributions (0.2 V bins) for the data shown in (a).

E_{diff} < 1.6 eV) indicates formation of probe-array-substrate nanocontacts where the shortest conducting path contains between 2 and 3 nanocrystals. Figure 3.9(c) shows a histogram of the corresponding E_{asym} values for the Coulomb blockade threshold voltage data presented in Figure 3.9(a). As discussed in the previous section, the small (non-zero; < 0.5 eV) values for the energy asymmetry indicate a weak influence of the fractional residual charge Q_0, characteristic of a network of tunnel junctions where the shortest conducting path contains only a few nanocrystals and the influence of background charges, e.g., arising from contact potential differences or other interface effects, is minimal.[49,50]

By comparison, CP-AFM and *z*-*V* measurements on regions where nanocrystal aggregates formed revealed non-uniform topography and high phase contrast as shown in Figure 3.10(a) and 3.10(b). As a consequence, extremely broad distributions in measured threshold voltages are observed at both bias polarities; see Figure 3.11. By comparison, Abeles and co-workers have previously fabricated random granular metal films by co-sputtering gold and aluminium oxide onto gold substrates to create ~ 25 nm thick layers with gold volume fractions below 0.45. As a result, there were no more than 2-3 isolated Au particles stacked vertically within a film and, for scanning tunneling spectroscopy measurements made at different locations on the top surface of a film, a dominant tunneling path (modelled as a triple-barrier tunnel-junction) was

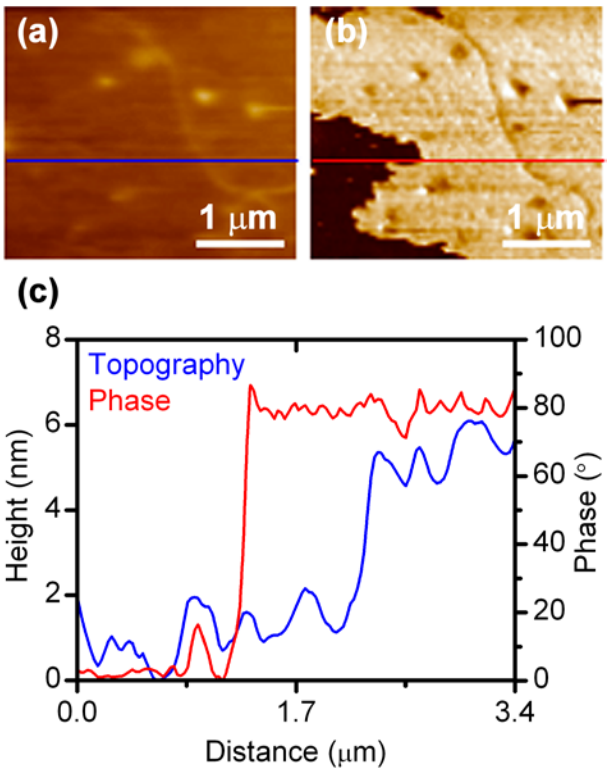

Figure 3.10. (a) Tapping mode AFM topography of a layer of 28 kDa (d = 1.65 nm) Au nanocrystals drop-cast on a Au substrate before acquisition of probe displacement versus bias voltage (z-V) data. False colour height scale (z): 16 nm, RMS roughness: 7.34 nm. (b) Phase imaging of the same region reveals a large and abrupt change in phase in the film, as observed in the line profiles in (c), suggesting a region of nanocrystal aggregation.

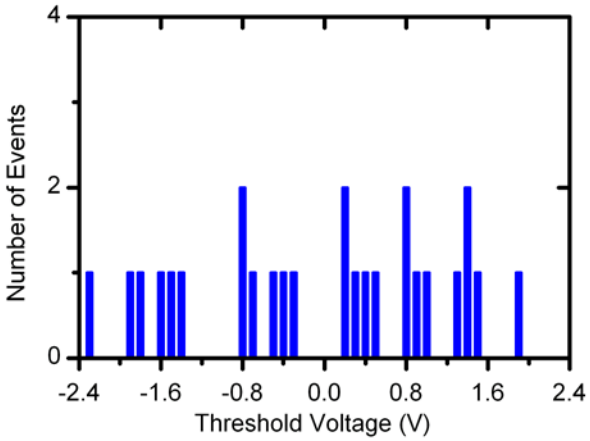

Figure 3.11. (a) Histogram of measured Coulomb blockade threshold voltages (0.1 V bins) from z-V data acquired at a regular grid of 14 locations on the region of high phase contrast of the 28 kDa nanocrystal film shown in Figure 3.10.

expected for each measurement location. Interestingly, these measurements also revealed broad distributions in the local electrical transport properties with variations in both measured energy gaps and asymmetries over lateral distances as small as 5 nm.[50]

3.5 Conclusion

In summary, it has been shown that CP-AFM-based *z*-*V* spectroscopy permits local, room temperature measurements of the Coulomb blockade voltage thresholds arising from sequential single electron charging of 28 kDa Au nanocrystals in current-carrying paths containing as few as 3 nanocrystals through portions of a nanocrystal array, with lateral dimensions ~ 9 × 9 nanocrystals, located between the apex of a conducting AFM probe and an underlying Au substrate. A key advantage of *z*-*V* spectroscopy over conventional current-voltage spectroscopy for measurement of threshold voltages is that the feedback loop remains active during the bias voltage sweep, thus a small increase in the measured current can result in a large relative displacement, allowing precise determination of the Coulomb blockade threshold voltages at both bias polarities. It has also been demonstrated that the fluid-like properties of these nanocrystal arrays enable reproducible formation of nanoscale probe-array-substrate junctions, allowing the influence of background charge on the electronic properties of the array to be identified. Finally, it has been shown that the use of CP-AFM allows complementary topography and phase data to be acquired before and after spectroscopy measurements, enabling comparison of local array morphology with local measurements of the Coulomb blockade thresholds. The use of CP-AFM based *z*-*V* spectroscopy could be an extremely valuable technique for characterization and analysis of charge transport through nanocrystal arrays, where specific information regarding the spatial variation of transport thresholds or, e.g., concerning the conductance of ligand molecules, is critically required. [51-55]

3.6 References

1. Alivisatos, A. P. “Semiconductor Clusters, Nanocrystals, and Quantum Dots”, *Science* **1996**, *271*, 933-937.

2. Collier, C. P.; Vossmeyer, T.; Heath, J. R. “Nanocrystal Superlattices”, *Annu. Rev. Phys. Chem.* **1998,** *49*, 371-404.

3. Murray, C. B.; Kagan, C. R.; Bawendi, M. G. “Synthesis and Characterization of Monodisperse Nanocrystals and Close-Packed Nanocrystal Assemblies”, *Annu. Rev. Mater. Sci.* **2000,** *30*, 545-610.

4. Whetten, R. L.; Shafigullin, M. N.; Khoury, J. T.; Schaaf, T. G.; Vezmar, I.; Alvarez, M. M.; Wilkinson, A. “Crystal Structures of Molecular Gold Nanocrystal Arrays”, *Acc. Chem. Res.* **1999**, *32*, 397-406.

5. Templeton, A. C.; Wuelfing, W. P.; Murray, R. W. “Monolayer-Protected Cluster Molecules”, *Acc. Chem. Res.* **2000**, *33*, 27-36.

6. Tiwari, S.; Rana, F.; Hussein, H.; Hartstein, A.; Crabbé, E. F.; Chan, K. “A Silicon Nanocrystals Based Memory”, *Appl. Phys. Lett.* **1996**, *68*, 1377-1379.

7. Liu, Z., Narayanan, V., Pei, G., Kan, E. C. “Metal Nanocrystal Memories. I. Device Design and Fabrication”, *IEEE Trans. Electron Dev.* **2002**, *49*, 1606-1613.

8. Colvin, V. L.; Schlamp, M. C.; Alivisatos, A. P. “Light-Emitting Diodes Made from Cadmium Selenide Nanocrystals and a Semiconducting Polymer”, *Nature* **1994**, *370*, 354-357.

9. Klimov, V. I.; Mikhailovsky, A. A.; Xu, S.; Malko, A.; Hollingsworth, J. A.; Leatherdale, C. A.; Eisler, H. J.; Bawendi, M. G. “Optical Gain and Stimulated Emission in Nanocrystal Quantum Dots”, *Science* **2000**, *290*, 314-317.

10. Tessler, N.; Medvedev, V.; Kazes, M.; Kan, S. H.; Banin, U. “Efficient Near-Infrared Polymer Nanocrystal Light-Emitting Diodes”, *Science* **2002**, *295*, 1506-1508.

11. Black, C. T.; Murray, C. B.; Sandstrom, R. L., Sun, S. “Spin-Dependent Tunneling in Self-Assembled Cobalt-Nanocrystal Superlattices”, *Science* **2000**, *290*, 1131-1134.

12. Parthasarathy, R.; Lin, X.-M.; Jaeger, H. M. “Electronic Transport in Metal Nanocrystal Arrays: The Effect of Structural Disorder on Scaling Behaviour”, *Phys. Rev. Lett.* **2001**, *87*, art. no. 186807.

13. Beecher, P.; Quinn, A. J.; Shevchenko, E. V.; Weller, H., Redmond, G. “Insulator-to-Metal Transition in Nanocrystal Assemblies Driven by In Situ Mild Thermal Annealing”, *Nano Lett.* **2004**, *4*, 1289-1293.

14. Wiesendanger, R. *Scanning Probe Microscopy and Spectroscopy*, Cambridge University Press: Cambridge, **1994**.

15. Kelley, T. W.; Granstrom, E. L.; Frisbie, C. D. “Conducting Probe Atomic Force Microscopy: A Characterization Tool for Molecular Electronics”, *Adv. Mater*. **1999**, *11*, 261-264.

16. Schönenberger, C.; Van Houten, H.; Donkersloot, H. C. “Single-Electron Tunneling Observed at Room-Temperature by Scanning-Tunneling Microscopy”, *Europhys. Lett.* **1992**, *20*, 249-254.

17. Andres, R. P.; Bein, T.; Dorogi, M.; Feng, S.; Henderson, J. I.; Kubiak, C. P.; Mahoney, W.; Osifchin, R. G.; Reifenberger, R. “"Coulomb Staircase" at Room Temperature in a Self-Assembled Molecular Nanostructure”, *Science* **1996**, *272*, 1323-1325.

18. Ingram, R. S.; Hostetler, M. J.; Murray, R. W.; Schaaf, T. G.; Khoury, J. T.; Whetten, R. L.; Bignioni, T. P.; Guthrie, D. K.; First, P. N. “28 kDa Alkanethiolate-Protected Au Clusters Give Analogous Solution Electrochemistry and STM Coulomb Staircases”, *J. Am. Chem. Soc.* **1997**, *119*, 9279-9280.

19. Bigioni, T. P.; Harrell, L. E.; Cullen, W. G.; Guthrie, D. K.; Whetten, R. L.; First, P. N. “Imaging and Tunneling Spectroscopy of Gold Nanocrystals and Nanocrystal Arrays”, *Eur. Phys. J. D* **1999**, *6*, 355-364.

20. Kim, S.-H.; Medeiros-Ribeiro, G.; Ohlberg, D. A. A.; Williams, R. S.; Heath, J. R. “Individual and Collective Electronic Properties of Ag Nanocrystals”, *J. Phys. Chem. B* **1999**, *103*, 10341-10347.

21. Boer, E. A.; Bell, L. D.; Brongersma, M. L.; Atwater, H. A.; Ostraat, M. L.; Flagan, R. C. “Charging of Single Si Nanocrystals by Atomic Force Microscopy”, *Appl. Phys. Lett.* **2001**, *78*, 3133-3135.

22. Boer, E. A.; Brongersma, M. L.; Atwater, H. A.; Ostraat, M. L.; Flagan, R. C.; Bell, L. D. “Localized Charge Injection in SiO_2 films Containing Silicon Nanocrystals”, *Appl. Phys. Lett.* **2001**, *79*, 791-793.

23. Medeiros-Ribeiro, G.; Ohlberg, D. A. A.; Williams, R. S.; Heath, J. R. "Rehybridization of Electronic Structure in Compressed Two-Dimensional Quantum Dot Superlattices", *Phys. Rev. B* **1999**, *59*, 1633-1636.

24. Taleb, A.; Silly, F.; Gusev, A. O.; Charra, F.; Pileni, M. P. "Electron Transport Properties of Nanocrystals: Isolated, and "Supra"-Crystalline Phases", *Adv. Mater.* **2000**, *12*, 633-637.

25. Sample, J. L.; Beverly, K. C.; Chaudhari, P. R.; Remacle, F.; Heath, J. R.; Levine, R. D. "Imaging Transport Disorder in Conducting Arrays of Metallic Quantum Dots: An Experimental and Computational Study", *Adv. Mater.* **2002**, *14*, 124-128.

26. Cherniavskaya, O.; Chen, L.; Weng, V.; Yuditsy, L.; Brus, L. E. "Quantitative Noncontact Electrostatic Force Imaging of Nanocrystal Polarizability", *J. Phys. Chem. B* **2003**, *107*, 1525-1531.

27. Drndić, M.; Markov, R.; Jarosz, M. V.; Bawendi, M. G.; Kastner, M. A.; Markovic, N.; Tinkham M. "Imaging the Charge Transport in Arrays of CdSe Nanocrystals", *Appl. Phys. Lett.* **2003**, *83*, 4008-4010.

28. Hu, Z.; Fischbein, M. D.; Drndić, M. "Local Charge Transport in Two-Dimensional PbSe Nanocrystal Arrays Studied by Electrostatic Force Microscopy", *Nano Lett.* **2005**, *5*, 1463-1468.

29. Whetten, R. L.; Khoury, J. T.; Alvarez, M. M.; Murthy, S.; Vezmar, I.; Wang, Z. L.; Stephens, P. W.; Cleveland, C. L.; Luedtke, W. D.; Landman, U. "Nanocrystal Gold Molecules", *Adv Mater.* **1996**, *8*, 428-433.

30. Cleveland, C. L.; Landman, U.; Shafigullin, M. N.; Stephens, P. W.; Whetten, R. L. "Structural Evolution of Larger Gold Clusters", *Z. Phys. D* **1997**, *40*, 503-508.

31. Cleveland, C. L.; Landman, U.; Schaaf, T. G.; Shafigullin, M. N.; Stephens, P. W.; Whetten, R. L. "Structural Evolution of Smaller Gold Nanocrystals: The Truncated Decahedral Motif", *Phys. Rev. Lett.* **1997**, *79*, 1873-1876.

32. Alvarez, M. M.; Khoury, J. T.; Schaaff, T. G.; Shafigullin, M. N.; Vezmar, I.; Whetten, R. L. "Optical Absorption Spectra of Nanocrystal Gold Molecules", *J. Phys. Chem. B* **1997**, *101*, 3706-3712.

33. Hostetler, M. J.; Wingate, J. E.; Zhong, C.-J.; Harris, J. E.; Vachet, R. W.; Clark, M. R.; Londono, D.; Green, S. J.; Stokes, J. J.; Wignall, G. D.; Glish, G. L.; Porter, M. D.; Evans, N. D.; Murray, R. W. "Alkanethiolate Gold Cluster Molecules with Core Diameters from 1.5 to 5.2 nm: Core and Monolayer Properties as a Function of Core Size", *Langmuir* **1998**, *14*, 17-30.

34. Chen, S.; Ingram, R. S.; Hostetler, M. J.; Pietron, J. J.; Murray, R. W.; Schaaf, T. G.; Khoury, J. T.; Alvarez, M. M.; Whetten, R. L. "Gold Nanoelectrodes of Varied Size: Transition to Molecule-Like Charging", *Science* **1998**, *280*, 2098-2101.

35. Hicks, J. F.; Templeton, A. C.; Chen, S.; Sheran, K. M.; Jasto, R.; Murray, R. W. "The Monolayer Thickness Dependence of Quantized Double-Layer Capacitances of Monolayer-Protected Gold Clusters", *Anal. Chem.* **1999**, *71*, 3703-3711.

36. Alvarado, S. F.; Seidler, P. F.; Lidzey, D. G.; Bradley, D. D. C. "Direct Determination of the Exciton Binding Energy of Conjugated Polymers Using a Scanning Tunneling Microscope", *Phys. Rev. Lett.* **1998**, *81*, 1082-1085.

37. Alvarado, S. F.; Rossi, L.; Muller, P.; Seidler, P. F.; Riess, W. "STM-Excited Electroluminescence and Spectroscopy on Organic Materials for Display Applications", *IBM J. Res. Dev.*, **2001**, *45*, 89-100.

38. Alvarado, S. F.; Barth, S.; Bussler, H.; Scherf, U.; van der Horst, J. W.; Bobbert, P. A.; Michels, M. A. J. "Spatially Resolved STM Spectroscopy of Charge Injection at the Ladder-Type Poly(para-phenylene)/Au(111) Interface", *Adv. Funct. Mater*. **2002**, *12*, 117-122.

39. Brust, M.; Walker, M.; Bethell, D.; Schiffrin, D. J.; Whyman, R. "Synthesis of Thiol-Derivatized Gold Nanoparticles in a 2-Phase Liquid-Liquid System", *J. Chem. Soc., Chem. Commun.* **1994**, 801-802.

40. Quinn, A. J.; Biancardo, M.; Floyd, L.; Belloni, M.; Ashton, P. R.; Preece, J. A.; Bignozzi, C. A.; Redmond, G. "Analysis of Charge Transport in Arrays of 28 kDa Nanocrystal Gold Molecules", *J. Mater. Chem.* **2005**, *12*, 4403-4407.

41. Terrill, R. H.; Postlethwaite, T. A.; Chen, C.; Poon, C.; Terzis, A.; Chen, A.; Hutchison, J. E.; Clark, M. R.; Wignall, G.; Londono, J. D.; Superfine, R.; Falvo, M.; Johnson Jr., C. S.; Samulski, E. T.; Murray, R. W. "Monolayers in Three Dimensions: NMR, SAXS, Thermal, and Electron Hopping Studies of Alkanethiol Stabilized Gold Clusters", *J. Am. Chem. Soc.* **1995**, *117*, 12537.

42. Hicks J. F., Zamborini F. P., Murray R. W. "The Dynamics of Electron Transfers Between Electrodes and Monolayers of Nanoparticles", *J. Phys. Chem. B* **2002**, *106*, 7751-7757.

43. Quinn, A. J.; Beecher, P.; Iacopino, D.; Floyd, L.; De Marzi, G.; Shevchenko, E. V.; Weller, H., Redmond, G. "Manipulating the Charging Energy of Nanocrystal Arrays", *Small* **2005**, *1*, 613-618.

44. Rampi, M. A.; Schueller, O. J. A.; Whitesides, G. M. "Alkanethiol Self-Assembled Monolayers as the Dielectric of Capacitors with Nanoscale Thickness", *Appl. Phys. Lett.* **1998**, *72*, 1781-1783.

45. Biancardo, M.; Quinn, A. J.; Floyd, L.; Mendes, P. M.; Briggs, S. S.; Preece, J. A.; Bignozzi, C. A.; Redmond, G. "Hysteresis of Charge Tunneling in Assemblies of Carboxylic Acid-Modified Gold Nanoparticles", *J. Phys. Chem. B* **2005**, *109*, 8718-8722.

46. Luedtke, W. D.; Landman, U. "Structure, Dynamics, and Thermodynamics of Passivated Gold Nanocrystallites and Their Assemblies", *J. Phys. Chem. B* **1996**, *100*, 13323-13329.

47. Grabert, H.; Devoret, M. H. (ed.) Single Charge Tunneling, Plenum Press: New York, **1992**.

48. Hanna, A. E.; Tinkham M. "Variation of the Coulomb Staircase in a 2-Junction System by Fractional Electron Charge", *Phys. Rev. B* **1991**, *44*, 5919-5922.

49. Black, C. T.; Tuominen, M. T.; Tinkham M. "Voltage-Activated Charge Motion Measured by a Mesoscopic 2-Tunnel-Junction System", *Phys. Rev. B* **1994**, *50*, 7888-7892.

50. Bar-Sadeh, E.; Goldstein, Y.; Zhang, C.; Deng, H.; Abeles, B.; Millo, O. "Single-Electron Tunneling Effects in Granular Metal-Films", *Phys. Rev. B* **1994**, *50*, 8961-8964.

51. Parthasarathy, R.; Lin, X. M.; Elteto, K.; Rosenbaum, T. F.; Jaeger, H. M. "Percolating Through Networks of Random Thresholds: Finite Temperature Electron Tunneling in Metal Nanocrystal Arrays", *Phys. Rev. Lett.* **2004**, *92*, art. no. 076801.

52. Elteto, K.; Antonyan, E. G.; Nguyen, T. T.; Jaeger, H. M. “Model for the Onset of Transport in Systems with Distributed Thresholds for Conduction”, *Phys. Rev. B* **2005**, *71*, art. no. 064206.

53. Elteto, K.; Lin, X. M.; Jaeger, H. M. “Electronic Transport in Quasi-One-Dimensional Arrays of Gold Nanocrystals”, *Phys. Rev. B* **2005**, *71*, art. no. 205412.

54. Cui, X. D.*;* Primak, A.*;* Zarate, X.*;* Tomfohr, J.*;* Sankey, O. F.*;* Moore, A. L.*;* Moore, T. A.*;* Gust, D.*;* Harris, G.*;* Lindsay, S. M. “Reproducible Measurement of Single-Molecule Conductivity”, *Science* **2001**, *294*, 571-574.

55. Dadosh, T.*;* Gordin, Y*;* Krahne, R.*;* Khivrich, I.*;* Mahalu, D.*;* Frydman, V.*;* Sperling, J.*;* Yacoby, A.*;* Bar-Joseph, I. “Measurement of the Conductance of Single Conjugated Molecules”, *Nature* **2005**, *436*, 677-680.

Chapter 4

Polythiophene Nanowires: Synthesis by Template Wetting and Local Electrical Characterisation of Single Wires

4.1 Introduction

One-dimensional (1-D) nanostructures fabricated from conducting polymers and small organic molecules have attracted increasing research interest due to their unique physical, chemical and electronic properties, together with the wide variety of potential applications envisaged for such structures in the field of nanoscience.[1-26] A range of techniques has been employed for fabrication of organic nanowires and nanotubes.[1,3,5-6,8-10] In particular, template synthesis in porous anodised alumina membranes is a key method since it offers the potential for production of ordered arrays of nanotubes or nanowires with good control over structural parameters such as diameter, length, wall thickness (in the case of tubes) and areal density. This technique has been employed for fabrication of arrays of 1-D nanostructures from metals, semiconductors and ceramics via electrodeposition, and also from organic materials via electropolymerization.[1-4]

Recently, a new method for formation of organic nanowires and nanotubes by template wetting has been reported.[14] This approach has shown itself to be a versatile reagentless method for formation of 1-D organic nanostructures without the need for the specific monomers that are typically required for electropolymerisation. Melt- and solution-assisted template wetting methods do not require specialised apparatus and are broadly applicable across a wide range of organic materials including small molecules, oligomers, polymers, blends and multi-component solutions.[14,18-20]

In particular, melt-assisted template wetting has extended the range of processable materials to include high molecular weight polymers, blends and composite materials not amenable to processing using other techniques, *e.g.*, polytetrafluoroethylene (PTFE), polystyrene (PS), polymethyl methacrylate (PMMA) and palladium-polystyrene composites.[14,20] For melt-assisted wetting, the organic material of choice is placed on an alumina pore array and heated above its glass transition temperature or melting point. Due to the high surface energy of the alumina membrane, a thin surface film of organic material will rapidly cover the pore walls in the initial stages of wetting, forming nanotubes with well-defined wall thicknesses.[14] Formation of nanowires takes place on longer time scales because the cohesive forces required for pore filling are considerably weaker than the adhesive forces involved in wall wetting.[14]

In this chapter,[♦] the method of melt-assisted template wetting is exploited for controlled high-yield synthesis of organic semiconductor nanowires from regioregular poly-(3-hexylthiophene) (RR-P3HT). Following synthesis, the wires were liberated from the templates using sodium hydroxide and dispersed on insulating substrates. Their local structural and electronic properties were investigated using scanning electron microscopy (SEM) and conducting-probe atomic force microscopy (CP-AFM). CP-AFM is a useful tool in this regard, since it allows non-invasive imaging and local electrical characterisation of 1-D nanostructures.[12,13,27-30] The produced P3HT polymer nanowires were found to have average lengths ~ 10 μm and diameters ~ 450 nm. Two-terminal electrical contacting of individual nanowires on thermally oxidised silicon substrates was undertaken using a shadow mask evaporated titanium/gold drain electrode, and a CP-AFM tip as the (mobile) source electrode. This approach permitted both topographic imaging and spatially resolved electrical characterisation of individual nanowires. The resulting data allowed the intrinsic nanowire resistivity, as well as the total nanowire-electrode contact resistance to be estimated. Fits to a thermionic emission-diffusion model further allowed the single nanowire hole mobility and the mean nanowire-electrode barrier height to be evaluated.

♦ This work will be published as "Polythiophene Nanowires: Synthesis by Template Wetting and Local Electrical Characterization of Single Wires", *J. Mater. Chem.* accepted.

4.2 Brief Description of the Proposed Approach

The structure of the anodised alumina membranes utilised as templates for controlled high yield synthesis of organic semiconductor nanowires is illustrated in Figure 4.1. The membranes are fabricated by electrochemically anodising aluminium under bias in an acidic medium. The membranes feature a high density of similarly sized pores over the entire range of each membrane. A feature of such pores is branching, which is observed on one side of the membrane extending over several μm in depth from the membrane surface; this is apparent when the membranes are cross sectioned and is illustrated in the magnified schematic view of the upper surface of a membrane shown in Figure 4.1. Branching can be intentionally induced by reducing the anodising voltage by a factor of $1/\sqrt{2}$ but may also occur due to random fluctuations in the anodising voltage or temperature during the fabrication process.[31,32]

In order to fabricate nanowires, it is necessary to completely fill these pores with the desired material, e.g., conjugated polymer, and then to liberate the nanowires from the membrane in an undamaged state. The filling of the pores typically occurs in a two stage process: Initially a wetting process occurs with an extremely thin precursor film emanating from a macroscopic polymer droplet, rapidly covering the substrate.[33,34] Organic materials are characterised by low surface energies, whereas inorganic materials are characterised by high surface energies. Low energy liquids spread rapidly on high-energy surfaces. Hence, a mesoscopic polymer wetting film will cover the pore walls of the alumina membrane template on a very short time scale. The underlying driving forces are due to van der Waals interactions between the wetting liquid and the pore walls. After the wetting layer has been formed, the strong adhesive forces are neutralised as a kinetically stable stationary state is achieved. The cohesive forces that drive a complete filling of the template pores are much weaker and have to overcome the viscous

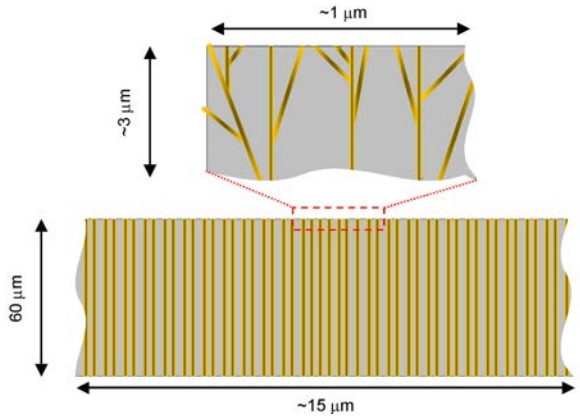

Figure 4.1. Cross-sectional schematic of an anodised alumina membrane illustrating the structure of the membrane and the density of the pores. The expanded view highlights the random branching of the pores on one side of the membrane

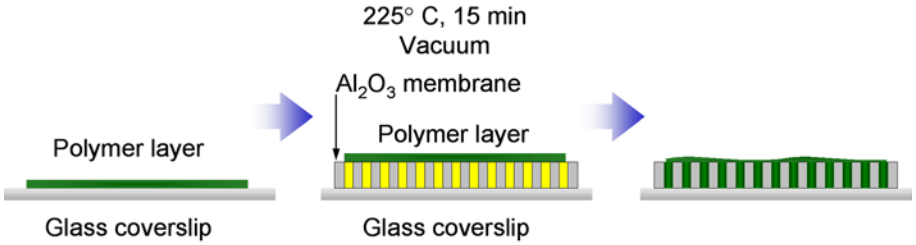

Figure 4.2. Schematic representation of the template melt wetting synthesis technique. A dried drop cast layer of P3HT was peeled from a glass coverslip and deposited onto the branched side of an anodised alumina membrane. After annealing at 225 °C for 15 minutes in vacuum, most of the pores had been filled with the molten polymeric material.

forces of the wetting liquid, which are of considerable strength. Formation of nanowires therefore subsequently takes place on longer time scales because the cohesive forces required for pore filling are considerably weaker than the adhesive forces involved in wall wetting.

The melt-assisted template wetting technique employed in this work is illustrated in Figure 4.2. Here a drop of high concentration polymer solution is deposited onto a glass coverslip and allowed to dry. Once the layer has dried, it is carefully delaminated from the supporting coverslip and placed onto a porous membrane. The layer is placed on the branched side of the membrane in order to promote pore filling and also to prevent the membrane from curling as it fills, for ease of processing at later stages. Heating the organic layer above its glass transition temperature or melting point allows the polymer to flow into the membrane pores. Sufficient time is allowed to permit the membrane to fill completely, typically 15 minutes, such that nanowires are formed rather than nanotubes.

Upon cooling, any excess material remaining on the membrane surface can be removed using a blade followed by a polish with fine sandpaper to expose the surface of the membrane. The nanowires can then be liberated from the membrane by selectively etching the membrane material away. This can be achieved using either phosphoric acid or aqueous NaOH solution.

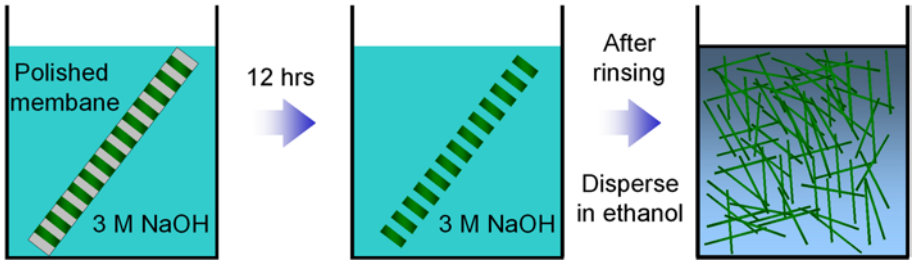

Figure 4.3. Schematic representation of the protocol utilised to liberate nanowires from the template. The polished membrane is immersed in 3 M NaOH overnight to remove the template material. Following successive washing steps, it is possible to disperse the nanowires in ethanol.

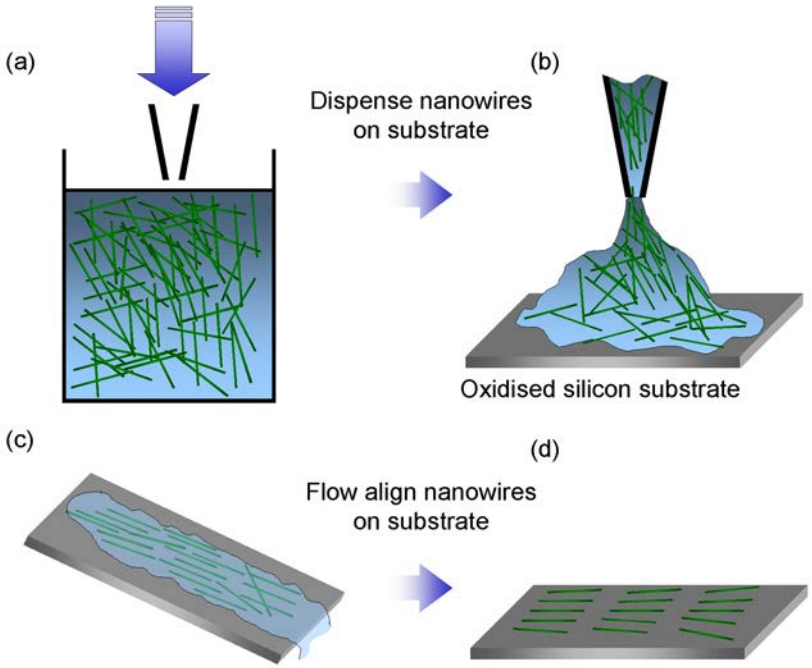

Figure 4.4. Schematic of the nanowire dispersal technique: (a) A drop of nanowires suspended in ethanol was dispensed onto a cleaned oxidised silicon substrate (b), which was then gently rinsed with multiple cycles of ethanol (c). This resulted in regions of well-aligned nanowires (d).

The latter approach is utilised in this work; see Figure 4.3 for a relevant schematic. Prolonged exposure of the filled membrane to the NaOH solution results in the complete dissolution of all membrane material, leaving clumps of nanowires suspended in the NaOH solution. Multiple cycles of rinsing leads to a large number of clean nanowires suspended in solution. Finally the wires are suspended in a dispersal solvent. The solvent is chosen so that it will not react with the polymer material and that it will have a low boiling point suitable for evaporation at room temperature once dispensed.

In order to disperse the nanowires on a substrate, the nanowire-loaded solvent is dispensed onto the desired substrate. The alignment of the nanowires can be varied from random to high orientation by post deposition flushing of the substrate with the host solvent. Multiple washes of the tilted substrate reduces the number of nanowires present on the substrate but results in regions of well oriented wires. This process is outlined in Figure 4.4.

Once the nanowires are dispersed onto the substrate it is possible to define electrodes using a simple shadow mask and thermal evaporation of metal contacts onto the nanowires. Various electrode configurations are achievable using this approach, ranging from a single electrode contacting multiple wires to two terminal connections to individual wires. As a CP-AFM tip was used as a mobile electrode in this work, it was only necessary to define a single contact to

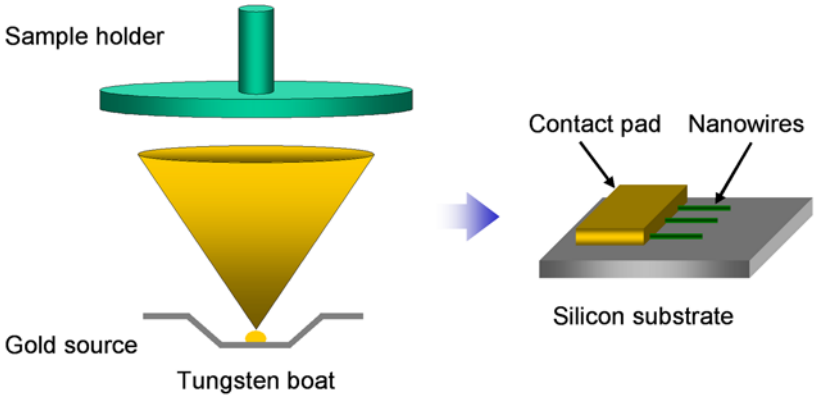

Figure 4.5. Schematic representation of the thermal evaporation technique utilised to make electrical contact to multiple nanowires. A single contact pad was deposited perpendicular to the alignment direction of the nanowires using a shadow mask.

the aligned wires; see Figure 4.5.

Figure 4.6 shows the experimental configuration for single nanowire electrical measurement using CP-AFM. Initially, topographic images of the region of interest are acquired in AFM tapping mode to identify suitably contacted wires. Following selection of an appropriate wire, the probe is retracted and the microscope is switched to AFM contact mode for the current-voltage (*I*-*V*) measurements. A drain bias is applied to the shadow-evaporated electrode and the metallised AFM probe acts as the source electrode, which can be positioned at various points along the wire axis for spatially resolved *I*-*V* measurements.

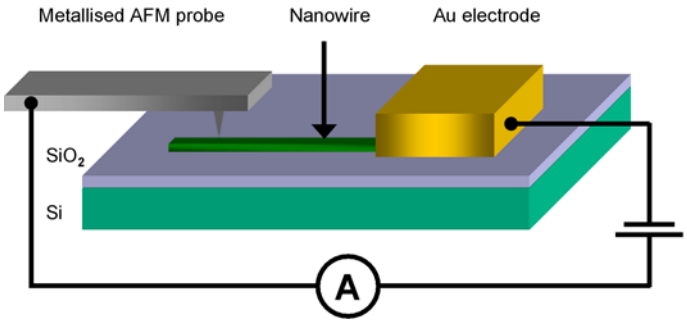

Figure 4.6. Schematic representation of the conducting-probe atomic force microscopy (CP-AFM) measurement configuration. Spatially resolved current-voltage (*I*-*V*) measurements are acquired by electrically contacting a polymer nanowire using an evaporated gold electrode as the fixed drain electrode, and a metallised AFM probe as a mobile source electrode.

4.3 Experimental

4.3.1 Synthesis of Nanowires

Reagents and solvents were purchased from Sigma-Aldrich Ireland Ltd., and used without purification unless otherwise stated. Nanowires of regioregular poly-(3-hexylthiophene) (M_W ~ 87000 g/mol with > 98.5 % regioregularity) were fabricated in commercial anodised alumina membranes (Anodisc 13, Whatman Ltd.; 200 nm nominal pore diameter) by the melt-assisted wetting method as outlined in the previous section. Briefly, 80 μL of a 20 mg/mL solution of P3HT in tetrahydrofuran (THF) was drop cast onto a glass coverslip in an inert atmosphere glovebox and left to dry. After removing the glass coverslip from the glovebox, it was soaked in a 3 M aqueous solution of sodium hydroxide (NaOH) for 10 seconds, rinsed with deionised water (Millipore; Q, > 18 MΩcm) and blown dry using a nitrogen flow. This process partially delaminated the P3HT layer from the glass. The P3HT layer was peeled off from the glass support and deposited onto an alumina membrane, which was then returned to the glove box. The membrane was annealed in vacuum at 225 ºC for 15 minutes, in order to melt inject the polymer into the porous template, and was then slowly cooled to room temperature. A razor blade was used to remove excess P3HT from the alumina membrane followed by polishing with 1200 grid sand paper. In order to liberate the nanowires from the membrane and disperse them in solution, the following protocol was followed: The polished membrane was soaked in 3 M aqueous NaOH overnight and subsequently sonicated for 15 minutes. After settling, the NaOH supernatant was decanted off and replaced with deionised H_2O. The suspension was sonicated for 10 minutes (FS100B, Decon Laboratories Ltd.; 40 kHz, 75 W), allowed to settle and the H_2O supernatant was decanted off and replaced with decane. Excess organic residue was then removed by three cycles of sonication (1 minute), centrifugation (8000 rpm, 1 minute), removal of the supernatant and addition of fresh decane. Following the final centrifugation step, the decane supernatant was decanted off, replaced with ethanol and the solution was manually agitated to disperse the nanowires. Scanning electron microscopy images (SEM) were acquired using a field emission SEM (JSM-6700F, Jeol UK Ltd.) operating at beam voltages between 1 and 10 kV.

4.3.2 Device Fabrication and Characterisation

Oxidised silicon substrates (*n* type, 2-4 Ωcm, 100 nm thermal oxide) were solvent cleaned by sonication in trichloroethylene, acetone and isopropanol for 5, 4 and 3 minutes, respectively. The substrates were then dried using a nitrogen flow. Nanowires were dispersed and aligned by drop deposition onto a tilted substrate. The substrate was gently rinsed by multiple cycles of drop deposition with ethanol. As-deposited nanowires were structurally characterised using a

Topometrix Explorer atomic force microscope (AFM) system using commercial tapping mode AFM probes (Nanosensors NCHR; typical radius of curvature ~ 10 nm and front/rear cone angles of 22.5 º / 27.5 º, respectively).

4.3.3 Electrical Characterisation of Single Nanowires

Electrical contacts to deposited aligned nanowires were fabricated using shadow masking and thermal evaporation of metal (20 nm Ti / 300 nm Au). A single electrode contact pad was deposited perpendicular to the alignment direction of the nanowires. Contacted nanowires were then imaged using a JEOL (JSPM 4200, JEOL U.K. Ltd.) scanning probe microscope. The AFM measurements were performed under ambient conditions. For nanowire imaging commercial tapping mode AFM probes (Nanosensors NCHR; details as above) were used. For local electrical characterisation commercial PtIr coated tapping mode AFM probes (Nanosensors NCHPt; typical radius of curvature ~ 20 nm) were used.

Once a suitable nanowire was located by AFM imaging, it was possible to conduct two-probe transport measurements using the PtIr coated AFM probes, in contact mode, where the tip acted as a movable source electrode (virtual ground) and the evaporated Ti/Au contact pad acted as the drain, which was biased. Current versus drain voltage (*I*-*V*) sweeps were acquired at selected locations along the length of the nanowire using the minimum contact loading. For each measurement the drain bias, V_{Drain}, was swept from 10 V to –10 V in 38 mV steps. Control *I*-*V* measurements were acquired on evaporated Ti/Au electrode contact pads and also on the SiO_2 top surface of the oxidised silicon substrates.

4.4 Results and Discussion

4.4.1 Physical Characterisation of Anodised Alumina Membranes

Figure 4.7(a) shows a scanning electron microscope image of the bottom surface of an as-received porous alumina membrane. The membrane is characterised by an extremely high density of pores, ~ 10^9 cm^{-2}. The diameter of the pore openings was determined from statistical analysis of SEM images of the bottom surface of membranes. This analysis suggests that the pore mouth diameter is greater than the nominal value stated by the manufacturer, with a broad distribution centred in the range 250 nm to 300 nm. The cross sectional SEM image of a broken membrane shown in Figure 4.7(b) shows that the pores are almost uniformly aligned perpendicular to the membrane surface and that the pore branching occurs just beneath the membrane surface as described in section 4.2 above. The diameter of individual pore channels

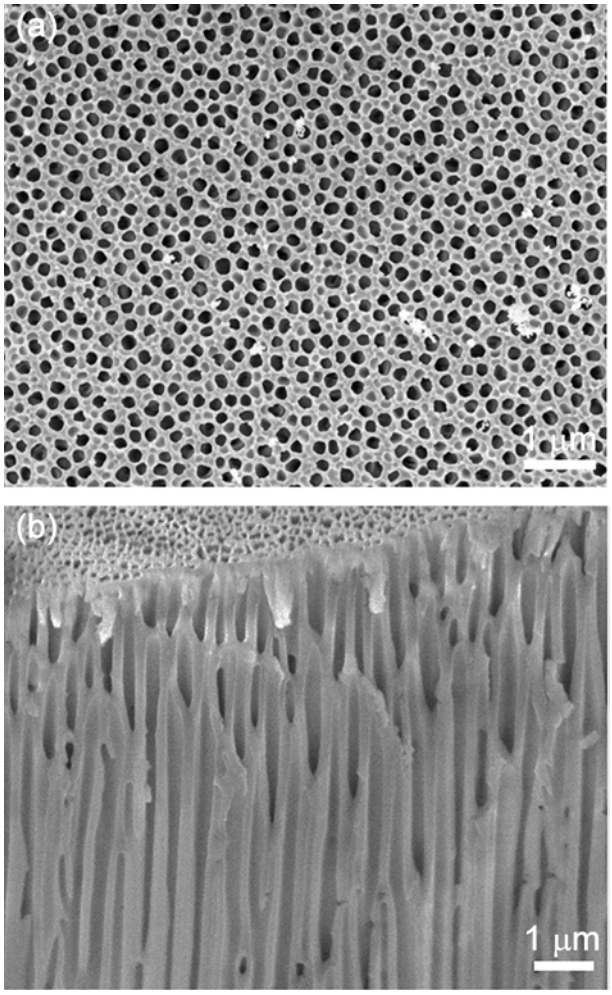

Figure 4.7. Scanning electron microscopy images of (a) the bottom surface of an as-received anodised alumina membrane, and of (b) the same membrane in cross section, the large number of openings at the membrane surface relative to the number of pores visible in cross section is indicative of pore branching just beneath the membrane surface.

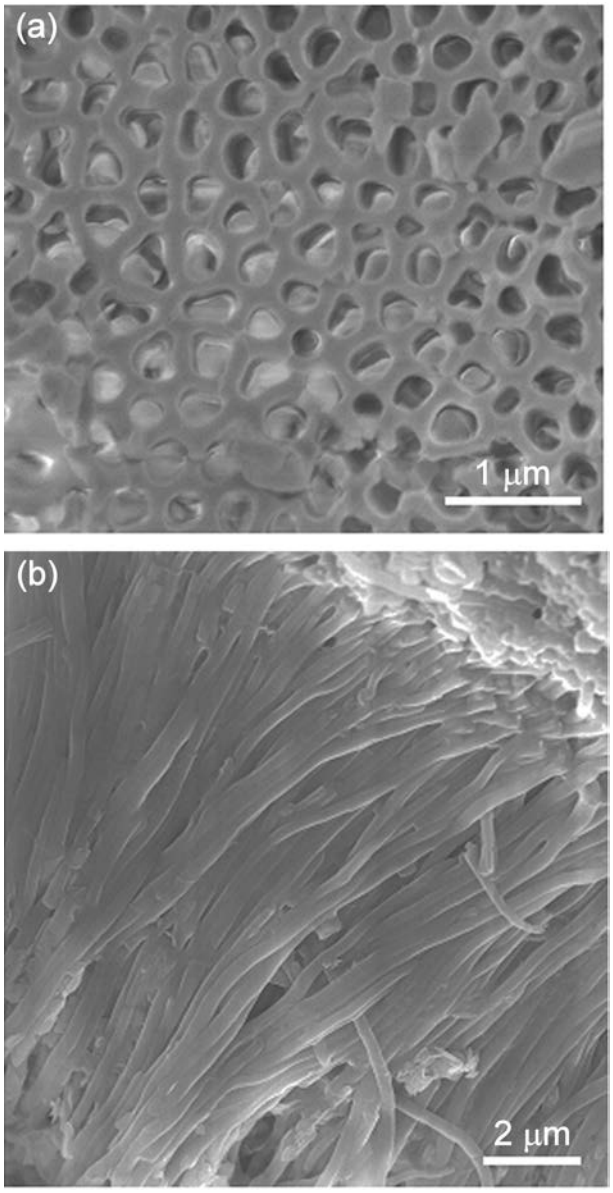

Figure 4.8. Scanning electron microscopy images of (a) the bottom surface of a cleaned, filled alumina template following melt-assisted filling of P3HT from the top surface of the template, and (b) an array of P3HT nanowires following partial dissolution of the alumina template.

appears to be uniform throughout the depth of the membrane also.

4.4.2 Physical Characterisation of P3HT Nanowires

Figure 4.8(a) shows a SEM image of the bottom surface of a filled porous alumina membrane, following melt-assisted injection of P3HT from the top surface of the template. Excess material remaining on the membrane surface was removed, as described in section 4.2 above, using a blade followed by a polish with fine sandpaper to expose the surface of the

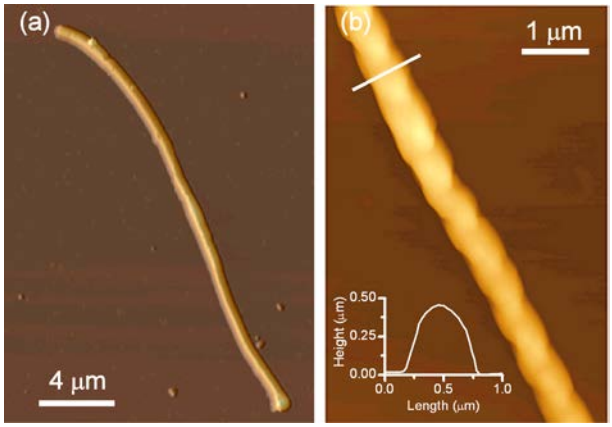

Figure 4.9. (a) Tapping mode atomic force microscopy image of a P3HT nanowire as-deposited on an oxidised silicon substrate. (b) High-resolution AFM image of the nanowire showing periodic granularity. Inset: Topography profile obtained along white line in main panel.

membrane prior to imaging. The high density of filled pores (~ 10^9 cm^{-2}) indicates almost complete filling of the template during melt injection, resulting in high-yield formation of wires with maximum lengths on the order of the template thickness (~ 60 μm). Figure 4.8(b) shows a cross sectional SEM image of an array of P3HT nanowires following partial dissolution of the alumina template using aqueous NaOH. The image demonstrates the efficiency of the melt-assisted wetting process for high-yield preparation of these 1-D nanostructures. The nanowires were freed from the template by completely dissolving the alumina in aqueous NaOH and were ultimately dispersed in ethanol following several cycles of washing by sonication and centrifugation. For dispersion protocols where only a single sonication step was employed, few single wires were observed and the majority of the wires formed bundles. In fact, multiple sonication steps were required to liberate and disperse the wires fully. It was found that the mean nanowire length decreased as a function of the number of sonication steps, resulting in a mean wire length ~ 10 μm, measured for dispersed single wires following a total of five sonications. Individual wires with lengths up to 30 μm were also observed at low number density (less than 1 in 50).

Figure 4.9(a) shows a tapping mode atomic force microscopy image of a typical wire, with a total length greater than 20 μm, deposited on an oxidised silicon substrate. The wire morphology appears smooth with a low density of defects. Extensive radial curvature was observed for the majority of dispersed single wires, indicating appreciable flexibility of these nanostructures. Figure 4.9(b) shows a high resolution scan over a part of the nanowire. The nanowire appears granular, with ellipsoidal grains ~ 700 nm long (i.e., grain aspect ratio ~1.4). This granularity suggests partial local dewetting of the molten polymer material from the pore

walls during wire formation, possibly as a result of competition between the cohesive forces driving wire formation and the adhesive forces driving wetting of the pore walls.[14] The inset to Figure 4.9(b) shows a typical line profile across the nanowire; the measured maximum height at this location is 450 nm. Since the nanostructure height is unaltered by tip-induced lateral broadening effects, the heights measured in AFM images were taken to represent the actual nanowire diameters. A value of 450 nm for the nanowire diameter is greater than the range of 250 – 300 nm measured for the diameter of the pore openings in section 4.4.1 above. However, observation of nanowires with diameters ranging from 250 nm to 550 nm was found to be commonplace during this work.

4.4.3 Electrical Characterisation of P3HT Nanowires

Prior to electrical analysis of individual P3HT nanowires, control *I-V* measurements were acquired in order to characterise the CP-AFM system. *I-V* curves acquired on evaporated titanium/gold electrode contact pads were found to be linear and reproducible with a resistance value ~ 10 kΩ, indicating formation of good electrical contacts between the PtIr coated CP-AFM tip and the conductive electrodes; see Figure 4.10(a). These measured values are close to that of a quantum point contact resistance ~ 13 kΩ, suggesting that the small contact area between the PtIr coated tip and the gold surface dominate the transport. *I-V* curves acquired on the SiO_2 top surface of the oxidised silicon substrates demonstrated negligible current flow with measured currents $I < 10$ pA for $V_{Drain} \leq 10$ V, corresponding to leakage resistances $R > 1$ TΩ as expected for a high quality thermally grown oxide layer; see Figure 4.10(b). Therefore, on the basis of this data, it was considered a reasonable assertion that *I-V* curves measured by CP-AFM on individual P3HT nanowires were dominated by conduction through the nanowire itself.

Concerning single nanowire characterisation, the bottom inset of Figure 4.11 shows an AFM image of a P3HT nanowire contacted using the shadow masking method described in section 4.2. The mean diameter for this wire was measured (using the maximum height from multiple line profiles) to be $d = 555 \pm 17$ nm, with a corresponding circular cross sectional area $A = \pi d^2/4 = 0.24 \pm 0.05$ μm^2. The main panel of Figure 4.11 shows a set of CP-AFM *I-V* curves obtained at various locations along the length of the nanowire, corresponding to the coloured symbols shown in the bottom inset. Several curves were acquired at each measurement location to ensure reproducibility. The distance from the edge of the fixed drain electrode to the metallised AFM probe (source electrode), *L*, was determined from measured topography data. Each *I-V* curve shows symmetric non-linear behaviour at high drain bias, with monotonically decreasing current at a given drain voltage as *L* increases.

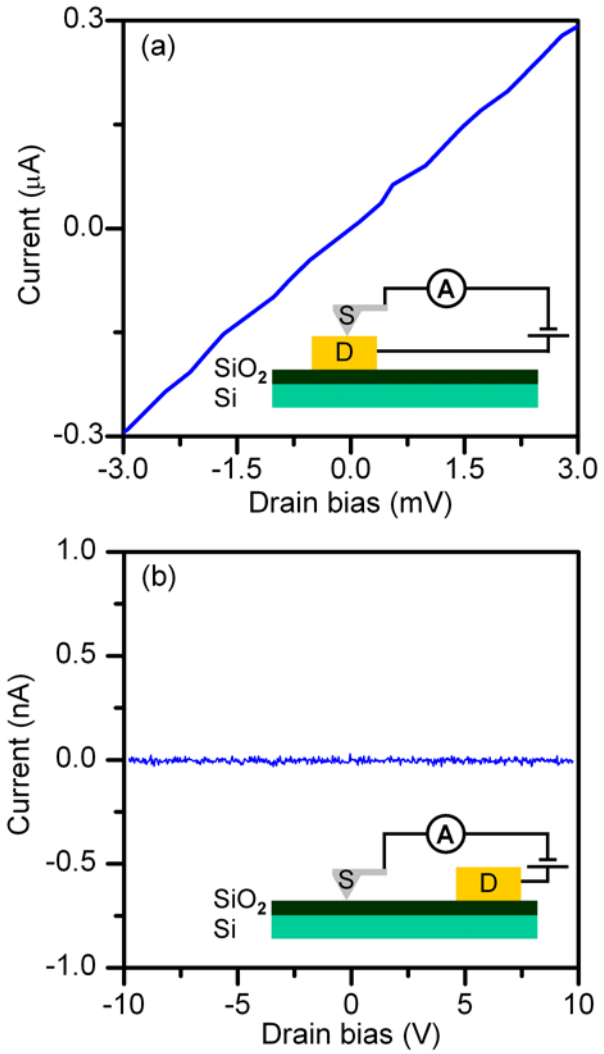

Figure 4.10. (a) Current-voltage characteristics acquired by CP-AFM on (a) a Ti/Au electrode contact pad evaporated onto an oxidised Si substrate, and on (b) the SiO_2 top surface of the substrate itself. Insets: Schematic representations of the measurement approaches employed.

The nanowire resistance (R) at each measurement location was calculated from the inverse slope of the corresponding I-V curve at high drain bias (6 V < V < 10 V). Figure 4.12 shows the measured resistance values as a function of distance from the drain electrode. The R versus L data are well described by a simple linear fit with a linear correlation coefficient of 0.97. This linear fit can be written as $R = R_{contact} + \rho L/A$, where $R_{contact}$ is the sum of the parasitic series resistances at the source and drain electrodes, ρ is the intrinsic nanowire resistivity and A is the cross-sectional area of the nanowire ($A = 0.24 \pm 0.05$ μm^2). This total contact resistance is equal to the intercept of the linear fit, $R_{contact} = 2.4 \pm 0.7$ GΩ. The contact resistance is a substantial fraction of the total device resistance at all measurement locations.

Contact resistance remains a significant problem in polymer based devices such as

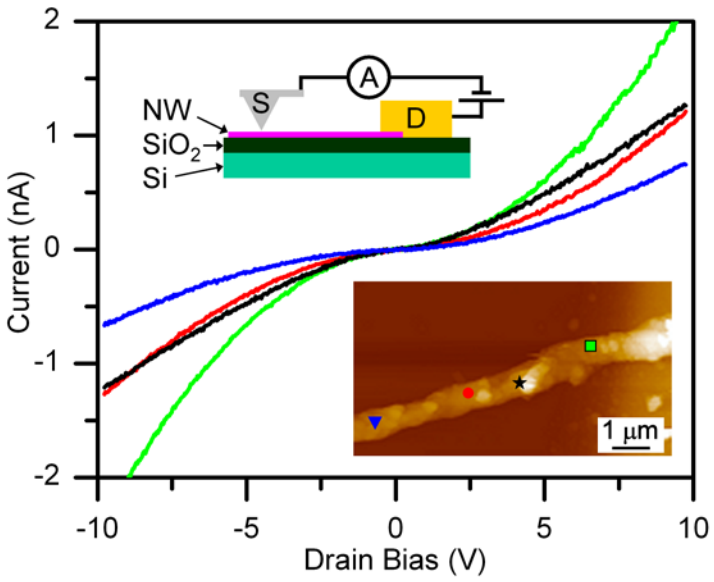

Figure 4.11. Measured CP-AFM current-voltage characteristics of the P3HT nanowire device shown in the bottom inset acquired using the approach schematised in the top inset. Bottom inset: Tapping mode AFM image of the contacted nanowire. The Ti/Au drain electrode is located to the right of the image and the coloured symbols indicate the locations at which local *I-V* measurements were performed. Therefore, the colour of each *I-V* characteristic shown in the main panel denotes the location along the nanowire at which that data was acquired.

transistors and light-emitting diodes, especially for bottom-contact geometries, and even for devices with large width-length ratios ($W/L \sim 10^1$ - 10^3).[21,22,37] By contrast, the nanowire devices fabricated here have significantly smaller width-length ratios. Assuming the drain electrode metal wraps around the nanowire, the maximum channel width will be on the order of half the nanowire circumference $W \sim \pi d/2 \sim 860$ nm. In fact, the actual channel width is likely to be even smaller due to the dimensions of the CP-AFM probe apex (diameter ~ 20 nm). The range of measured L values correspond to width-length ratios, $W/L < 0.01$ - 0.3, significantly smaller than for thin film devices fabricated from P3HT.[35-43] The specific contact resistivity, $\rho_c \approx R_{contact} W$ is often used to incorporate the effect of channel width on contact resistance. For the device with data shown in Figure 4.11, $\rho_c \sim 10^1$ - 10^3 Ωm, comparable to the lowest reported values for bottom-contact short channel devices. Merlo and Frisbie have reported $\rho_c \sim$ 2 - 10 Ωm for bottom- contacted web-like networks of P3HT polymer nanofibres, while Sirringhaus and co-workers have reported values of 5×10^2 Ωm for spun cast, bottom contacted, P3HT field effect transistors.[21,22,41]

Concerning the intrinsic nanowire resistivity, this parameter can be extracted from the slope of the linear fit to the data in Figure 4.12, $\rho = 160 \pm 35$ Ωm. This value is in good agreement

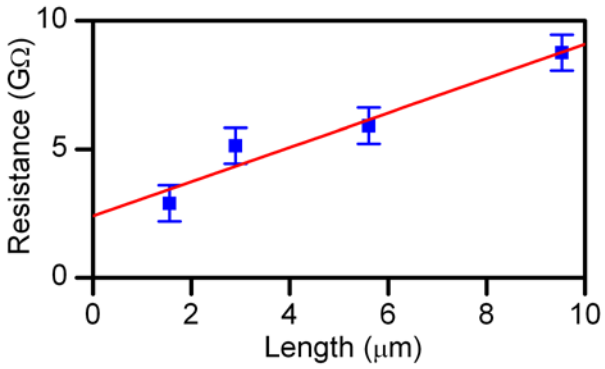

Figure 4.12. Nanowire resistance at high bias (R) extracted from the data shown in Figure 4.11 and plotted versus the distance of each measurement location from the drain electrode (L). The solid line shows a linear fit to the data, where the contact resistance is given by the intercept (2.4 ± 0.7 GΩ) and the intrinsic nanowire resistivity is proportional to the slope of the fit line (160 ± 35 Ωm).

with reported data of Valaski *et al.*, who determined a resistivity value of 110 Ωm for electrochemically deposited thin films of P3HT,[36] and in reasonable agreement with data measured by Bao *et al.* on thin film devices fabricated from unpurified RR-P3HT ($\rho \sim 10^3$ - 10^5 Ωm).[35] The extracted resistivity data indicate that the nanowires are likely to be (unintentionally) doped, possibly due to air exposure.[35,38]

Returning to the observed non-linearity in the measured *I-V* data, which is observed to increase quadratically with the applied bias voltage, such an effect is usually associated with space-charge limited current (SCLC) transport.[44] However, in this model, the current should also scale as $I \propto 1/L^3$, which is not supported by the measured data. Considering the *I-V* data acquired at $L \approx 1.5$ μm (Figure 4.13, squares) and at $L \approx 9.5$ μm (Figure 4.13, triangles), the SCLC model predicts a reduction in measured current for the same bias voltage by a factor of 250. In fact, even allowing for the effects of contact resistance, the measured current is only reduced by a factor ~ 10. The good agreement between the linear fit and the measured high bias resistance data shown in Figure 4.12 is more characteristic of ohmic transport ($I \propto V/L$). Since the measured data cannot be adequately described by either model for bulk transport, this indicates that charge injection effects must also be considered. Well known mechanisms for carrier injection into polymers include Fowler-Nordheim tunneling and thermionic emission.[44] Since the maximum electric fields employed in these measurements are below the accepted threshold for Fowler-Nordheim tunneling in polymers ($F < 10^7$ Vm^{-1}),[44] this mechanism is not expected to be significant and thermionic emission should have a greater influence on carrier injection.

For carrier transport in low-mobility semiconductors, diffusion effects must also be considered.[44] Equation 1 presents the thermionic emission-diffusion theory for the current (I) as a function of the electric field along the axis of the nanowire, where q is the carrier charge, μ is the hole mobility in a single nanowire, N_c is the carrier concentration, ϕ_b is the mean nanowire-electrode barrier height, k is Boltzmann's constant and T is the Kelvin temperature. Equation 2 includes the effect of the image force, which lowers the barrier height from its initial value ϕ_{b0} by an energy $\Delta\phi$, where ε_0 is the vacuum permittivity and ε_r is the polymer dielectric constant. Since the applied fields employed are low, it can be assumed that the device is operating under diffusion-limited current injection conditions, thus the electric field can be written $F(L) = V/L$.[44]

$$I(L) = \frac{qN_c\mu AV}{L}\exp\left(-\frac{q\phi_b}{kT}\right) \qquad 1$$

$$\phi_b = \phi_{b0} - \Delta\phi = \phi_{b0} - \sqrt{\frac{qV}{4\pi\varepsilon_0\varepsilon_r L}} \qquad 2$$

The solid curves in Figure 4.13 show the fits of equation 1 to the data of Figure 4.11 (showing every twentieth data point for clarity), taking ε_r = 3 and N_c = 2.5 × 10^{19} cm^{-3} from literature,[35,44] and treating μ and ϕ_{b0} as free parameters. From the fit to the data measured at the location closest to the drain electrode ($L \approx 1.5$ μm; Figure 4.13, squares) a single nanowire

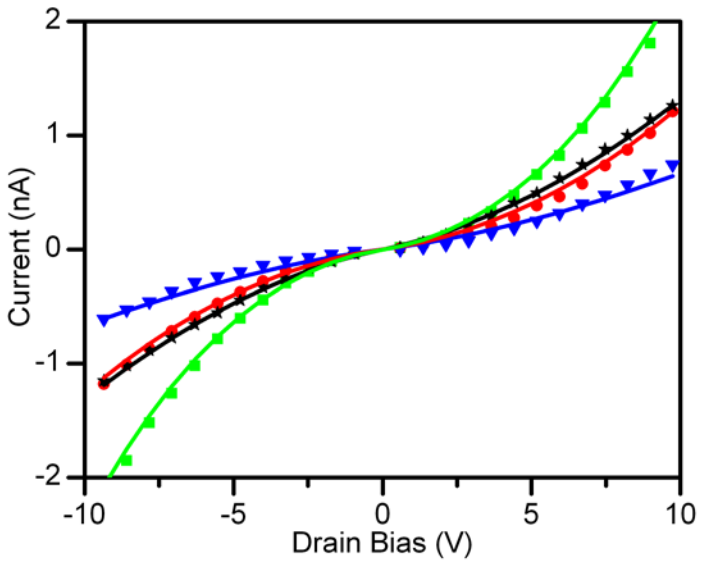

Figure 4.13. Measured CP-AFM current-voltage characteristics (symbols) of the P3HT nanowire shown in Figure 4.11. For clarity only every twentieth data point is shown. The symbols correspond to the locations at which each *I-V* measurement was made. The solid curves show fits to the data using the thermionic emission-diffusion model described in the text.

mobility value of $\mu \approx 2 \times 10^{-5}$ cm^2/Vs and a mean nanowire-electrode barrier height of $\phi_{b0} \approx 0.1$ eV were determined. Such barrier effects have been previously observed in Au-P3HT contacts.[37,42] For all other fits, the mobility was fixed at $\mu \approx 2 \times 10^{-5}$ cm^2/Vs while the barrier height was unconstrained as the tip-nanowire contact may not be identical in all cases, given the small loading forces used. The barrier height was found to decrease slightly with *L*. The extracted single nanowire mobility value ($\mu \approx 2 \times 10^{-5}$ cm^2/Vs) is comparable to early two-terminal measurements on thin films of poly(phenylene vinylene) derivatives ($\mu \sim 10^{-6}$ cm^2/Vs).[44]

While the single nanowire mobility value is significantly smaller than reported field-effect mobilities for highly-oriented RR-P3HT thin film and nanowire devices ($\mu \sim 10^{-3} - 10^{-1}$ cm^2/Vs),[21,22,38-40] a number of factors have been shown to have significant detrimental effects on measured mobility. These include energy disorder effects arising from charge localisation on polymer strands due to weak inter-chain coupling, the presence of defects, both in the polymer bulk and at the nanowire-SiO_2 substrate interface, and, finally, contact resistance and short channel effects arising from the nanowire dimensions. Concerning defects within the polymer, these can arise from exposure to chemical species, *e.g.*, NaOH,[23] or from photo-chemically induced species resulting from exposure to light or oxygen.[38] While some species may act as dopants, these defects can also behave as traps.[23] Finally, short channel effects have been shown to have a significant influence on measured device characteristics for P3HT devices with (sub)-micron channel lengths,[40] and contact resistance effects are also expected to have a significant effect as the width/length ratios scale down from planar/vertical device values ($W/L \sim 10^3$),[30,40] towards the dimensions of these nanowire devices ($W/L << 1$).

4.5 Conclusion

In this chapter, it has been shown that melt-assisted template wetting is a useful technique for the massively parallel fabrication of conjugated polymer nanowires. The physical and electrical characteristics of P3HT wires fabricated in this manner have been presented.

Structural characterisation indicated that the P3HT wires appear to be smooth with a low density of defects. The wires were found to have average lengths of ~ 10 μm and diameters ~ 450 nm while wires with length up to 30 μm were also observed. Extensive radial curvature was observed for the majority of dispersed single wires, indicating appreciable flexibility of these nanostructures. The nanowires are granular, which suggests partial local dewetting of the molten polymer material from the pore walls during wire formation. Once the operation of the CP-AFM system was validated, local structural and electronic characterisation of individual nanowires was undertaken. CP-AFM is a useful tool in this regard, as it allows non-invasive characterisation of nanostructures. Two-terminal electrical measurements of individual nanowires, utilising a CP-AFM tip as the source electrode, directly yielded values for the intrinsic nanowire resistivity and for the total nanowire-electrode contact resistance. Fits to a thermionic emission-diffusion model also allowed the single nanowire hole mobility and the mean nanowire-electrode barrier height to be evaluated.

It is proposed that application of the method of template wetting to the synthesis of conjugated polymer nanowires may be a potentially important future approach to the fabrication of polymer based electronic nanostructures.

4.6 References

1. Martin, C. R. “Template Synthesis of Polymeric and Metal Microtubules”, *Adv. Mater.* **1991**, *3*, 457-459.

2. Martin, C. R. “Nanomaterials a Membrane-Based Synthetic Approach”, *Science* **1994**, *266*, 1961-1966.

3. Martin C. R. “Template Synthesis of Electronically Conductive Polymer Nanostructures”, *Acc. Chem. Res.* **1995**, *28*, 61-68.

4. Hulteen, J. C.; Martin, C. R. “A General Template-Based Method for the Preparation of Nanomaterials”, *J. Mater. Chem.* **1997**, *7*, 1075-1087.

5. Schönenberger, C.; van der Zande, B. M. I.; Fokkink, L. G. J.; Henny, M.; Schmid, C.; Krüger, M.; Bachtold, A.; Huber, R.; Birk, H.; Staufer, U. “Template Synthesis of Nanowires in Porous Polycarbonate Membranes: Electrochemistry and Morphology”, *J. Phys. Chem. B*, **1997**, *101*, 5497-5505.

6. Johnson, S. A.; Khushalani, D.; Coombs, N.; Mallouk, T. E.; Ozin, G. A. “Polymer Mesofibres”, *J. Mater. Chem.* **1998**, *8*, 13-14.

7. Cepak, V. M.; Martin, C. R. “Preparation of Polymeric Micro- and Nanostructures Using a Template-Based Deposition Method”, *Chem. Mater.* **1999**, *11*, 1363.

8. MacDiarmid, A. G.; Jones Jr., W. E.; Norris, I. D.; Gao, J.; Johnson Jr., A. T.; Pinto, N. J.; Hone, J.; Han, B.; Ko, F. K.; Okuzaki, H.; Llaguno, M. “Electrostatically-Generated Nanofibers of Electronic Polymers”, *Synth. Met.* **2001**, *119*, 27-30.

9. Bognitzki, M.; Hou, H. Q.; Ishaque, M.; Frese, T.; Hellwig, M.; Schwarte, C.; Schaper, A.; Wendorff, J. H.; Greiner, A. “Polymer, Metal, and Hybrid Nano- and Mesotubes by Coating Degradable Polymer Template Fibers (TUFT Process)”, *Adv. Mater.* **2000**, *12*, 637-640.

10. Bognitzki, M.; Czado, W.; Frese, T.; Schaper, A.; Hellwig, M.; Steinhart, M.; Greiner, A.; Wendorff, J. H. “Nanostructured Fibers via Electrospinning”, *Adv. Mater.* **2001**, *13*, 70-72.

11. Park, J. G.; Kim, G. T.; Krstic, V.; Lee, S. H.; Kim, B.; Roth, S.; Burghard, M.; Park, Y. W. “Gating Effect in the I-V Characteristics of Iodine Doped Polyacetylene Nanofibers”, *Synth. Met.* **2001**, *119*, 469-470.

12. Park, J. G.; Kim, B.; Lee, S. H.; Park, Y. W. “Current-Voltage Characteristics of Polypyrrole Nanotube in Both Vertical and Lateral Electrodes Configuration”, *Thin Sol. Films.* **2001**, *438*, 118-122.

13. Park, J. G.; Lee, S. H.; Kim, B.; Park, Y. W. "Electrical Resistivity of Polypyrrole Nanotube Measured by Conductive Scanning Probe Microscope: The Role of Contact Force", *Appl. Phys. Lett.* **2002**, *81*, 4625-4627.

14. Steinhart, M.; Wendorff, J. H.; Greiner, A.; Wehrspohn, R. B.; Nielsch, K.; Schilling, J.; Choi, J.; Gösele, U. "Polymer Nanotubes by Wetting of Ordered Porous Templates", *Science* **2002**, *296*, 1997.

15. Yang, Y.; Wan, M. "Chiral Nanotubes of Polyaniline Synthesized by a Template-Free Method", *J. Mater. Chem.* **2002**, *12*, 897-901.

16. Ginzburg-Margau, M.; Fournier-Bidoz, S.; Coombs, N.; Ozin, G. A.; Manners, I. "Formation of Organometallic Polymer Nanorods Using a Nanoporous Alumina Template and the Conversion to Magnetic Ceramic Nanorods", *J. Chem. Soc., Chem. Commun.* **2002**, 3022-3023.

17. Sun, Z. C.; Zussman, E.; Yarin, A. L.; Wendorff, J. H.; Greiner, A. "Compound Core-Shell Polymer Nanofibers by Co-Electrospinning", *Adv. Mater.* **2003**, *15*, 1929-1932.

18. Zhao, L.; Yang, W.; Ma, Y.; Yao, J.; Li, Y.; Liu, H. "Perylene Nanotubes Fabricated by the Template Method", *J. Chem. Soc., Chem. Commun.* **2003**, 2442-2443.

19. Guo, Y.-G.; Li, C.-J.; Wan, L.-J.; Chen, D.-M.; Wang, C.-R.; Bai, C.-L.; Wang, Y.-G. "Well-Defined Fullerene Nanowire Arrays", *Adv. Funct. Mater.* **2003**, *13*, 626-630.

20. Steinhart, M.; Wendorff, J. H.; Wehrspohn, R. B. "Nanotubes à la Carte: Wetting of Porous Templates", *ChemPhysChem* **2003**, *4*, 1171-1176.

21. Merlo, J. A.; Frisbie, C. D. "Field Effect Conductance of Conducting Polymer Nanofibers", *J. Polym. Sci. Pol. Phys.* **2003**, *41*, 2674-2680.

22. Merlo, J. A.; Frisbie, C. D. "Field Effect Transport and Trapping in Regioregular Polythiophene Nanofibers", *J. Phys. Chem. B* **2004**, *108*, 19169-19179.

23. Duvail, J. L.; Rétho, P.; Fernandez, V.; Louarn, G.; Molinié, P.; Chauvet, O. "Effects of the Confined Synthesis on Conjugated Polymer Transport Properties", *J. Phys. Chem. B* **2004**, *108*, 18552-18556.

24. Kim, B. H.; Park, D. H.; Joo, J.; Yu, S. G.; Lee, S. H. "Synthesis, Characteristics, and Field Emission of Doped and De-Doped Polypyrrole, Polyaniline, Poly (3,4-ethylenedioxythiophene) Nanotubes and Nanowires", *Synth. Met.* **2005**, *150*, 279-284.

25. Gonzalez, R.; Pinto, N. J. "Electrospun Poly(3-hexylthiophene-2,5-diyl) Fiber Field Effect Transistor", *Synth. Met.* **2005**, *151*, 275-278.

26. Babel, A.; Li, D.; Xia, Y. N.; Jenekhe, S. A. "Electrospun Nanofibers of Blends of Conjugated Polymers: Morphology, Optical Properties, and Field-Effect Transistors", *Macromol.* **2005**, *38*, 4705-4711.

27. Bøggild, P.; Grey, F.; Hassenkam, T.; Greve, D. R.; Bjørnholm, T. "Direct Measurement of the Microscale Conductivity of Conjugated Polymer Monolayers", *Adv. Mater.* **2000**, *12*, 947-950.

28. Hassenkam, T.; Greve, D. R.; Bjørnholm, T. "Direct Visualization of the Nanoscale Morphology of Conducting Polythiophene Monolayers Studied by Electrostatic Force Microscopy", *Adv. Mater.* **2001**, *13*, 631-634.

29. de Pablo, P. J.; Gómez-Navarro, C.; Martínez, M. T.; Benito, A. M.; Maser, W. K.; Colchero, J.; Gómez-Herrero, J.; Baró, A. M. "Performing Current Versus Voltage Measurements of Single-Walled Carbon Nanotubes Using Scanning Force Microscopy", *Appl. Phys. Lett.* **2002**, *80*, 1462-1464.

30. Bockrath, M.; Markovic, N.; Shepard, A.; Tinkham, M.; Gurevich, L.; Kouwenhoven, L. P.; Wu, M. W.; Sohn, L. L. "Scanned Conductance Microscopy of Carbon Nanotubes and Lambda-DNA", *Nano Lett.* **2002**, *2*, 187-190.

31. Tian, Y. T.; Meng, G. W.; Gao, T.; Sun, S. H.; Xie, T.; Peng, X. S.; Ye, C. H.; Zhang L. D. "Alumina Nanowire Arrays Standing on a Porous Anodic Alumina Membrane", *Nanotechnology* **2004**, *15*, 189-191.

32. Routkevitch, D.; Bigioni, T.; Moskovits, M.; Xu, J. M. "Electrochemical Fabrication of CdS Nanowire Arrays in Porous Anodic Aluminum Oxide Templates", *J. Phys. Chem.* **1996**, *100*, 14037-14047.

33. De Gennes, P. G. "Wetting: Statics and Dynamics", *Rev. Mod. Phys.* 57, 1985, 827-863.

34. Ausserre, D.; Picard, A. M.; Leger, L. "Existence and Role of the Precursor Film in the Spreading of Polymer Liquids", *Phys. Rev. Lett.* **1986**, *57* 2671-2674.

35. Bao, Z.; Dodabalapur, A.; Lovinger, A. J. "Soluble and Processable Regioregular Poly(3-hexylthiophene) for Thin Film Field-Effect Transistor Applications with High Mobility", *Appl. Phys. Lett.* **1996**, *69*, 4108-4110.

36. Valaski, R.; Moreira, L. M.; Micaroni, L.; Hümmelgen, I. A. "Charge Injection and Transport in Electrochemical Films of Poly(3-hexylthiophene)", *J. Appl. Phys.* **2002**, *92*, 2035-2040.

37. Hamadani, B. H.; Natelson, D. "Temperature-Dependent Contact Resistances in High-Quality Polymer Field-Effect Transistors", *Appl. Phys. Lett.* **2004**, *84*, 443-445.

38. Sirringhaus, H.; Tessler, N.; Friend, R. H. "Integrated Optoelectronic Devices Based on Conjugated Polymers", *Science*, **1998**, *280*, 1741-1744.

39. Sirringhaus, H.; Brown, P. J.; Friend, R. H.; Nielsen, M. M.; Bechgaard, K.; Langeveld-Voss, B. M. W.; Spiering, A. J. H.; Janssen, R. A. J.; Meijer, E. W.; Herwig, P.; de Leeuw, D. M. "Two-Dimensional Charge Transport in Self-Organized, High-Mobility Conjugated Polymers", *Nature (London)* **1999**, *401*, 685-688.

40. Stutzmann, N.; Friend, R. H.; Sirringhaus, H. "Self-Aligned, Vertical-Channel, Polymer Field-Effect Transistors", *Science* **2003**, *299*, 1881-1884.

41. Bürgi, L.; Richards, T. J.; Friend, R. H.; Sirringhaus, H. "Close Look at Charge Carrier Injection in Polymer Field-Effect Transistors", *J. Appl. Phys.* **2003**, *94*, 6129-6137.

42. Rep, D. B. A.; Morpugo, A. F.; Klapwijk, T. M. "Doping-Dependent Charge Injection into Regioregular Poly(3-hexylthiophene)", *Org. Electron.* **2003**, *4*, 201-207.

43. Mas-Torrent, M.; den Boer, D.; Hadley, P.; Schenning, A. P. H. J. "Field Effect Transistors Based on Poly(3-hexylthiophene) at Different Length Scales", *Nanotechnology* **2004**, *15*, S265-S269.

44. Blom, P. W. M.; de Jong, M. J. M.; Vleggaar, J. J. M. "Electron and Hole Transport in Poly(p-phenylene vinylene) Devices", *Appl. Phys. Lett.* **1996**, *68*, 3308-3310.

Chapter 5

A Single Polymer Nanowire Photodetector

5.1 Introduction

Semiconducting nanowires and nanotubes are an emerging class of one-dimensional (1-D) nanostructures that represent attractive building blocks for nanoscale electronic and photonic devices. For example, inorganic semiconductor nanowires[1-3] and carbon nanotubes,[4] show great promise for nanoelectronic devices and integrated nanosystems because they can function both as device components for logic, memory and sensing applications and also as interconnects. Inorganic semiconducting nanowires are also attracting increasing research interest as building blocks for integrated nanophotonic systems since they can function as sub-wavelength optical waveguides, emissive devices and photodetectors.[1-3,5-13] With respect to the latter, photoconductance measurements have been recently been reported for a range of single inorganic nanowire devices: InP,[5] ZnO,[6] GaN,[7] and Si;[8] as well as for carbon nanotubes.[14]

While inorganic nanowires and carbon nanotubes have been explored in depth, the challenge of controlled fabrication of 1-D nanostructures based on organic molecular materials suitable for integrated nanophotonic applications has yet to be as comprehensively addressed. In particular, semiconducting polymers are attractive materials due to their chemically tunable opto-electronic properties, as well as their facility for solution processing.[15,16] 1-D nanostructures fabricated from such polymers have been the subject of recent research *viz.* their physical, chemical, electronic and photonic properties.[17-22] However, demonstration of viable polymer nanowire photonic technologies will require development of reliable methods for production of such structures with good control over critical parameters such as diameter, length, morphology and chemical composition. In the last chapter, a new method for formation of organic nanotubes and nanowires by wetting of porous anodised alumina membranes was introduced.[22] This method of template wetting using solution-based or molten material does not require specialised apparatus and has been shown to be broadly applicable across a wide range of organic materials, including small molecules, oligomers, polymers, blends and multi-component solutions.[22]

In this chapter*, the method of solution-assisted template wetting is successfully extended to high-yield controlled synthesis of poly[(9,9-dioctylfluorenyl-2,7-diyl)-co-(bithiophene)] (F8T2) nanowires. Following liberation from the template and dispersion, this method produced discrete nanowires with average lengths of 15 μm and mean diameters of 200 nm. The electrical characteristics of single nanowire devices and, also, the use of single F8T2 nanowires in photoconductivity-based photodetectors were then investigated. To date, there have been relatively few reports on photoconductivity in 1-D polymer nanostructures. Kim and co-

* This work will be published as "A Single Polymer Nanowire Photodetector", *Adv. Mater*. submitted.

workers have reported photo-conductance in single bilayer nanotubes comprising poly-(p-phenylenevinylene) (PPV) nanotube cores and carbonised PPV outer shells.[23] However, in this chapter, photoconductivity measurements of F8T2 nanowire devices are presented which yielded monochromatic single nanowire responsivities ~ 0.4 mA/W and external quantum efficiencies ~ 0.1 %, i.e., comparable with data reported for single inorganic nanowire devices. The results demonstrate the promise of these novel nanostructures as ultra-miniature photodetectors with potential for integration into future hybrid nanophotonic devices and systems.

5.2 Experimental

5.2.1 Synthesis of Nanowires

Reagents and solvents were purchased from Aldrich, and used without further purification. De-ionised water (Millipore; Q, > 18 MΩcm) was used for all aqueous solutions. Poly[(9,9-dioctylfluorenyl-2,7-diyl)-co-(bithiophene)] (F8T2) with mean molecular weight M_W = 19000 g/mol was purchased from ADS Inc., Canada, and stored under nitrogen before use. Porous anodised alumina membranes (Anodisc 13; 200 nm nominal pore diameter) were purchased from Whatman Ltd. Nanowires were fabricated under ambient conditions by the method of template synthesis: 50 μL of a 60 mg/mL solution of F8T2 in tetrahydrofuran (THF) was drop cast on a glass coverslip. Immediately after this, a membrane was placed on top of the drop, which was then covered by another glass coverslip. A 2.5kg weight was then applied for 12 hours in order to facilitate penetration of the F8T2 solution by capillary action. A razor blade was used to remove excess F8T2 from the alumina membrane followed by polishing with 1200 grid sand paper. In order to free nanowires from the membrane and disperse them in solution, the following protocol was followed: The polished membrane was soaked in 6 M aqueous NaOH for 12 hours, the NaOH supernatant was decanted off and replaced with 6 M NaOH. Excess organic residue was then removed by two cycles of sonication (B2510E, Branson Corp.; 45 kHz, 100 W, 60 seconds), centrifugation (8000 rpm, 30 seconds), removal of the supernatant and addition of fresh NaOH. A further two cycles were then performed with deionised H_2O as the solvent. Following the final centrifugation step, the H_2O supernatant was decanted off, replaced with acetonitrile and the solution was briefly agitated to disperse the nanowires.

5.2.2 Structural Characterisation of Polymer Nanowires

Transmission electron microscopy (TEM) measurements were acquired for individual nanowires deposited on carbon-coated copper TEM grids (JEM-2011, JEOL UK Ltd; Gatan DualVision 600 charged-coupled detector (CCD) Camera and Digital Micrograph Software, Gatan UK Ltd.). Selected area electron diffraction (SAED) patterns were recorded from selected areas of the sample with a camera length of 35 cm. The TEM was calibrated using standard samples both for magnification and diffraction.

Scanning electron microscopy (SEM) images of nanowire arrays and individual nanowires were acquired using a field emission SEM (JSM-6700F, JEOL UK Ltd.) operating at beam voltages between 1 and 10 kV. For imaging of nanowire arrays, filled porous alumina membranes were mounted on SEM stubs using carbon pads and then dipped in NaOH solution (6 M) to remove the template and leave freestanding forests of F8T2 wires.

X-ray diffraction (XRD) measurements were performed on arrays of F8T2 nanowires embedded in porous alumina templates fragments, prepared by solution wetting from a 60 mg/mL solution of F8T2 in THF (Philips X'pert Pro diffractometer, Panalytical UK Ltd.). For comparative purposes, XRD measurements were also acquired for a polymer thin film, prepared from the same 60 mg/mL solution of F8T2 in THF and drop cast onto silicon substrates, and for an as-received alumina membrane. The system was configured in a symmetric reflection coupled $\theta/2\theta$ mode using a Cu K_α radiation source ($\lambda_{K\alpha}$ = 1.549 Å) with the surface of the templates and film samples oriented perpendicular to the plane of the incident and scattered X-rays.

The topography of individual nanowires drop-deposited onto glass slides was characterised using a calibrated atomic force microscope (AFM) system (Topometrix Explorer, Veeco Instruments Ltd.) in tapping mode using commercial tapping mode AFM probes (Nanosensors, NCHR; typical radius of curvature ~ 10 nm and front/rear cone angles of 22.5 º / 27.5 º respectively).

5.2.3 Optical Characterisation of Polymer Nanowires

Epi-optical and epifluorescence microscopy images of individual nanowires and nanowire mats, drop deposited from acetonitrile suspension onto clean glass microscope slides, were acquired using a calibrated epifluorescence microscope (Zeiss Axioskop II Plus, Carl Zeiss U.K.) equipped with a CCD camera (Optronics DEI-750). For epifluorescence imaging, a 100 W arc lamp was employed, together with an appropriate filter set (Zeiss 18), enabling excitation between 390 and 420 nm and collection of all the resulting fluorescence above 450 nm. Images were analysed using Image Pro Express software (Media Cybernetis Inc., USA).

UV-Vis absorption spectra were acquired from solutions of F8T2 in THF (80 μg/mL), as well as from thin films prepared by spin casting solutions of F8T2 from THF (1 mg/mL) onto glass using a spectrophotometer (8453E, Agilent Technologies Inc.). UV-Vis absorption spectra were also acquired from mats of nanowires dispersed on glass microscope slides using a double beam spectrophotometer equipped with an integrating sphere system (2401, Shimadzu Europe Ltd.).

Photoluminescence spectra were acquired using an in-house built optical system for solutions of F8T2 in THF (20 μg/mL), thin films of F8T2 spun cast onto glass substrates from solutions of F8T2 in THF (1 mg/mL) and for mats of F8T2 nanowires deposited onto glass substrates. Samples were optically pumped at 350 nm with an argon ion laser (Innova

Enterprise II, Coherent Inc.) using reflective neutral density filters (Newport Corp.) to attenuate the intensity. Spectra were collected using a fibre-coupled monochromator (0.19 m; Jobin-Yvon Ltd. Triax 190), with an input slit width of 0.1 mm. An output slit width of 0.75 was used for nanowire mats, while an output slit width of 0.15 mm was used for the solution and thin film samples. A photomultiplier tube (R928, PMT Hamamatsu Photonics K.K.) was used to detect the visible emission. Analysis was carried out with Jobin-Yvon's SpectRad software. The incident light power was focussed onto the sample at an angle of 27 ° to the plane of the sample and emission was collected at an angle of 63 ° degrees to the plane of the sample. Input light powers of 0.2 mW, 1.3 mW and 1.5 mW were used for the solution, thin film and nanowire mat samples, respectively.

5.2.4 Fabrication of Bottom Contacted Nanowire Devices

For bottom contacted measurements of electrical transport through F8T2 nanowires, laterally patterned parallel gold electrodes, 50 μm in length and 1 μm wide, and with interelectrode gaps ranging from 1 μm to 5 μm were fabricated on oxidised Si wafer chips (*n* type, 2-4 Ωcm, 100 nm thermal oxide) using optical lithography followed by metal evaporation (Ti 3 nm/Au 20 nm) and lift off. Nanowire devices were prepared by drop depositing from acetonitrile suspension onto the electrode chips. Nanowire devices were examined using optical microscopy.

5.2.5 Bottom Contacted Nanowire Electrical Measurement

For room temperature electrical measurements, electrode chips were electrically contacted using a probe station (Wentworth Laboratories PML 8000 Analytical, Wentworth Laboratories, Inc.). Electrical measurements were performed using a HP4156A Semiconductor Parameter Analyser (Agilent Technologies Inc.), with a voltage resolution < 1 mV and a current resolution < 100 fA, which was programmed using Agilent VEE Pro 6.0 software. Voltages were swept up to ± 5 V in step sizes of 0.25 V. All measurements were made under ambient condition in the dark.

5.2.6 Fabrication of Top Contacted Nanowire Devices

For top contacted measurements of electrical transport through F8T2 nanowires, well-dispersed F8T2 nanowires suspended in acetonitrile were deposited onto pre-cleaned 1 cm^2 microscope slides under ambient conditions. The acetonitrile was allowed to evaporate off and the samples were then transferred to an inert atmosphere glovebox system (MBraun Ltd.) with sub-ppm levels of H_2O and O_2. The nanowire bearing glass chips were loaded into a vacuum oven, annealed at 40 ºC for 1 hour and then allowed to cool down to room temperature.

Transmission electron microscopy grids (600 mesh, Agar Scientific Ltd.) were employed as shadow masks, comprising arrays of square holes (nominally 37 μm × 37 μm) separated by metal wires (~ 7 μm wide). The grids were mounted directly on top of the nanowire chips, which were loaded into a metal evaporator system (BOC Edwards Ltd.) located inside the glovebox. Gold electrodes (300 nm thick) were thermally evaporated onto the nanowire chips to create arrays of square electrode pads with interelectrode gap ~ 6 μm. After allowing the system to cool down sufficiently, the samples were removed from the evaporator and stored until needed in the glovebox.

5.2.7 Top Contacted Nanowire (Opto-) Electrical Measurement

Following optical inspection of the devices under ambient conditions, photoconductivity measurements were performed using a modified near-field scanning optical microscope (Aurora II NSOM, Veeco Instruments Ltd.); see Figure 5.1.[24] The nanowire-bearing glass chips were illuminated from below using 405 nm laser excitation (Blue Photon, LG-Laser Technologies GmbH, Germany), which was coupled into the NSOM head via a high power density single mode optical fibre (F-MTC, Newport Ltd.) via a dichroic mirror (XF2034, Glen Spectra). At the termination of the optical fibre, the light was collimated using an aspherical lens (KPA010, 20×, NA = 0.88, Newport Ltd.). The beam then propagated through free space and was directed into the NSOM head via an optical train of mirrors and prisms. The laser power was measured at the output of the head stage using a handheld SiGe photodetector (840 C meter with 818-UV low power detector, Newport Ltd.). An objective lens (PL 40×, NA = 0.65, Olympus UK Ltd.) was used to focus the laser beam onto the glass chip from below (transmission mode).

In order to locate wires of interest, the NSOM control software (SPMLab, Veeco Instruments Ltd.) was used to translate the NSOM scanning stage (6 mm range, 0.1 μm step size) relative to the transmission mode microscope objective lens in order to locate the desired, contacted wire centrally over this lens. The NSOM CCD camera system (GW-304R B/W ½″ CCD, GenWac Inc.) was used in conjunction with the reflection mode objective lens located above the sample (SLMPL 20×, NA = 0.35, Olympus UK Ltd.) to monitor the position of the contacted wires. The pivoting mirror in the NSOM head was manually flipped so that the output of either the reflection or transmission mode lens was directed towards the CCD camera via a second flip-up mirror. Once a suitably contacted wire was located centrally above the transmission mode lens, the mirrors were manually flipped again so that the wire could be illuminated from beneath via the transmission mode lens.

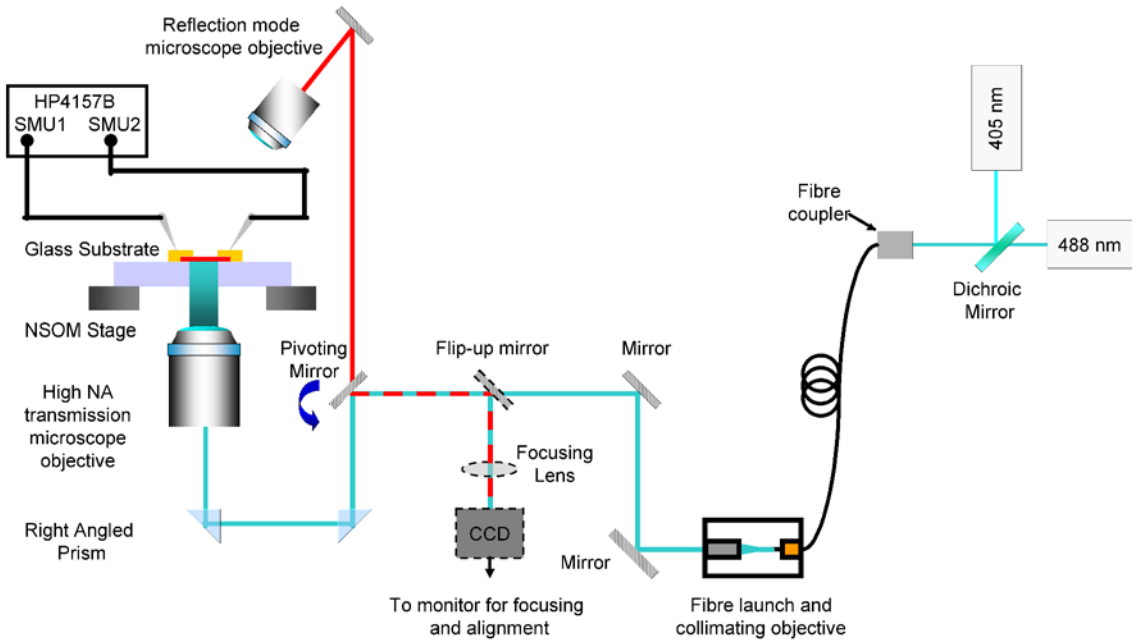

Figure 5.1. Schematic representation of the modified near field scanning optical microscope used to conduct photoconductivity measurements. The contacted nanowire is positioned over the transmission mode microscope objective and then contacted using two manual linear motion probes. The position of the probes is monitored via the reflection mode microscope objective in conjunction with a CCD camera system. Once the wire has been contacted it can be illuminated from beneath with a 405 nm laser.

Electrical contact was made to the evaporated Au electrodes using two manual linear motion probes (PVX 500, Wentworth Labs Ltd.). The position of the probes relative to the electrodes was monitored using the reflection mode lens as above. Electrical measurements were performed using a HP4157B Semiconductor Parameter Analyser (Agilent Technologies Inc.), with voltage resolution < 1 mV and current resolution < 20 fA, which was programmed using Agilent VEE Pro 6.0 software. Voltages were swept up to ± 40 V in various step sizes ranging from 0.25 V to 4 V. Current-voltage (*I-V*) characteristics of single top-contacted nanowires were acquired in the dark, under continuous 405 nm illumination and under manually chopped 405 nm illumination.

5.3 Results and Discussion

5.3.1 Physical Characterisation of Nanowires

Figure 5.2(a) shows a SEM image of the injected side of an array of F8T2 nanowires following partial dissolution of the alumina template using aqueous NaOH. The image demonstrates the efficiency of the solution wetting process for high-yield preparation of these 1-D nanostructures. Figure 5.2(b) shows a high magnification image of the opposite side of the array showing F8T2 nanowires with similar diameters and lengths. The nanowires were then freed from the template by completely dissolving the alumina in aqueous NaOH and were ultimately dispersed in acetonitrile through several cycles of washing by sonication and centrifugation in NaOH and deionised H_2O, respectively. Few single wires were observed for dispersion protocols where only a single sonication step was employed during washing, with the majority of the wires forming bundles. In fact, multiple sonication steps were required to

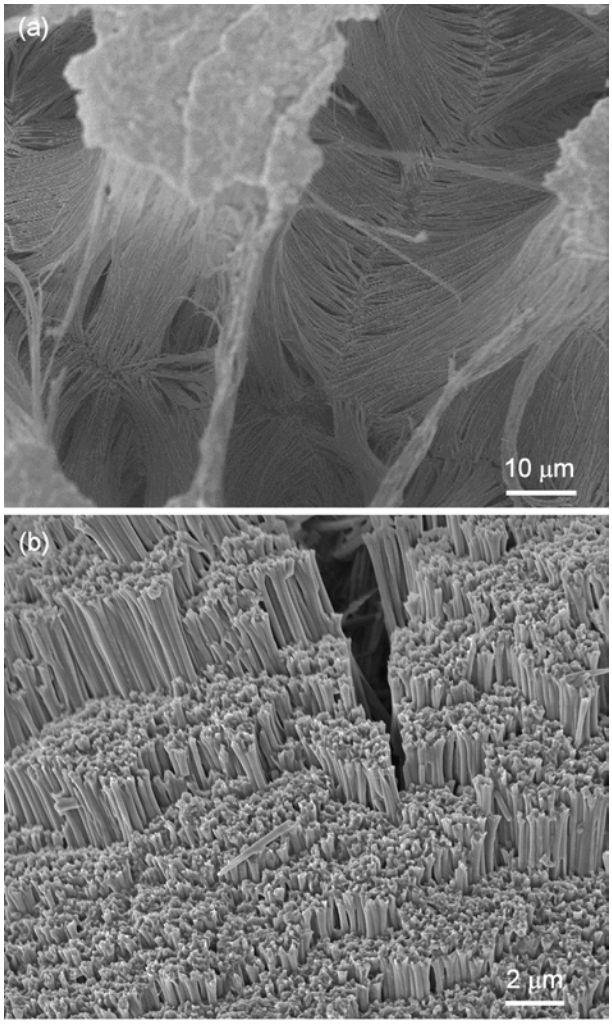

Figure 5.2. (a) Scanning electron microscope (SEM) image of an array of F8T2 nanowires following template removal (injected side of template). (b) High magnification image of the F8T2 nanowire array (opposite side of template).

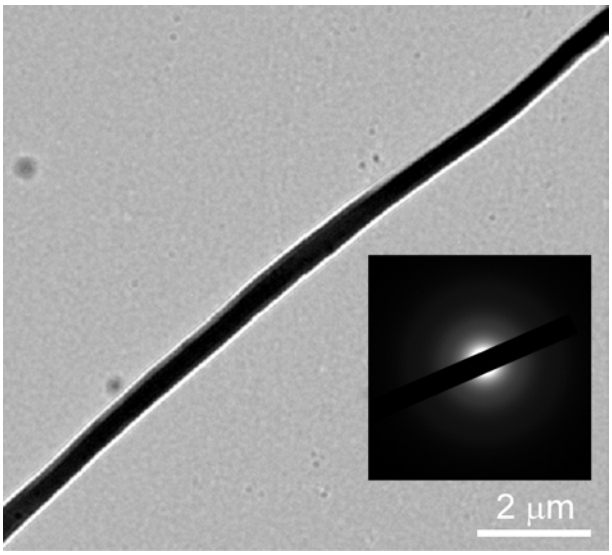

Figure 5.3. Transmission electron microscope (TEM) image of an isolated F8T2 nanowire. Inset: Selected area electron diffraction (SAED) pattern of a region of the wire shown in the main panel.

liberate and disperse the wires fully. It was found that the mean nanowire length decreased as a function of the number of sonication steps, resulting in a mean wire length ~ 15 μm, measured for dispersed single wires following a total of four sonications. Individual wires with lengths up to 50 μm were also observed at low number density (~ 2%).

Figure 5.3 shows a high resolution TEM image of a single nanowire. The morphology appears smooth, with a low density of defects and the uniform contrast indicates wire formation. The inset shows a selected-area electron diffraction image for the wire shown in the main panel. No diffraction spots or rings are evident, indicating that the polymer molecules within the wire do not adopt any appreciable long range order.

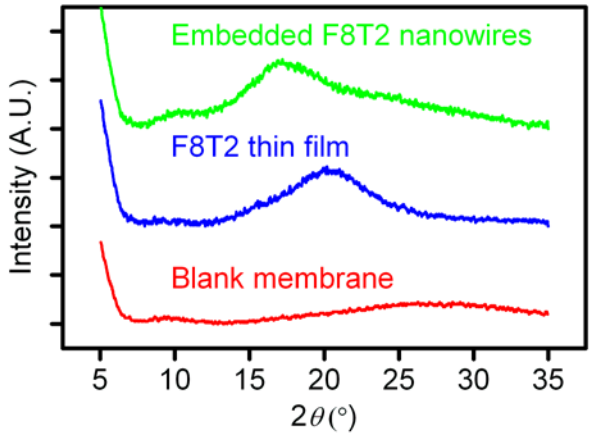

Figure 5.4. X-ray diffractograms of a blank alumina membrane (red curve), a drop cast thin film of F8T2 (blue curve) and F8T2 nanowires embedded in an alumina template (green curve).

X-ray diffraction data were acquired for arrays of F8T2 nanowires embedded in porous alumina membranes; see Figure 5.4. Diffractograms acquired for the injected and non-injected sides of the membrane were identical. For the nanowire sample, the first order reflection is not observable in the scan, due to the measurement range employed, but the lack of higher order reflections at low angles indicates that the wires possess no or only a small extent of long range order. A broad diffraction peak is observable in the wide angle regions of the polymer samples, e.g., at ~ 20 º in the thin film sample, corresponding to a *d* spacing ~ 4.4 Å. The width of this peak, which has been attributed to the lateral distance between polymer chains within layer planes or to side chain crystallization, likewise points to a low degree of crystallinity within the polymer thin film and nanowire samples.[25]

The topography of individual nanowires dispersed from solution was characterised using

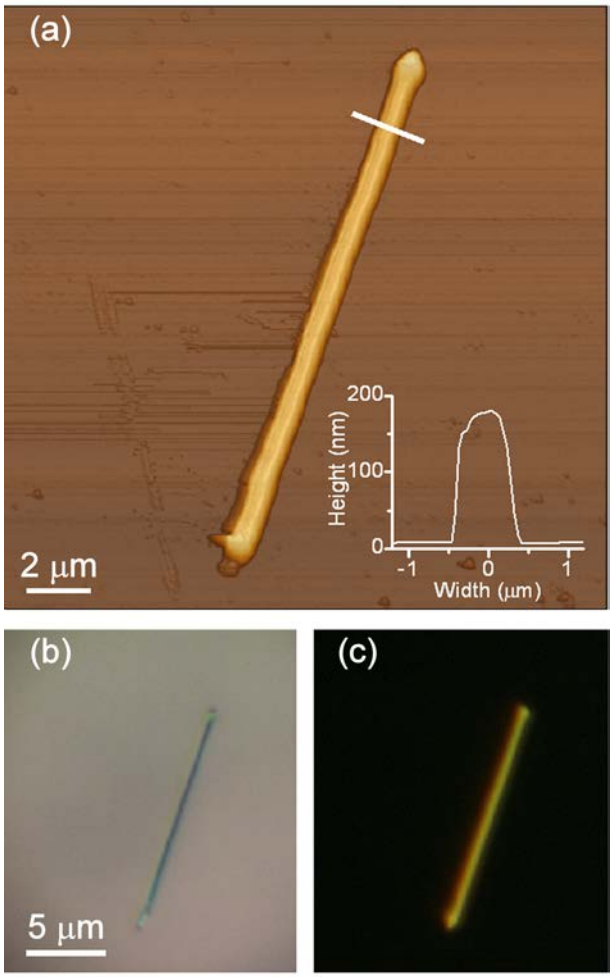

Figure 5.5. (a) Tapping mode atomic force microscopy (AFM) image of an F8T2 nanowire. Inset**:** Cross sectional line profile of the wire showing a maximum height of 190 nm, the effects of tip induced distortion can be seen in the diameter of the line profile. (b) Epi-optical and (c) epifluorescent images of the same wire.

AFM. Figure 5.5(a) shows tapping mode AFM image of a typical wire (length ~ 17 μm), again showing little curvature and a low density of defects. The inset to Figure 5.5(a) shows a line profile across the nanowire. Since the height is unaltered by tip-induced lateral broadening, measured heights were taken to represent the actual nanowire diameter. From multiple line profiles, the diameter was determined to be 190 ± 10 nm, in good agreement with the nominal pore diameter of the template. Figures 5.5(b) and (c) show epi-optical and epifluorescence images of this wire, respectively. Figures 5.5(c) demonstrates uniform emission along the length of the wire with the characteristic yellow colour of F8T2.

The intensity-normalised absorption and photoluminescence spectra of a solution of F8T2 in THF, a thin film of F8T2 on glass and a mat of F8T2 nanowires on glass are shown in Figure 5.6 (red, green and blue lines, respectively). For the thin film, the F8T2 absorption and emission bands are substantially red-shifted compared to those of the solution as a result of electronic perturbations due to π–stacking of polymer chains in the solid state. The 0–0 emission peak is also absent, due to self-absorption effects within the layer. The absorption and emission spectra of the F8T2 wires show good agreement with the thin film data, along with further broadening of the F8T2 absorption profile due to enhanced light scattering within the disordered array of nanowires comprising the mat.

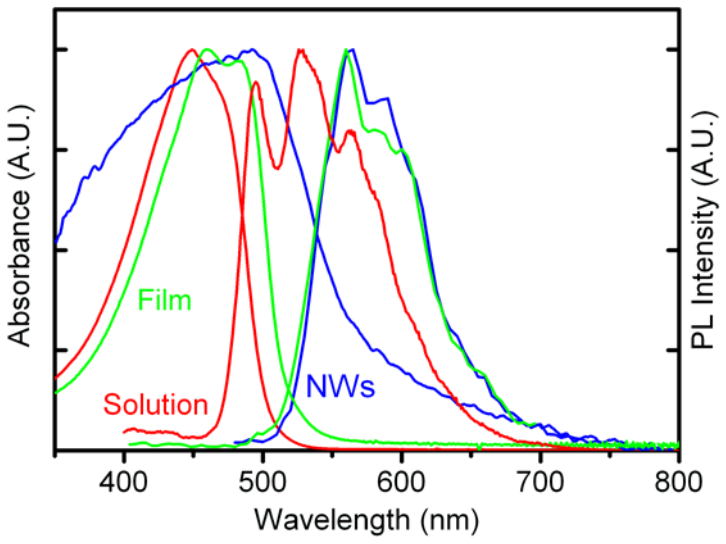

Figure 5.6. UV-Vis absorption and photoluminescence (PL) spectra of solutions of F8T2 in THF (red lines), 80 μg/mL and 20 μg/mL, respectively. The absorption and PL spectra of a thin film of F8T2 spun cast from a 1 mg/ml solution of F8T2 in THF (green lines) and of a mat of nanowires (blue lines) are also shown.

5.3.2 Electrical Characterisation of Bottom Contacted Nanowires

Figure 5.7(a) shows the electrical measurement configuration for a bottom contacted nanowire device following drop deposition of single nanowires onto prepatterned gold microelectrodes on oxidised silicon chip substrates. The inset to Figures 5.7(b) shows a typical bottom contacted device. For electrical characterisation, the source was grounded, a bias voltage sweep was applied to the drain and the current through the nanowire was measured in the dark under ambient conditions. The main panel of Figure 5.7(b) shows the measured current-voltage (*I*-*V*) characteristics for the device shown in the inset. The data are linear and quasi-symmetric for bias voltages in the range –2.5 V to 2.5 V. In this regime, the extracted device resistance, $R \sim 7 \times 10^{11}$ Ω. The measured wire length $L \approx 3$ μm and the diameter $D \approx$ 200 nm, thus the wire resistivity can be calculated, $\rho = \pi D^2 R/4L \approx 7 \times 10^3$ Ωm. For the 8 devices measured, the extracted resistivity values were in the range 7×10^3 Ωm $< \rho < 4 \times 10^4$ Ωm. For each device, this value represents an upper bound for the nanowire resistivity since the measured device resistance (*R*) is likely to include contributions from parasitic series resistances between the nanowire and the source and drain electrodes, respectively.

The extracted resistivity data indicate that the nanowires are likely to be (unintentionally) doped, possibly due to air exposure.[26] The measured non-linearity at higher bias in the single

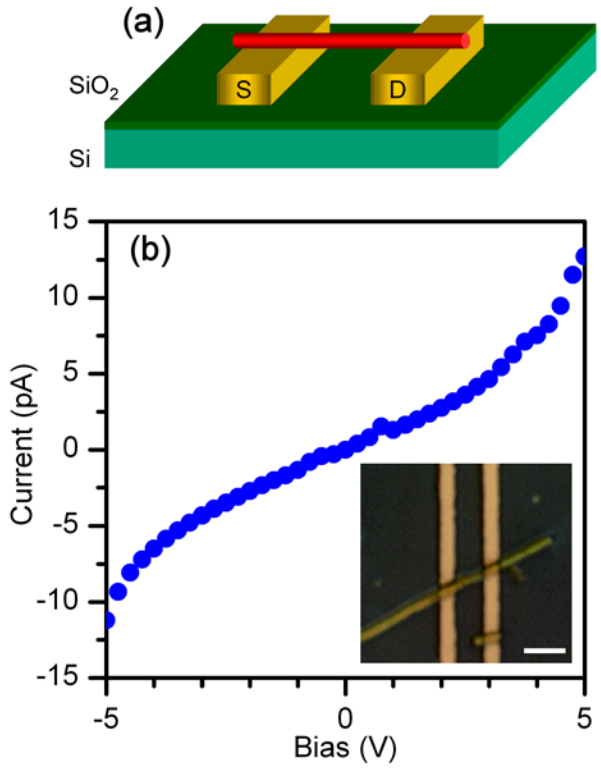

Figure 5.7. (a) Schematic of a bottom contact nanowire device. (b) *I*-*V* characteristics of a bottom contacted F8T2 nanowire acquired in the dark. Inset: Optical micrograph of this device. Scale bar: 2 μm.

nanowire *I-V* data shown in Figure 5.7(b) suggests injection-limited transport, which has previously been observed in short-channel F8T2 vertical transistor devices and attributed to non-ohmic voltage drops at the nanowire-electrode contacts.[26] The injection barriers may arise due to the difference between the ionization potential of F8T2 (~ 5.5 eV) and the work function of gold (~ 5.3 eV), although the small contact area may also be a significant factor.[26] Well known mechanisms for carrier injection into polymers include Fowler-Nordheim tunneling and thermionic emission.[27] Since the maximum electric fields employed ($F \sim V/L \leq 2 \times 10^6$ Vm^{-1}) are below the accepted threshold for Fowler-Nordheim tunneling in semiconducting polymers ($F_t \approx 10^7$ Vm^{-1}), this mechanism is not expected to be significant and thermionic emission should be the dominant carrier injection mechanism.

5.3.3 (Opto-) Electrical Characterisation of Top Contacted Nanowires

Top contacted F8T2 nanowire device with interelectrode gaps ~ 5 μm were fabricated on glass substrates using shadow masking and gold evaporation for single nanowire photoconductivity measurements using a modified NSOM; see Figure 5.8(a). The blue curve in Figure 5.8(b) shows the measured dark current (I_{dark}) for a typical device. The data shows quasi-linear characteristics at low bias, similar to measured data for bottom contacted nanowires, with some asymmetry at higher bias. The red curve in Figure 5.8(b) shows the measured current (I_{illum}) under continuous 405 nm illumination. A marked increase in the measured current is observed across the entire bias range. The green curve in Figure 5.8(b) shows the measured current under manually chopped 405 nm illumination, where the illumination was switched on or off at 10 V intervals during the bias sweep, corresponding to a duty cycle of 50%. These data demonstrate almost complete recovery of the device after illumination is removed, indicating that the photocurrent response is significantly larger than any thermionic or thermoelectric effects that might arise from a photo-induced temperature increase.[8,28,29]

The photocurrent can be defined as $I_{ph} = I_{illum} - I_{dark}$. From Figure 5.8(b), the maximum photocurrent measured is $I_{ph} \approx 200$ pA at $V = -40$ V. A useful figure of merit for photodetectors is responsivity (R_{res}), the ratio of the photocurrent to the incident light power. The responsivity can be calculated from $R_{res} = I_{ph} / I_{irr}A$, where A is the effective device area and I_{irr} is the irradiance of the incident light. The incident laser power (3 mW, measured without the objective lens in place) corresponds to an irradiance $I_{irr} \sim 40$ W/cm^2 for a beam diameter ~ 100 μm incident on the substrate. This value represents an upper bound for the irradiance since losses in the objective lens and the glass substrate are neglected. The effective

nanowire area

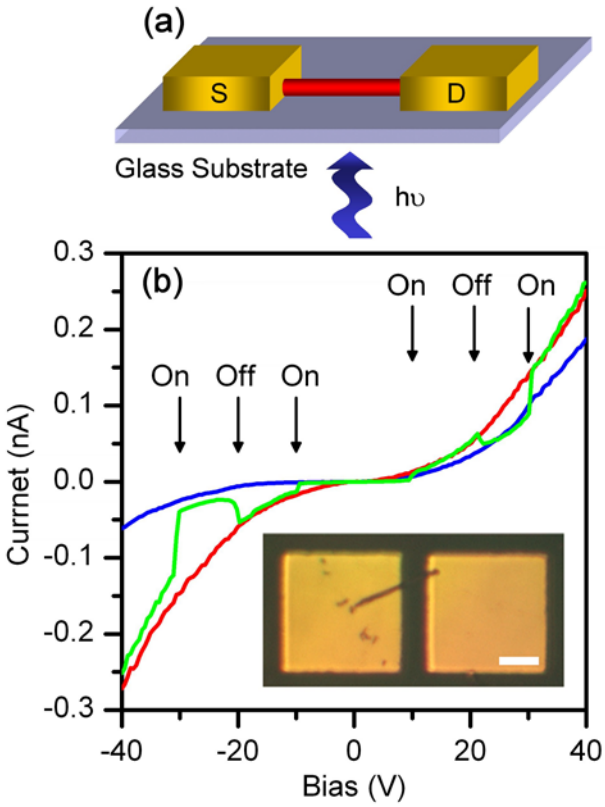

Figure 5.8. (a) Schematic of a top contact nanowire device. (b) *I-V* characteristics of a top contacted F8T2 nanowire acquired in the dark (blue line) and under 405 nm illumination (red line). Reversible switching (green line) measured under chopped illumination. Inset: Optical micrograph of a typical device; the scale bar is 10 μm.

(*A*) is taken as the wire diameter ($D \approx 200$ nm) multiplied by its length ($L \approx 6$ μm), thus $A = DL \approx 1.2 \times 10^{-8}$ cm^2. The measured single nanowire responsivity is then $R_{res} = 0.4$ mA/W. This value is comparable with measured responsivity values for back-gated large area F8T2 phototransistors, $R_{res} = 0.4$ mA/W for $V_{ds} = -10$ V and $V_{gs} = -40$ V at $I_{irr} \sim 3$ W/cm^2,[30] and is an order of magnitude larger than values measured for the devices at $V_{gs} = 0$ V.[30] The nanowire responsivity is also competitive with responsivity values extracted from published data for inorganic nanowires at irradiances similar to those used in this work: ~ 0.35 mA/W for a single InP nanowire device at low bias,[5] and ~ 0.5 mA/W for a single ZnO nanowire at 1 V bias.[6]

The quantum yield for the polymer nanowire device can also be estimated as follows: The incident radiant energy delivered to the nanowire per second is $I_{irr}A \approx 5 \times 10^{-7}$ J and the energy of a 405 nm photon is $E_p \approx 5 \times 10^{-19}$ J, thus yielding a flux ~ 10^{12} photons per second incident on the nanowire. The measured photocurrent ($I_{ph} \approx 200$ pA) corresponds to ~ 10^9 carriers per second, yielding an external quantum efficiency of ~ 0.1 %. Again, this is comparable to

published data for single inorganic nanowires, where the calculated external quantum efficiencies are ≈ 0.08 % and ≈ 0.17 % for single InP and ZnO nanowires, respectively.[5,6] The low value of the external quantum efficiency for these F8T2 nanowire devices may be due to a combination of several loss mechanisms: Inefficient dissociation of photogenerated excitons causing substantial recombination, low carrier mobility and limited carrier extraction due to contact barrier effects.[27,30,31]

5.4 Conclusion

In this chapter, solution-assisted template wetting has been successfully applied to high yield controlled synthesis of F8T2 conjugated polymer nanowires with good control over wire structure and morphology. The physical, electrical and opto-electronic characteristics of wires fabricated in this manner have also been presented. Structural characterisation indicated that the discrete F8T2 wires appear smooth with a low density of defects. The wires were found to have average lengths of ~ 15 μm and diameters ~ 200 nm. However wires with lengths up to 50 μm were also observed. As expected, structural data pointed to a low degree of crystallinity within the wires. Individual nanowires were electrically interfaced using top or bottom contact geometries. Current-voltage characteristics acquired for single nanowire devices indicated barrier formation at the nanowire-electrode interfaces and the range of the measured resistivity values, $7 \times 10^3\ \Omega m < \rho < 4 \times 10^4\ \Omega m$, suggested (unintentional) doping, possibly arising from air exposure.

The use of single F8T2 nanowires as ultra-miniature photodetectors was also described. Measurements of single nanowires yielded external quantum efficiencies ~ 0.1 % under monochromatic illumination, comparable with previously reported data for single inorganic nanowire devices. The single nanowire responsivity ~ 0.4 mA/W was found to be in good agreement with measured responsivity values for large area F8T2 phototransistors and is also competitive with responsivities extracted for inorganic nanowires under similar conditions. These results demonstrate the promise of these one-dimensional polymer nanostructures as sub-wavelength photodetectors with potential for integration into future nanophotonic devices.

5.5 References

1. Duan, X.; Huang, Y.; Cui, Y.; Lieber. C. M. In *Molecular Nanoelectronics*; Reed, M. A.; Lee, T.; American Scientific Publishers, California, **2003,** 199–227.

2. Huang, Y.; Lieber, C. M. "Integrated Nanoscale Electronics and Optoelectronics: Exploring Nanoscale Science and Technology Through Semiconductor Nanowires", *Pure Appl. Chem.* **2004**, *76*, 2051-2068.

3. Law, M.; Goldberger, J.; Yang, P. "Semiconductor Nanowires and Nanotubes", *Annu. Rev. Mater. Sci.* **2004**, *34*, 83-122.

4. Yao, Z.; Dekker, C.; Avouris, P. "Electrical Transport Through Single-Wall Carbon Nanotubes", *Top. Appl. Phys.* **2001**, *80*, 147-171.

5. Wang, J.; Gudiksen, M. S.; Duan, X.; Cui, Y.; Lieber, C. M. "Highly Polarized Photoluminescence and Photodetection from Single Indium Phosphide Nanowires", *Science* **2001**, *293*, 1455-1457.

6. Kind, H.; Yan, H. Q.; Messer, B.; Law, M.; Yang, P. D. "Nanowire Ultraviolet Photodetectors and Optical Switches", *Adv. Mater.* **2002,** *14*, 158-160.

7. Han, S.; Jin, W.; Zhang, D. H.; Tang, T.; Li, C.; Liu, X. L.; Liu, Z. Q.; Lei, B.; Zhou, C. W. "Photoconduction Studies on GaN Nanowire Transistors Under UV and Polarized UV Illumination", *Chem. Phys. Lett.* **2004**, *38*9, 176-180.

8. Ahn, Y.; Dunning, J.; Park, J. "Scanning Photocurrent Imaging and Electronic Band Studies in Silicon Nanowire Field Effect Transistors", *Nano Lett.* **2005**, *5*, 1367-1370.

9. Barrelet, C. J.; Greytak, A. B.; Lieber, C. M. "Nanowire Photonic Circuit Elements", *Nano Lett.* **2004**, *4*, 1981-1985.

10. Zhang, D.; Li, C.; Han, S.; Liu, X.; Tang, T.; Jin, W.; Zhou, C. "Ultraviolet Photodetection Properties of Indium Oxide Nanowires", *Appl. Phys. A* **2003**, *76*, 1-4.

11. Huang, Y.; Duan, X.; Lieber, C. M. "Nanowires for Integrated Multicolor Nanophotonics", *Small* **2005**, *1*, 142-147.

12. Greytak, A. B.; Barrelet, C. J.; Li, Y.; Lieber, C. M. "Semiconductor Nanowire Laser and Nanowire Waveguide Electro-Optic Modulators", *Appl. Phys. Lett.* **2005**, *87*, art. no.151103.

13. Qian, F.; Gradecak, S.; Li, Y.; Wen, C.-Y.; Lieber, C. M. "Core/Multishell Nanowire Heterostructures as Multicolor, High-Efficiency Light-Emitting Diodes", *Nano Lett.* **2005**, *5*, 2287-2291.

14. Freitag, M.; Martin, Y.; Misewich, J. A.; Martel, R.; Avouris, P. "Photoconductivity of Single Carbon Nanotubes", *Nano Lett.* **2003**, *3*, 1067-1071.

15. Forrest, S. R. "The Path to Ubiquitous and Low-Cost Organic Electronic Appliances on Plastic", *Nature* **2004**, *428*, 911-918.

16. Malliaras, G.; Friend, R. H. "An Organic Electronics Primer", *Phys. Today* **2005**, *58*, 53-58.

17. Merlo, J. A.; Frisbie, C. D. "Field Effect Conductance Of Conducting Polymer Nanofibers", *J. Polym. Sci. Pol. Phys.* **2003**, *41*, 2674-2680.

18. Merlo, J. A.; Frisbie, C. D. "Field Effect Transport and Trapping in Regioregular Polythiophene Nanofibers", *J. Phys. Chem. B* **2004**, *108*, 19169-19179.

19. Liu, H.; Reccius, C. H.; Craighead, H. G. "Single Electrospun Regioregular Poly(3-hexylthiophene) Nanofiber Field-Effect Transistor", *Appl. Phys. Lett.* **2005**, *87*, art. no. 253106.

20. Jeukens, C. R. L. P. N.; Jonkheijm, P.; Wijnen, F. J. P.; Gielen, J. C.; Christianen, P. C. M.; Schenning, A. P. H. J.; Meijer, E. W.; Maan, J. C. "Polarized Emission of Individual Self-Assembled Oligo(p-phenylenevinylene)-Based Nanofibers on a Solid Support", *J. Am. Chem. Soc.* **2005**, *127*, 8280-8281.

21. Kim, K.; Jin, J. I. "Preparation of PPV Nanotubes and Nanorods and Carbonized Products Derived Therefrom", *Nano Lett.* **2001**, *1*, 631-636.

22. Steinhart, M.; Wendorff, J. H.; Greiner, A.; Wehrspohn, R. B.; Nielsch, K.; Schilling, J.; Choi, J.; Gösele, U. "Polymer Nanotubes by Wetting of Ordered Porous Templates", *Science* **2002**, *296*, 1997.

23. Kim, K.; Kim, B. H.; Joo, S. H.; Park, J. S.; Joo, J.; Jin, J. I. "Photoconductivity of Single-Bilayer Nanotubes Consisting of Poly(p-phenylenevinylene) (PPV) And Carbonized-PPV Layers", *Adv. Mater.* **2005**, *17*, 464-468.

24. Ferri, V.; Scoponi, M.; Bignozzi, C. A.; Tyson, D. S.; Castellano, F. N.; Doyle, H.; Redmond, G. "Near-Field Optical Addressing of Luminescent Photoswitchable Supramolecular Systems Embedded in Inert Polymer Matrices", *Nano Lett.* **2004**, *4*, 835-839.

25. Kawana, S.; Durrell, M.; Lu, J.; Macdonald, J. E.; Grell, M.; Bradley, D. D. C.; Jukes, P. C.; Jones, R. A. L.; Bennett, S. L. "X-ray Diffraction Study of the Structure of Thin Polyfluorene Films", *Polymer* **2002**, *43*, 1907-1913.

26. Stutzmann, N.; Friend, R. H.; Sirringhaus, H. "Self-Aligned, Vertical-Channel, Polymer Field-Effect Transistors", *Science* **2003**, *299*, 1881-1884.

27. Blom, P. W. M.; de Jong, M. J. M.; Vleggaar, J. J. M. "Electron and Hole Transport in Poly(p-phenylene vinylene) Devices", *Appl. Phys. Lett.* **1996**, *68*, 3308-3310.

28. Lupton, J. M. "Frequency Up-Conversion as a Temperature Probe of Organic Opto-Electronic Devices", *Appl. Phys. Lett.* **2002**, *80*, 186-188.

29. Masubuchi, S; Kazama, S. "A Possible Phase Transition in Metallic Polythiophene and Poly(3-methylthiophene) at Low Temperature", *Synth. Met.* **1995**, *69*, 315-316.

30. Hamilton, M. C.; Martin, S.; Kanicki, J. "Thin-Film Organic Polymer Phototransistors", *IEEE Trans. Electron. Dev.* **2004**, *51*, 877-885.

31. Marks, R. N.; Halls, J. J. M.; Bradley, D. D. C.; Friend, R. H.; Holmes, A. B. "The PhotoVoltaic Response in Poly(p-phenylene vinylene) Thin-Film Devices", *J. Phys.-Condens. Matter* **1994**, *6*, 1379-1394.

Chapter 6

Thesis Summary

6.1 Conclusion

The objective of this thesis was the exploration and characterisation of the nanoscale electronic properties of conjugated polymers and nanocrystals.

In Chapter 2, the first application of CP-AFM based *z*-*V* spectroscopy to local measurement of the electronic properties of conjugated polymer thin films was reported. A key advantage of *z*-*V* spectroscopy over conventional current-voltage spectroscopy for measurement of threshold voltages is that the feedback loop remains active during the bias voltage sweep, thus a small increase in the measured current can result in a large relative displacement, allowing precise determination of the charge injection thresholds at both bias polarities. Using this approach, the charge injection thresholds along with corresponding single particle gap energies (E_{gsp}) and exciton binding energies (E_b) were determined for a MEH-PPV thin film. By performing measurements across a grid of locations on the film, a series of exciton binding energy distributions were identified, with peak E_b values ≈ 0.2 eV, 0.4 eV and 0.8 eV, respectively. The variation in measured E_b values was in contrast to the smoothness of the film surface suggesting that the variation may be attributable to differences in the nano-environment of the polymer molecules within the thin film at each measurement location. The method therefore represents a useful tool for local determination of electronic properties of organic materials.

In Chapter 3, it was shown that CP-AFM-based *z*-*V* spectroscopy also permits local, room temperature measurements of the Coulomb blockade voltage thresholds arising from sequential single electron charging of 28 kDa Au nanocrystals in current-carrying paths containing as few as 3 nanocrystals through portions of a nanocrystal array located between the apex of a conducting AFM probe and an underlying Au substrate. It was demonstrated that the fluid-like properties of the nanocrystal arrays enable reproducible formation of nanoscale probe-array-substrate junctions, allowing the influence of background charge on the electronic properties of the array to be identified. Finally, it was shown that the use of CP-AFM allows complementary topography and phase data to be acquired before and after spectroscopy measurements, enabling comparison of local array morphology with local measurements of the Coulomb blockade thresholds. It is suggested that CP-AFM based *z*-*V* spectroscopy could be an extremely valuable technique for characterization and analysis of charge transport through nanocrystal arrays, where specific information regarding the spatial variation of transport thresholds or, e.g., concerning the conductance of ligand molecules, is critically required.

In Chapter 4, it was shown that melt-assisted template wetting is a useful technique for the massively parallel fabrication of conjugated polymer nanowires. The physical and electrical

characteristics of P3HT wires fabricated in this manner were presented. Structural characterisation indicates that the P3HT wires were smooth with a low density of defects. The wires were found to have average lengths of ~ 10 μm and diameters ~ 450 nm while wires with length up to 30 μm are also observed. Extensive radial curvature is observed for the majority of dispersed single wires, indicating appreciable flexibility of these nanostructures. The nanowires are also granular, which suggests partial local dewetting of the molten polymer material from the pore walls during wire formation. Use of CP-AFM for local structural and electronic characterisation of individual nanowires was undertaken. CP-AFM is an excellent tool in this regard, as it allows non-invasive characterisation of nanostructures. Two-terminal electrical measurements of individual nanowires, utilising a CP-AFM tip as the source electrode, directly yielded values for the intrinsic nanowire resistivity and for the total nanowire-electrode contact resistance. Fits to a thermionic emission-diffusion model also allowed the single nanowire hole mobility and the mean nanowire-electrode barrier height to be evaluated. It is proposed that the template wetting method for synthesis of conjugated polymer nanowires may be an important future tool for fabrication of polymer based electronic nanostructures.

In Chapter 5, solution-assisted template wetting was successfully applied to high yield controlled synthesis of F8T2 conjugated polymer nanowires with good control over wire structure and morphology. The physical, electrical and opto-electronic characteristics of wires fabricated in this manner were also presented. Structural characterisation indicates that the discrete F8T2 wires were smooth with a low density of defects. The wires were found to have average lengths of ~ 15 μm and diameters ~ 200 nm. However wires with lengths up to 50 μm were also observed. As expected, structural data point to a low degree of crystallinity within the wires. Individual nanowires were electrically interfaced using top or bottom contact geometries. Current-voltage characteristics acquired for single nanowire devices indicated barrier formation at the nanowire-electrode interfaces and the range of the measured resistivity values, $7 \times 10^3\ \Omega m < \rho < 4 \times 10^4\ \Omega m$, suggested (unintentional) doping, possibly arising from air exposure. The first report of single F8T2 nanowires as ultra-miniature photodetectors was also presented. Measurements of single nanowires yielded external quantum efficiencies ~ 0.1 % under monochromatic illumination, comparable with previously reported data for single inorganic nanowire devices. The single nanowire responsivity ~ 0.4 mA/W was found to be in good agreement with measured responsivity values for large area F8T2 phototransistors and was also competitive with responsivities extracted for inorganic nanowires under similar conditions. These results demonstrate the promise of these one-dimensional polymer nanostructures as sub-wavelength photodetectors with potential for integration into future nanophotonic devices.

Appendices

A.1 Abbreviations

AC	alternating current
AFM	atomic force microscope/microscopy
AlQ_3	tris 8-(hydroxyquinoline) aluminium
CCD	charged-coupled detector
CMOS	complementary metal oxide semiconductor
CP-AFM	conducting-probe atomic force microscope
CV	cyclic voltammetry`
CVL	common vacuum level
DC	direct current
DNA	deoxyribonucleic acid
DPV	differential pulsed voltammetry
EFM	electrostatic field microscopy
F8T2	poly[(9,9-dioctylfluorenyl-2,7-diyl)-co-(bithiophene)]
HOMO	highest occupied molecular orbital
IPA	isopropanol
ISC	intersystem crossing
ITO	indium-tin oxide
KPM	Kelvin probe microscopy
LCD	liquid crystal display
LED	light emitting diode
LUMO	lowest unoccupied molecular orbital
MALDI-TOF/MS	matrix assisted laser desorption/ionization time of flight mass spectrometry
MEH-PPV	poly[2-methoxy-5-(2-ethylhexyloxy)-1,4-phenylenevinylene]
MO	molecular orbital
MOS	metal-oxide-semiconductor
MOSFET	metal oxide semiconductor field effect transistor
MUA	11-mercaptoundecanoic acid
NA	numerical aperture
NC	nanocrystal
NIR	near infrared
NMR	nuclear magnetic resonance
NSOM	near field scanning optical microscope
OLED	organic light emitting diode
P3HT	poly-(3-hexylthiophene)

PC	photoconductivity
PEDOT	3,4-polyethylene-dioxythiophene-polystyrenesulfonate
PL	photoluminescence
PLEDS	polymer light emitting diodes
PMMA	polymethyl methacrylate
PPV	poly-(p-phenylene vinylene)
PS	polystyrene
PTFE	polytetrafluoroethylene
PV	photovoltaic
RC	resistor-capacitor
RMS	root-mean-square
RPM	revolutions per minute
RR-P3HT	regioregular poly-(3-hexylthiophene)
SAED	selected area electron diffraction
SCE	saturated-calomel electrode
SCLC	space charge limited current
SCM	scanning capacitance microscopy
SEM	scanning electron microscope/microscopy
SPM	scanning probe microscope/microscopy
STM	scanning tunneling microscope/microscopy
STS	scanning tunneling spectroscopy
TCE	trichloroethane
TEM	transmission electron microscope/microscopy
TFT	thin film transistor
THF	tetrahydrofuran
TOAB	tetraoctylammoniumbromide
TOF	time of flight
UV	ultra violet
UV-Vis	ultra violet-visible
XRD	X-ray diffraction
z-*V*	displacement-voltage
0-D	zero-dimensional
1-D	one-dimensional
^{1}H NMR	proton nuclear magnetic resonance
2-D	two-dimensional
3-D	three-dimensional

A.2 Publications

O'Brien, G. A.; Quinn, A. J.; Redmond, G. "Local Mapping of Electronic Properties in MEH-PPV Thin Films Using Conducting-Probe Atomic Force Microscopy" *Nanotechnology* **2006**, submitted.

O'Brien, G. A.; Quinn, A. J.; Biancardo, M.; Preece, J. A.; Bignozzi, C. A.; Redmond, G. "Making Electrical Nanocontacts to Nanocrystal Assemblies: Mapping of Room-Temperature Coulomb-Blockade Thresholds in Arrays of 28-kDa Gold Nanocrystals", *Small* **2006**, *2*, 261-266.

O'Brien, G. A.; Quinn, A. J.; Iacopino, D.; Pauget, N.; Redmond, G. "Polythiophene Nanowires: Synthesis by Template Wetting and Local Electrical Characterisation of Single Wires", *J. Mater. Chem.* **2006**, accepted.

O'Brien, G. A.; Quinn, A. J.; Redmond, G. "A Single Polymer Nanowire Photodetector", *Adv. Mater*. **2006**, submitted.

A.3 Conference Presentations

Oral

O'Brien, G. A.; Quinn, A. J.; Redmond, G. "Local Electronic Characterisation of Conjugated Polymer Films using Conducting-Probe Atomic Force Microscopy", *1st International Nanofabrication Symposium*, Dundalk, Ireland, 10-12 March 2004.

Quinn, A. J.; O'Brien, G. A.; Redmond, G. "Local Electronic Characterisation of Conjugated Polymer Films using Conducting-probe Atomic Force Microscopy", *Trinity College Dublin & Veeco Instruments Scanning Probe Microscopy Conference*, Dublin, Ireland, 23 September 2003.

Poster

O'Brien, G. A.; Quinn, A. J.; Redmond, G. "Local Electronic Characterisation of Conjugated Polymer Films using Conducting-Probe Atomic Force Microscopy", *1st Annual Nanotechnology Symposium*, University College Cork, Cork, Ireland, 5 September 2003.

O'Brien, G. A.; Quinn, A. J.; Redmond, G. "Local Electronic Characterisation of Conjugated Polymer Films using Conducting-Probe Atomic Force Microscopy", *Trends in Nanotechnology 2003*, Salamanca, Spain, 15-19 September 2003.